Thèse
de doctorat
de l'UTT

Pengfei GAO

Fatigue Properties Under Complex Loadings of an AA7075 Alloy Processed by SMAT

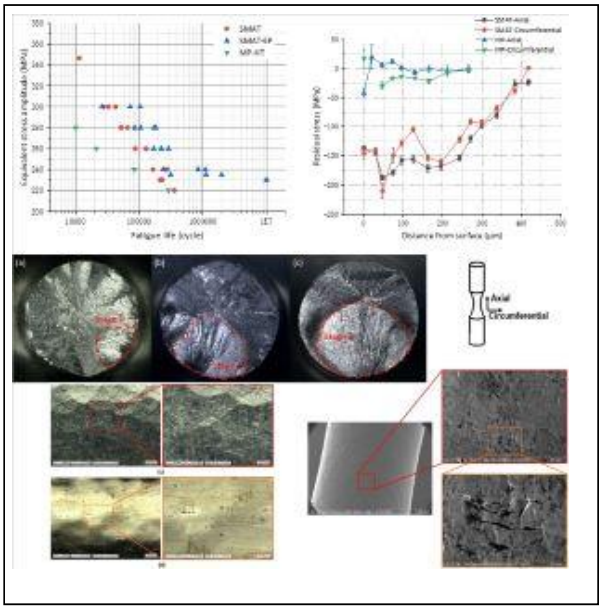

Champ disciplinaire :
Sciences pour l'Ingénieur

2024TROY0032 **Année 2024**

utt
UNIVERSITÉ DE TECHNOLOGIE
TROYES

THESE

pour l'obtention du grade de

DOCTEUR
de l'UNIVERSITE DE TECHNOLOGIE DE TROYES

en SCIENCES POUR L'INGENIEUR

Spécialité : MATERIAUX, MECANIQUE, OPTIQUE ET NANOTECHNOLOGIE

présentée et soutenue par

Pengfei GAO

le 2 octobre 2024

Fatigue Properties Under Complex Loadings of an AA7075 Alloy Processed by SMAT

JURY

Mme Véronique FAVIER	PROFESSEURE DES UNIVERSITES	Présidente
M. Lahouari BENABOU	PROFESSEUR DES UNIVERSITES	Rapporteur
Mme Catherine MABRU	PROFESSEURE DES UNIVERSITES	Rapporteure
M. Hongqian XUE	PROFESSOR	Examinateur
Mme Delphine RETRAINT	PROFESSEURE DES UNIVERSITES	Directrice de thèse
M. Zhidan SUN	PROFESSEUR ASSISTANT UTT	Directeur de thèse

To my family, my teachers and my friends

ACKNOWLEDGEMENTS

First and foremost, I would like to express my deepest gratitude to my supervisors, Prof. Delphine RETRAINT and Dr. Zhidan SUN, who have provided me with superior academic guidance and considerable support throughout my PhD study. Without them, I could not have been able to complete my PhD project. Their attitude and inspiration of research help me to have a deeper understanding of scientific research.

I would like to extend my sincere thanks to Dr. Bruno GUELORGET, who kindly taught me the operation of many instruments and helped me to conduct various experiments. I would also like to thank François WEIL, who supported my experimental work at J2 Building with patience. I would also like to thank everyone at LASMIS for helping me during my PhD study. The days I spent at LASMIS were very happy and fulfilling, and I will always miss them.

I also appreciate my friends, Yuan MENG, Xiao LIU, Hui CHEN, Lucas BRASILEIRO, Borui LI, Ke CAO, Hongshi CHEN, Kuan-ting WU, Zhihao GAO, Wei TAO, Zhengyang LYU, Yizhan FENG, Baoxing WANG, Yusen LI, Shengqiang SHI, for their companionship and support. Especially during the Covid-19 pandemic, without the help of my friends, I can hardly imagine how difficult the days would have been.

My sincere thanks should also go to my thesis committee members for their patience to examine my thesis and give insightful comments.

Last but not least, I would like to thank my family, especially my parents, who supported me all the way to finish my PhD study. Their support and encouragement have always been the strongest power within me.

Pengfei GAO

June 27, 2024, at Troyes

Abstract

Surface Mechanical Attrition Treatment (SMAT) is able of improving mechanical properties of metallic materials. The effect of SMAT on the biaxial fatigue properties of a 7075 aluminum alloy was investigated in the present work. The AA7075 dumbbell specimens were treated by SMAT, after a non-standard heat treatment and mechanical polishing. The SMAT-induced residual stress and its profile were evaluated by X-ray diffraction. Biaxial fatigue tests were performed under proportional combined tension-torsion loadings. A minimal difference in fatigue strength was found between mechanically-polished specimens and SMATed specimens at high and medium load levels, while a reduction was found after SMAT at low load levels. The effects of factors induced by SMAT were individually investigated by specially-designed post-SMAT processes, such as annealing and electropolishing. The compressive residual stress layer and the deterioration of surface integrity were considered as the main beneficial and detrimental factors influencing the fatigue strength. Specimens treated by SMAT and electropolishing exhibited significantly higher fatigue strength at all load levels. Multiaxial fatigue criteria were applied to estimate the fatigue strength of both mechanically-polished and SMATed specimens.

Key words: Aluminum alloys, Shot peening, Residual stresses, Materials--Fatigue, Materials—Cracking

Résumé

Le traitement par attrition mécanique de surface (SMAT) est capable d'améliorer les propriétés mécaniques des matériaux métalliques. L'effet du SMAT sur les propriétés de fatigue biaxiale d'un alliage d'aluminium 7075 a été étudié dans ce travail. Des éprouvettes sous forme d'haltères en alliage AA7075 ont été traitées par SMAT, après usinage, traitement thermique non standard et polissage mécanique. Les profils de contrainte résiduelle induits par SMAT ont été déterminés par diffraction des rayons X. Des essais de fatigue biaxiale ont été menés sous des chargements de traction-torsion proportionnels combinés. Une différence minimale de résistance à la fatigue a été constatée entre les échantillons polis mécaniquement et les échantillons traités par SMAT à des niveaux de chargement élevés et intermédiaires, tandis qu'une réduction a été constatée après SMAT pour de faibles niveaux de chargement. Les effets des facteurs induits par le SMAT ont été étudiés individuellement par un processus post-SMAT spécialement conçu, tel qu'un recuit et un électropolissage. La couche de contraintes résiduelles de compression et la détérioration de l'intégrité de la surface ont été considérées comme les principaux facteurs bénéfiques et néfastes influençant la résistance à la fatigue. Les échantillons traités par SMAT puis électropolis ont présenté une résistance à la fatigue significativement plus élevée pour tous les niveaux de chargement. Des critères de fatigue multiaxiale ont été appliqués pour estimer la résistance à la fatigue des échantillons polis mécaniquement et traités par SMAT.

Mots clés : Aluminium -- Alliages, Grenaillage de précontrainte, Contraintes résiduelles, Matériaux -- Fatigue, Matériaux – Fissuration

CONTENTS

General Introduction.....1
Chapter 1 Literature review.....4
1.1 Basic elements of SMAT.....4
1.1.1 Concepts of SMAT 5
1.1.2 Modifications induced by SMAT.....6
1.2 Effect of SMAT on fatigue properties.....15
1.2.1 Low-Cycle Fatigue after SMAT.....16
1.2.2 High cycle and very high cycle fatigue after SMAT.....18
1.2.3 Factors contributing to the effect of SMAT on fatigue properties..21
1.2.4 Effect of SMAT coupled with other treatment.....26
1.3 Aluminum alloy 7075.....31
1.3.1 Microstructure of AA7075.....31
1.3.2 Heat treatment of AA7075.....33
1.3.3 Fatigue fracture mechanism of AA7075.....34
1.4 Multiaxial fatigue.....38
1.4.1 Non-proportional hardening.....39
1.4.2 Damage mechanism.....40
1.4.3 Damage criterion and life estimation.....40
1.5 Scope of the thesis.....42
Chapter 2 Pre-test treatment and characterization.....44
2.1 Basic information on AA7075 material and specimen.....44
2.2 Heat treatment and mechanical polishing.....45
2.3 SMAT procedure.....47

2.4 Post-SMAT characterization 48
2.4.1 Surface quality 48
2.4.2 Residual stresses 51
2.4.3 Hardness and tensile strength 56
2.4 Conclusion 58
Chapter 3 Fatigue properties of SMATed AA7075 under biaxial loadings 59
3.1 Fatigue test procedure 59
3.1.1 Fatigue test device 59
3.1.2 Biaxial cyclic loadings 60
3.2 S-N data of biaxial fatigue tests 60
3.2.1 Mechanically-polished state 60
3.3.2 SMATed state 62
3.3 Statistical analysis of S-N data 63
3.3.1 Basquin equation 63
3.3.2 P-S-N analysis 65
3.4 Fractography observation 67
3.4.1 MP state 67
3.5 Conclusion 80
Chapter 4 Analysis of fatigue properties affected by SMAT 81
4.1 Effect of surface integrity on fatigue properties after SMAT 81
4.1.1 Post-SMAT electropolishing process 81
4.1.2 Fatigue strength of SMAT-EP specimens 86
4.2 Effect of SMAT-induced residual stresses on fatigue properties 91
4.2.1 Evolution of residual stress and FWHM during cyclic loadings 91
4.2.2 Post-SMAT heat treatment and its effect 94
4.3 Effect of grain refinement on fatigue properties 98
4.4 Effect of MP-induced residual stresses and work hardening 99
4.5 Conclusion 103

Chapter 5 Prediction on fatigue strength after SMAT with multiaxial fatigue criteria 105
5.1 Multiaxial fatigue criteria 105
5.1.1 Crossland criterion 105
5.1.2 Dang Van's criterion 106
5.1.3 Findley criterion 106
5.1.4 Fatemi-Socie criterion 106
5.2 Determination of material parameters 106
5.2.1 Crossland criterion 108
5.2.2 Findley and Fatemi-Socie criteria 109
5.3 Results and comparison 112
5.3.1 Prediction with Crossland criterion 113
5.3.2 Prediction with Findley and Fatemi-Socie criteria 116
5.4 Discussion and improvement on predictions 119
5.4.1 Effect of surface roughness 119
5.4.2 Effect of in-depth distribution of residual stresses 121
5.4 Conclusion 121
Chapter 6 Conclusions and prospects 123
6.1 Conclusions 123
6.2 Prospects 125
Résumé en français 126
References 136

List of tables

Table 1-1. Grain size in nanocrystalline layer of several SMATed materials. 8

Table 1-2. Surface hardness and roughness values of several materials treated by SMAT and other processes. 9

Table 2-1. Chemical composition of as-received AA7075 alloy (in wt.%) 44

Table 2-2. Parameters of SMAT 48

Table 2-3. Roughness of surfaces in different states (μm) 51

Table 3-1. Basquin equation parameters of MP and SMAT states. 64

Table 3-2. Weibull distribution fitting parameters for several MP state specimens 66

Table 5-1. Material parameter of 3 fatigue criteria at different fatigue lives 112

List of figures

Figure 1-1. (a) Schematic description of SMAT set-up, and (b) a single impact between a ball and the material surface, which generates a local plastically deformed region [13]. 6

Figure 1-2. Schematic description of the grain refinement process during SMAT [35]. 7

Figure 1-3. Tensile true stress-strain curve for the SMAT processed specimen, compared with the curve obtained for the specimen in as-received state, in 316L stainless steel [56]. 11

Figure 1-4. Tensile engineering stress-strain curves obtained for pure Al treated by SMAT with different intensities represented by different time durations [22]. 12

Figure 1-5. Engineering stress-strain curves obtained by monotonic compression tests for micro-pillars milled in a SMATed cross-section sample at different distances from the treated surface[59]. 13

Figure 1-6. HRTEM (High Resolution TEM) images of the squares marked in the inserted TEM bright-field images taken from (a) the solution-treated and (b) the as-SMATed samples; (c) EDX spectra detected at the points marked I (grain interior) and II (grain boundary) in (a) as well as III (grain boundary) in (b)[67]. 14

Figure 1-7. Relation between total strain amplitude and fatigue life for untreated and USSPed 7075 aluminum alloy (AA7075) samples (the figures denote the duration of treatment in seconds) [28]. 17

Figure 1-8. S–N curves for the untreated and UNSM-treated annealed Inconel 718 alloy obtained from rotating–bending fatigue (RBF) tests (UNSM with a load

of 15 N and an amplitude of 60 μm) [94]. 20
Figure 1-9. S–N plot for the fatigue data points obtained with electropolished (EP) AA7075-T6 samples and samples SMATed under different process conditions, namely, Steel-2 (SMAT using 2 mm steel shot), Steel-3 (SMAT with 3 mm steel shot) and Steel-3 + mechanical polishing (MP) [53]. 21
Figure 1-10. (a) fatigue striations space versus crack length curves for Zr-4 with different conditions: CG: coarse grain; SMGTed: after SMGT; A-SMGTed: SMGT and annealed; (b) S–N curves of different Zr-4 SMATed SMGTed samples and SMATed SMGTed samples combined with annealing at 400 °C[49].....23
Figure 1-11. (a) Evolution of residual stress at the top surface as a function of the number of cycles, with different load levels; (b) residual stress profiles with different load levels at N = Nf/2, for a micro alloyed steel [107]; (c) residual stress profiles of SMATed samples before and after fatigue; (d) residual stress profiles of CSPed samples before and after fatigue, for 316L stainless steel[108]. 24
Figure 1-12. SEM observation of microcracks induced by SMAT on an AA7075-T6 alloy with (a) 2 mm steel shots; (b) 3 mm steel shots[53].....26
Figure 1-13. (a) Residual stress profiles obtained for different conditions on 316L steel samples; (b) variation of grain size and hardness with annealing temperatures for the top surface layer; (c) S–N curves of different SMATed samples and SMATed samples combined with annealing[6].....27
Figure 1-14. S–N curves obtained at 10 Hz fatigue tests for a 304L austenitic stainless steel (RB: rotating bending; TC: tension–compression; G: ground state; P: polished state; RT: room temperature; CT: cryogenic temperature) [83].....29
Figure 1-15. (a) S–N plot of samples in different conditions (N8: nitrided for 8 h; N48: nitrided for 48 h; U1: UNSM with a strike number of 34,000 mm−2; U2:

UNSM with a strike number of 69,000 mm−2); (b) depth of inclusions inducing fish-eye initiations [103].....31
Figure 1-16. (a) Microstructure of 7xxx alloys; (b) optical micrograph; (c) TEM micrograph[28]. 33
Figure 1-17. Schematic of T6 heat treatment of 7xxx aluminum alloys[124].....34
Figure 1-18. S-N curves and cracking behaviors of AA7075-T651[126].....35
Figure 1-19. S-N plot of AA7075-T6 under uniaxial, torsional and combined loadings[127]. 36
Figure 1-20. Fracture mechanism map of AA7075-T6 in different biaxial loading conditions[127]. 37
Figure 1-21. A schematic of the crack trajectory of AA7075 tested under in-phase bending and torsional loading[128]. 38
Figure 1-22. Comparison of in-phase (IP) and 90° out-of-phase (OP) equivalent stress–strain data for Ti–6.5Al–3.4Mo (Ti)[134] and 304L stainless steel (SS)[100]. 39
Figure 1-23. Preferred cracking orientations observed for 1050 normalized steel under in-phase axial–torsion loading[139]. 40
Figure 1-24. Variation of von Mises and FS damage parameters with plane orientation forτa=0.7% of Ti–6.5Al–3.4Mo for in-phase (IP) and 90° out-of-phase (OP) axial–torsion loadings[129]. 42
Figure 2-1. (a) dimension of the AA7075 fatigue test specimens; (b) two typically investigated directions. 44
Figure 2-2. Schematic of heat treatment performed on AA7075 alloy. 45
Figure 2-3. Results of monotonic tensile tests with different heat treatments [147]. 46
Figure 2-4. The surface of the specimen in the: (a) as-received state; (b) mechanically polished state. 47
Figure 2-5. (a) The SMAT device in LASMIS UTT; (b) A specimen fixed in the SMAT

chamber with spherical shot (located at the place marked in red in (a)).....48
Figure 2-6. A SMATed surface observed with a KEYENCE optical microscope.....49
Figure 2-7. Micro-scale defects (marked in red) observed on a SMATed surface by SEM. 50
Figure 2-8. Scanning profiles of specimens in (a)AM; (b)MP; (c) SMAT states. ...51
Figure 2-9. (a) MMT 3D measuring machine; (b) specimens fixed on the SEIFERT XRD machine in LASMIS UTT. 53
Figure 2-10. Schematic of the material removal.....53
Figure 2-11. Residual stress profiles of a SMATed specimen (a) before and (b) after correction. 55
Figure 2-12. Residual stress profile of MP and SMAT specimens. 56
Figure 2-13. Hardness profile measured on AA7075 alloy in as-received (labelled “HT”) and SMAT (labelled “HT-SMAT 1000”) states [148]. 57
Figure 2-14. Tensile test curves of AA7075 in as-received (labelled “HT”) and SMAT (labelled “HT-SMAT 1000”) states [147]. 58
Figure 3-1. Fatigue testing machine Instron ElectroPuls E10000 with a specimen fixed on it 59
Figure 3-2. Input signal of axial and torsional loadings. 60
Figure 3-3. S-N plot of biaxial fatigue tests for specimens in MP state. 61
Figure 3-4. S-N plots of fatigue tests for specimens in MP and SMAT states. 62
Figure 3-5. Basquin equation fitting of (a) MP state; (b) MP and SMAT states. ..64
Figure 3-6. P-S-N fitting of (a)MP state; (b)MP and SMAT states.....66
Figure 3-7. 2-part fitted P-S-N curves of MP state. 66
Figure 3-8. (a) fracture surface of an MP state specimen tested at a high stress amplitude (368MPa); (b) a zoom-in figure of the multiple initiation sites..69
Figure 3-9. Different crack propagation stages in the case of high stress amplitude: (a) microscope image; (b) schematic. 70
Figure 3-10. Fracture surface of a MP specimen tested at 280MPa.....71

Figure 3-11. (a)(b) Observation of crack initiation on the lateral surface (tested at 280MPa); (c) a close-up of the crack initiation site. 73
Figure 3-12. Fracture surfaces of MP states tested at: (a)368MPa; (b)280MPa; (c)220MPa. 73
Figure 3-13. Observation of the crack initiation site of MP state tested at 220MPa: (a) Optical microscope; (b) SEM. 74
Figure 3-14. Dependence of cracking modes on material parameter b for fully reversed uniaxial and pure torsion loading[126] 76
Figure 3-15. Fracture mechanism map for AA7075T6 alloy under combined axial and torsional loading [127] 76
Figure 3-16. Observation of fracture surfaces of: (a) MP state 368MPa; (b) SMAT 280MPa; (c) MP 280MPa. 77
Figure 3-17. Fracture surface of SMAT specimens tested at: (a)260MPa;(b)230MPa. 78
Figure 3-18. Lateral surfaces of SMAT state specimens tested at: (a) 280MPa; ..78
Figure 3-19. The SMAT-affected zone in a SMAT 220MPa case observed by SEM. 79
Figure 4-1. Microcracks observed with SEM on a SMATed surface 82
Figure 4-2. Schematic of the electropolishing device for cylindrical specimens .83
Figure 4-3. (a) Set-up of the electropolishing device in the lab; (b) a specimen to be polished 84
Figure 4-4. Comparison between surfaces in SMAT and SMAT-EP states: (a) SMAT; (b) SMAT-EP; (c) details of SMAT surface; (d) details of SMAT-EP surface. ..85
Figure 4-5. Profile of (a) SMAT and (b) SMAT-EP surface. 86
Figure 4-6. Comparison in S-N plots of (a) SMAT and SMAT-EP; (b) MP and SMAT-EP. 87
Figure 4-7. Image of fracture surface of a SMAT-EP specimen tested at 300MPa 89

Figure 4-8. Crack initiation angle of a SMAT-EP specimens tested at (a) 260MPa; (b) 240MPa.....90
Figure 4-9. (a) fractography of a SMAT-EP specimen tested at 240MPa; (b) SEM image of (a) with an interior crack initiation site observed.....91
Figure 4-10. Evolution of residual stress and FWHM during cyclic loading: (a) 300MPa; (b) 240MPa. And (c): coordinate system of the cylindrical specimen 94
Figure 4-11. Evolution of residual stress and FWHM during post-SMAT heat treatment. 95
Figure 4-12. S-N plots of SMAT-HT specimens compared with SMAT state.....96
Figure 4-13. (a) Microscopic image of the fracture surface of a SMAT-HT specimen tested at 240MPa; (b) Observation in the direction marked in blue in (a)..97
Figure 4-14. S-N plots of SMAT-EP-HT compared with MP state 98
Figure 4-15. Profile distribution of SMAT-RS and MP-RS 100
Figure 4-16. S-N plots of MP-HT tests compared with MP state 100
Figure 4-17. S-N plots of specimens in SMAT, SMAT-EP and MP-HT states 102
Figure 4-18. Comparison in S-N plots between MP, MP-HT and SMAT-EP-HT states 103
Figure 5-1. S-N curve of both base and SMATed AA7075 obtained from (a) tension-compression tests and (b) torsional tests[147]. 108
Figure 5-2. Schematic of stress state in tension-compression tests.....110
Figure 5-3. Schematic of the plane stress state of SMATed surficial material ...113
Figure 5-4. Comparison between predicted fatigue strength and experimental data of MP specimens.....114
Figure 5-5. Prediction on fatigue strength of SMATed AA7075 115
Figure 5-6. Prediction on fatigue strength of SMAT-EP AA7075 with stabilized value of residual stresses 116
Figure 5-7. S-N slot of experimental and predicted data from (a) MP state tests,

(b) SMAT state tests and (c) SMAT-EP state tests. 118
Figure 5-8. Measurement of average space of dimples on a SMATed surface .. 120
Figure 5-9. Prediction on fatigue strength calibrated using factor Kt 121

General Introduction

Surface Mechanical Attrition Treatment (SMAT) is a promising surface treatment technique for enhancing the mechanical properties of metallic materials. The technique involves high-frequency multidirectional impacts, which generate a nanostructured layer at the surface of a part, as well as a high compressive residual stress profile and a work hardening gradient in the subsurface area. It has been demonstrated that SMAT can enhance mechanical properties, especially fatigue strength, for various materials under different loading conditions.

The 7075 Aluminum Alloy (AA7075) is a widely utilized material in the aerospace and automotive industries. Components manufactured from AA7075 are often subjected to complex working conditions, such as multiaxial loading. Consequently, there has been a significant focus on the fatigue properties of AA7075.

The objective of this study is to investigate the fatigue properties of AA7075 treated by SMAT treatment under combined tension-compression/torsion loading conditions. The uniaxial fatigue properties of SMATed AA7075 have been studied in LASMIS UTT by Yizhuo LI[1], and the present work is carried out on this basis. In Chapter 1, a literature review is present on the basic elements of SMAT and its effects on mechanical properties, especially fatigue properties. A brief introduction of the aluminum alloy 7075 is also given.

In Chapter 2, the pre-SMAT processes are firstly illustrated, including a non-standard heat treatment and mechanical polishing. The SMAT device and process parameters are introduced. Post-SMAT characterizations, such as surface roughness and residual stresses measurement, are present. The results of characterizations indicate that the mechanical properties of SMATed AA7075 are improved, while the surface roughness is significantly increased.

The experimental procedure of the biaxial fatigue tests and the results of fatigue tests are present in Chapter 3. The biaxial fatigue tests are performed under proportional tension-torsion combined loading condition, with a frequency of 5Hz. The

results of fatigue tests are illustrated in S-N plots, Basquin equation and P-S-N curves. A minimal difference has been found between mechanically-polished (MP) and SMATed specimens at high and intermediate load levels. A decrease in fatigue lives is observed at low load levels. The fractographic observation is performed with both optical microscope and SEM, and the results reveal the difference in fracture mechanism between specimens in MP and SMAT states. The deteriorated surface integrity is considered the main detrimental factors contributing to the decreased fatigue strength after SMAT.

In Chapter 4, the factors induced by SMAT are examined individually, including surface integrity, the compressive residual stress layer and the grain refinement. Specially-designed experiments with different post-SMAT processes are performed in order to eliminate certain factors. Such post-SMAT processes include electropolishing, annealing and their combination. Results of these experiments indicate that the existence of beneficial and detrimental factors and their competition contribute to the complex effect of SMAT on biaxial fatigue properties.

Fatigue life estimation is performed with several typical multiaxial fatigue criteria in Chapter 5. Comparison is made between the predicted and experimental values of fatigue lives. The Crossland criterion is found capable of predicting the fatigue lives of specimens in MP state with the highest accuracy. An over-estimation of the fatigue strength of specimens in SMAT and SMAT-EP (SMATed and electropolished) states is observed for all fatigue criteria.

Chapter 1 Literature review

1.1 Basic elements of SMAT

The durability and performance of mechanical components are of paramount importance in ensuring safety and economic efficiency in a multitude of applications. One approach to enhance their service life is through mechanical surface treatments, which are increasingly used due to their simplicity and effectiveness in industrial settings. These treatments, including shot peening and deep rolling, induce significant plastic deformation near the surface, resulting in the formation of a residual stress field and a work-hardened region [2–6]. One of the principal outcomes of these treatments is the generation of compressive residual stress, which has been demonstrated to enhance material durability, particularly in the context of fatigue resistance. This is achieved by enhancing crack initiation resistance and reducing the crack propagation rate [7–10].

Approximately two decades ago, researchers discovered the phenomenon of superficial nanocrystallization during severe plastic deformation induced by surface treatments such as shot peening [11,12]. Since then, a plethora of techniques based on the principle of shot peening, able of nanocrystallizing the material surface, have been developed and investigated. These techniques include Severe Shot Peening (SSP), Ultrasonic Shot Peening (USSP), and Ultrasonic Impact Peening/Treatment (UIP/UIT). Ultrasonic shot peening uses the vibration of a sonotrode powered by an ultrasonic generator operating at a very high frequency (normally 20 kHz). Among the various ultrasonic shot peening techniques, Surface Mechanical Attrition Treatment (SMAT) has emerged as one of the most extensively studied methods. SMAT involves repetitive multi-directional impacts between the material surface and spherical shot propelled with high kinetic energy [13,14]. During SMAT, the near-surface region of the material undergoes repeated impacts from spherical shot with high strain rates and random impact angles, leading to progressive refinement of grain size at the surface. Notably,

the bulk region of the material remains unaffected, preserving its original features and properties. This results in the generation of a gradient microstructure by SMAT, extending from the treated surface to the interior of the material [15–17]. One distinguishing feature of SMAT compared to Conventional Shot Peening (CSP) is its ability to transform the top surface layer of a material from coarse grains to nano-sized grains without increasing a lot the roughness. Despite its typically thin nature, this nanostructured layer can significantly impact the performance of a component by enhancing its mechanical functionality and altering its interaction with the surrounding environment.

Fatigue resistance is consistently recognized as one of the most critical aspects of mechanical properties. To facilitate the industrial adoption of SMAT, it is essential to thoroughly understand the fatigue properties of various materials treated by SMAT. SMAT has been successfully applied to a wide range of pure metals and alloys, including titanium and its alloys, iron and steels, aluminum and its alloys, magnesium and its alloys, as well as zirconium and its alloy.

By modifying the material surface, which includes alterations in hardness, grain size, and roughness, and by introducing compressive residual stress, SMAT has the potential to significantly enhance the fatigue resistance of materials, particularly in regimes such as high cycle fatigue (HCF) and very high cycle fatigue (VHCF). Additionally, SMAT can exhibit a synergistic effect on fatigue properties when combined with other processes such as heat treatment or other treatments including nitriding. A comprehensive understanding of the fatigue behavior of SMAT-treated materials is essential for the advancement of its industrial application and the maximization of its benefits.

1.1.1 Concepts of SMAT

SMAT, also known as one kind of ultrasonic shot peening, mainly uses ultrasonic vibration generated by a piezoelectric transducer. The schematic representation of the SMAT setup is depicted in Figure 1-1. In this process, metallic or ceramic balls, typically ranging from 1 to 8 mm in diameter, are initially positioned at the base of a cylindrical chamber. Subsequently, the bottom of the chamber (called sonotrode) is subjected to

vibration by an ultrasonic generator, causing the balls to be propelled towards a specimen at speeds reaching up to 20 m/s [18]. Due to the high frequency of the vibration (20 kHz), the specimen surface experiences impacts from numerous balls within a short duration. As illustrated in Figure 1-1b, each impact induces a plastic deformation in the material at a high strain rate. The formation of a nanostructured layer in the near surface region of the specimen is a consequence of repetitive impacts from various directions.

A diverse range of metallic materials has undergone treatment via SMAT, encompassing pure metals such as titanium (Ti) [19–22], aluminum (Al) [23], copper (Cu) [24], iron (Fe) [13], zirconium (Zr) [25] and alloys such as Cu alloys[26], Ti alloys [27], Al alloys[28–31], steels [32,33], Mg alloys[34–37]. These materials can be categorized based on various factors, including atomic structure and strengthening mechanisms, which may be associated with their stacking fault energy (SFE). In most cases, SMAT can generate a nanostructured layer on the surface of these materials, provided that the treatment intensity is sufficiently high and other process parameters, such as duration, are appropriately adjusted. Moreover, the resulting surface integrity after SMAT can vary for different materials, influenced by factors such as their ductility.

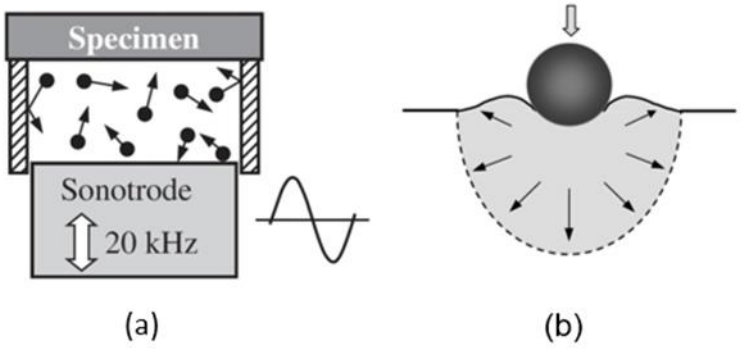

Figure 1-1. (a) Schematic description of SMAT set-up, and (b) a single impact between a ball and the material surface, which generates a local plastically deformed region [14]**.**

1.1.2 Modifications induced by SMAT

1.1.2.1 Microstructure and Nanocrystallization

In comparison to conventional shot peening (CSP), one of the defining

characteristics of SMAT is its ability to transform micrometer-sized grains into nanometer or ultrafine-sized grains. The grain refinement process during SMAT is facilitated by multi-directional plastic deformation. The plastic strain induced by SMAT results in the generation of high-density dislocations, which can organize into various configurations, including geometrically necessary boundaries, incidental dislocation boundaries, or dense dislocation walls [28,34,38]. The plastic deformation behavior and dislocation activities are primarily influenced by two factors: SFE and the number of slip systems in the metal, which is correlated with its atomic structure [39]. For example, in face-centered cubic (FCC) and body-centered cubic (BCC) metals, dislocation walls and cells are formed to accumulate strains, and sub-boundaries are established to subdivide coarse grains if the SFE of the metal is relatively high. Conversely, twinning plays a significant role in the initial deformation stage if the SFE is medium or low. This is evidenced by the findings of [13,28,36]. In the case of hexagonal close-packed (HCP) materials, twinning tends to be the dominant deformation mechanism due to the limited number of slip systems [36], as illustrated in Figure 1-2. It is also important to note that mechanical twinning can be further promoted by other processing factors, such as low temperature [40–44] or high strain rate [14,41–43].

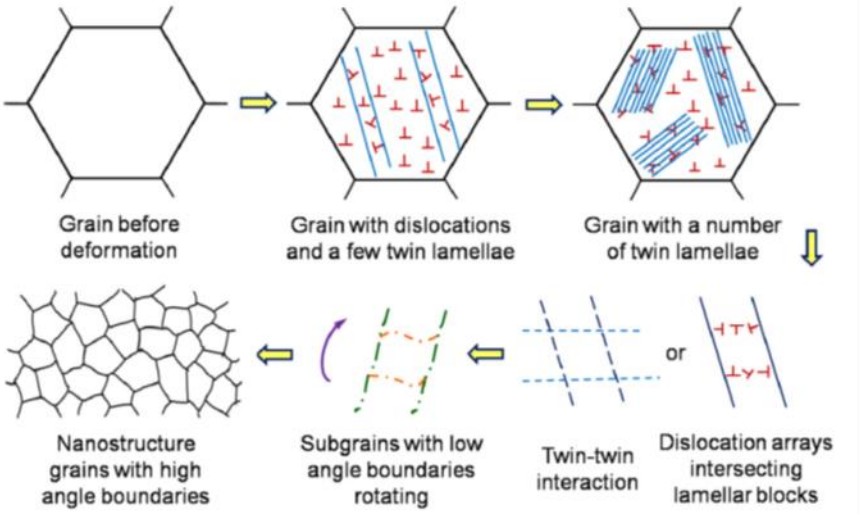

Figure 1-2. Schematic description of the grain refinement process during SMAT [36]**.**

In the case of certain stainless steels, such as 304L steel, where phase transformation can occur during SMAT [45], the grain refinement process is governed

by the formation of a nanometer-sized martensite phase induced by the ultrasonic frequency strikes. This is attributed to the relatively short ultrasonic period of approximately 50 μs, which restricts the growth of martensite, resulting in the attainment of nanometric grains at the surface [46].

A summary of the grain size values observed in the nanocrystalline layer of various materials treated by SMAT is presented in Table 1-1.

Table 1-1. Grain size in nanocrystalline layer of several SMATed materials.

Material	Type of Treatment	Grain Size (nm)	Reference
AA 2014	SMAT—10 min	31	[47]
AA 7075	SMAT—300 s	16 ± 3	[29]
SS 316L	SMAT—15 min	20	[7]
SUS 304	UNSM *-90 N	~10	[46]
Ti-6Al-4V	SMAT	115	[48]
C-2000 alloy	SMAT	~12	[49]
Zr-4 alloy	SMGT *	161	[50]
AZ91D alloy	SMAT	30 ± 5	[39]
Ni3Al	SMAT	45	[51]

*** UNSM – ultrasonic nanocrystal surface modification; SMGT—surface mechanical grinding treatment.**

1.1.2.2 Surface Hardness and Roughness

Following the SMAT process, there is a discernible increase in surface hardness, with values gradually declining from the surface towards the bulk material. In the nanocrystalline layer, peak hardness values of up to several gigapascals can be achieved.

As illustrated in Fig. 1-1(b), the severe plastic deformation induced by SMAT may result in a treated surface exhibiting higher roughness than its initial state. Significant increases in surface roughness have been observed across a range of materials. Nevertheless, the post-SMAT surface roughness is typically lower than that obtained after CSP [27,52,53].

A summary of surface hardness and roughness values for various materials processed by different mechanical surface treatments, including SMAT, is provided in Table 1-2.

Table 1-2. Surface hardness and roughness values of several materials treated by SMAT and other processes.

Material	Type of Treatment	Microhardness		Surface Roughness R_a (μm)	
		Bulk	Surface	Initial	Treated
AA 7075-T6 [54]	SMAT	157 $HV_{0.025}$	180 $HV_{0.025}$	0.35	1.11
AA 2014[47]	SMAT	190 HV	246 HV	-	-
SUS 304 [46]	UNSM	250 HV	540 HV	0.35	0.95
SS 316L [53]	SMAT	200 $HV_{0.025}$	380 $HV_{0.025}$	~2	~1.5
	CSP	200 $HV_{0.025}$	430 $HV_{0.025}$	~2	~3.3
Ti-6Al-4V [48]	SMAT	~3.2 GPa *	~6.9 GPa *	0.1	0.63
X70 micro alloyed steel[55]	CSP	~215 $HV_{0.05}$	~237 $HV_{0.05}$	2.58	3.15
	SSP	~215 $HV_{0.05}$	~244 $HV_{0.05}$	2.58	8.39
Ni3Al[51]	SMAT	~4 GPa *	~12 GPa *	-	-
Zircaloy-4[56]	SMAT	165 HV	215 HV	-	-

1.1.2.3 Residual stress

SMAT is able of generating superficial compressive residual stresses and inducing a

work-hardening layer on materials. In terms of qualitative analysis, the distribution of residual stress resulting from SMAT is comparable to that induced by CSP, due to similarities in impact and deformation mechanisms. Initially, the compressive residual stress peaks just beneath the surface of the material and gradually diminishes with increasing depth. As one progresses deeper into the material, the transition from compressive to tensile stress occurs. Nevertheless, the peak value and thickness of the residual stress layer following SMAT may differ from CSP due to variations in impact angles and kinetic energy. These parameters are contingent on the specific process parameters employed. For example, in the case of AA7075-T6 aluminum alloy, the utilization of steel balls of varying diameters (2 mm and 3 mm) during SMAT has been observed to yield peak compressive residual stresses of approximately -230 MPa and -330 MPa, respectively. A similar outcome can be observed when 316L ASTM F138 austenitic stainless steel is employed [53]. Utilizing 3 mm balls with a coverage ranging from 125% to 3000% during SMAT can result in compressive residual stress reaching a maximum value of approximately -500 to -600 MPa, respectively.

1.1.2.4 Monotonic mechanical properties

The improvement of mechanical properties of SMATed materials have been studied in the past two decades. In the study conducted by Chen et al.[57], dog-bone-shaped tensile specimens with a thickness of 15 μm were fabricated using electro-discharge machining. The specimens comprised a nanostructured layer with an average grain size of approximately 40 nm. The tensile stress-strain curve of the SMAT-treated specimen exhibited significantly enhanced strength compared to its as-received counterpart. The yield strength reached 1450 MPa, approximately six times higher than that of the as-received specimen. However, this increase in strength was accompanied by a reduction in ductility. The elongation to failure of the SMAT-treated specimen was notably decreased, with an elongation at failure of 3.4% (see Figure 1-3). This indicates a significant reduction in ductility for the SMAT-processed specimen, as reported by Chen et al. [57].

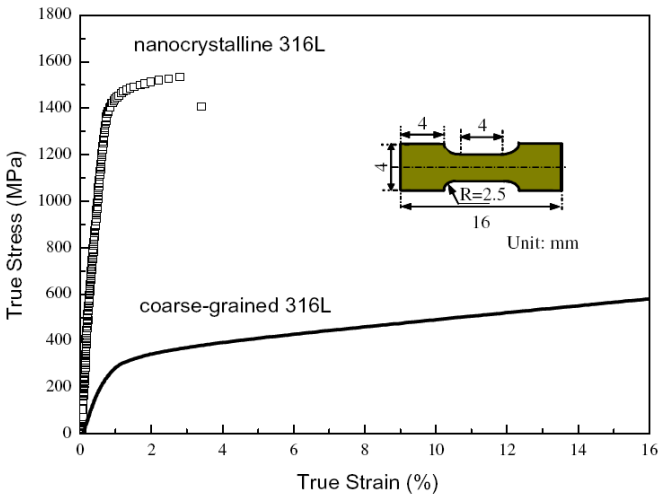

Figure 1-3. Tensile true stress-strain curve for the SMAT processed specimen, compared with the curve obtained for the specimen in as-received state, in 316L stainless steel [57]**.**

In a number of studies, including those on 316L steel [58], pure aluminum[23], and Mg-Gd alloy [59], tensile tests were conducted on sheet specimens with thicknesses ranging from 0.5 mm to 1 mm, treated with varying SMAT intensities. The results indicate that, in comparison to the as-received state, specimens subjected to SMAT demonstrate higher yield stress and ultimate stress, less pronounced strain hardening rate, and reduced elongation to failure. Figure 1-4 provides an example of the results obtained for pure aluminum.

The notable enhancement in mechanical strength observed in materials processed by SMAT is primarily attributed to the presence of the nanostructured layer and the strain hardening generated by the impacts during SMAT. Furthermore, in the case of sheet specimens processed by SMAT, other regions, such as those plastically deformed by ball impact, also contribute significantly to the mechanical strength.

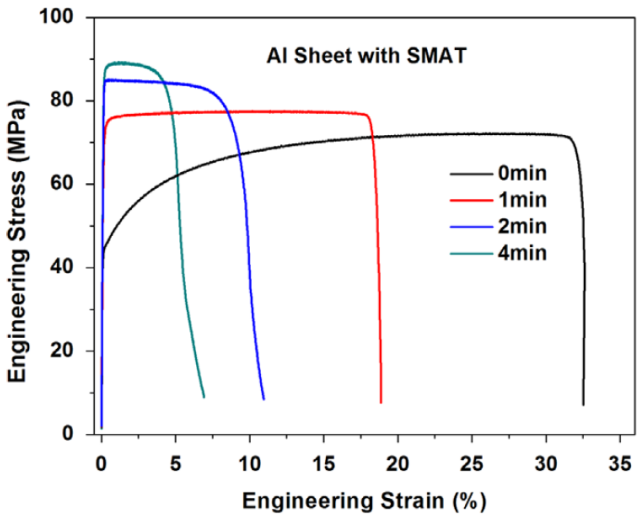

Figure 1-4. Tensile engineering stress-strain curves obtained for pure Al treated by SMAT with different intensities represented by different time durations [23]**.**

While the majority of experimental tests have traditionally been performed under tensile loading, recent research has employed micro-pillar compression to investigate the mechanical properties of the gradient microstructure of 316L stainless steel generated by SMAT [60]. In this method, micro-pillars were milled using Focused Ion Beam (FIB) within the cross-section of the SMAT-affected region, including the nanostructured layer. Subsequently, monotonic compression tests were conducted using a plat punch mounted in a nano-indenter with the objective of investigating the mechanical behavior of the nanostructured layer under compressive loading.

The micro-pillar has an upper diameter of 2.5 µm and a lower diameter of 3.5 µm, with a height of 10 µm. The technique allows the evaluation of local mechanical properties with high spatial resolution. The results indicate that the stress level for micro-pillars located in the nanostructured layer (1600 MPa) is significantly higher than that in the non-affected SMAT region (600 MPa). Moreover, micro-pillars at different distances from the treated surface exhibit different deformation mechanisms.

The effectiveness of this micro-pillar compression technique, in conjunction with EBSD observation, in characterizing the gradient microstructure generated by SMAT has been demonstrated.

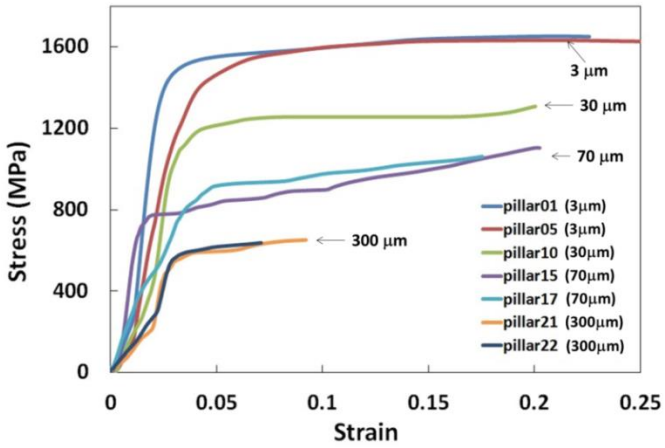

Figure 1-5. Engineering stress-strain curves obtained by monotonic compression tests for micro-pillars milled in a SMATed cross-section sample at different distances from the treated surface[60]**.**

1.1.2.5 Resistance to corrosion

The impact of SMAT on the corrosion resistance of various materials has been extensively studied, including titanium[61] and its alloys[62], stainless steels like 316L [63], 303[64], and 304L[65], as well as Zr[66], Al alloys[67], and 690 Ni-based alloy [63]. In the context of biomedical applications, such as orthopedic and dental implants made from SMATed Ti alloys, it is of paramount importance to assess their resistance to corrosion in vivo, given that the chemical environment of body fluids is highly aggressive for metals[61,68]. Similarly, in structural applications such as components in nuclear reactors and aerospace, corrosion properties are of paramount importance.

The majority of these studies have demonstrated a positive effect of SMAT on the corrosion resistance of materials. This enhancement is primarily attributed to the presence of a nano-sized grain layer formed during SMAT, which facilitates the dilution of segregated alloying elements at grain boundaries[61,63,68] and the formation of effective passive protective films on the nanostructured layer[25,63,67].

For example, Figure 1-6 demonstrates the presence of elements such as Mo, Zr, and Sn segregated at grain boundaries in a Ti-25Nb-3Mo-3Zr-2Sn titanium alloy. The peak intensities of the segregated alloying elements in the as-SMATed sample exhibit a decrease at the grain boundaries, indicating that the SMAT-induced grain refinement

results in the dilution of these elements at the grain boundaries. This dilution by grain size reduction appears to be an effective method to enhance corrosion resistance.

Nevertheless, the beneficial effects of SMAT on corrosion properties may be offset by negative factors such as surface roughness, strain-induced martensite, and dislocations[64].

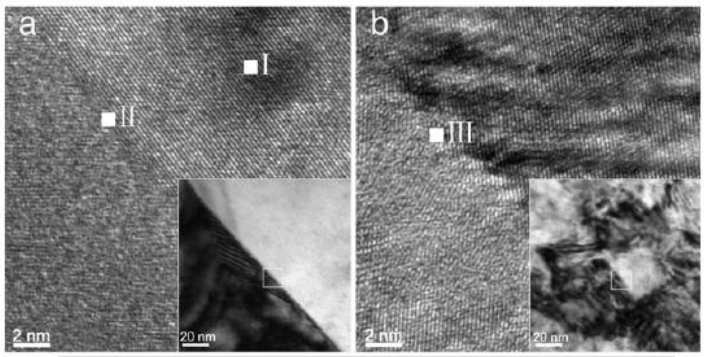

Figure 1-6. HRTEM (High Resolution TEM) images of the squares marked in the inserted TEM bright-field images taken from (a) the solution-treated and (b) the as-SMATed samples[68]**.**

1.1.2.5 Tribological properties

The comprehension of tribological properties is a multifaceted process, encompassing a multitude of physical and chemical phenomena, including oxidation. The effect of SMAT on friction and wear properties has been investigated across a range of materials, including low carbon steel[69], Mg alloys[70], Cu[71], Ti[19], and 316L steel[72].

In numerous instances, a significant enhancement in wear resistance has been observed in comparison to the original coarse-grained counterpart, particularly under relatively low applied loads. For instance, in low-carbon steel[69] and 316 stainless steel[72], it was demonstrated that the friction coefficient decreased and wear resistance increased due to the presence of the superficial nanostructured layer. This improvement can be attributed to the stability of a mechanical mixed layer, where produced oxides and unoxidized metal are mixed[73], and the high hardness of the nanostructured layer[71]. The high hardness of the nanostructured layer reduces

plowing and micro-cutting under lower loads and plastic removal and surface fatigue fracture at higher loads[69].

In the case of the AZ31 Mg alloy, the gradient nanostructure generated by SMAT confers wear resistance through a distinct mechanism. The gradient nanostructure facilitates the formation of an oxidation layer on the worn surface, which subsequently develops into a more compact layer, thereby enhancing the wear resistance of the alloy[74].

The effect of annealing following SMAT on tribological properties has also been investigated. It has been demonstrated that the tribological enhancement of SMATed 316L steel is greater when annealed at temperatures between 400°C and 600°C than when annealed at lower temperatures. This is due to the fact that after the SMAT process, a greater volume fraction of austenite is transformed into martensite at the surface of the material, thereby increasing its wear resistance. It is generally accepted that martensite has a higher mechanical strength than austenite[72].

Nevertheless, it should be noted that the tribological properties of a material are not always directly related to its general strength. In the case of a GW63K magnesium alloy, wear behavior tests demonstrate that the nanostructured layer generated by SMAT, despite exhibiting enhanced mechanical resistance, exhibits inferior wear resistance compared to the as-received condition. This inferior wear resistance is attributed to the low ductility and toughness of the alloy, which can readily result in surface fracture[70].

1.2 Effect of SMAT on fatigue properties

The investigation into the fatigue properties of materials treated by SMAT encompasses a wide range of materials subjected to diverse fatigue loading conditions. These studies are categorized according to the intensity of the load into three regimes: low cycle fatigue (LCF), high cycle fatigue (HCF), and very high cycle fatigue (VHCF). Moreover, in terms of the nature of the load, a variety of loading types are considered, including uniaxial loading, rotating bending, flexural bending, and multiaxial loading.

1.2.1 Low-Cycle Fatigue after SMAT

In studies of LCF, improvements in fatigue life have been observed for aluminum alloys treated by SMAT. For example, a study conducted on a 2014 aluminum alloy[47] revealed that specimens treated with ultrasonic shot peening exhibited significant increases in LCF life, particularly at low strain amplitudes. After 10 minutes of treatment, fatigue life exhibited increases of 79%, 115%, 280%, and 480% for samples tested at total strain amplitudes of 0.55%, 0.5%, 0.4%, and 0.375%, respectively, in comparison to untreated samples. Similar enhancements were reported for a 7075 aluminum alloy (AA7075) in the study by Pandey et al. [29]. In their work, the fatigue life of samples treated with ultrasonic shot peening for 180 seconds was found to be increased in comparison to untreated samples, while the fatigue life of samples treated for 300 seconds was found to be decreased (see Figure 1-7). The authors concluded that the observed improvement was the result of a combined effect of grain refinement and compressive residual stress. Conversely, the observed reduction in fatigue life was attributed to surface damage caused by over-peening. Furthermore, an AA7075-T651 specimen subjected to Surface Mechanical Rolling Treatment (SMRT) [75] exhibited a 6.5% increase in fatigue strength in the LCF regime. Furthermore, the cyclic response during cyclic loadings with high strain amplitudes was affected. Specimens treated with the method exhibited a more pronounced ratcheting effect and greater asymmetry under high applied strain conditions.

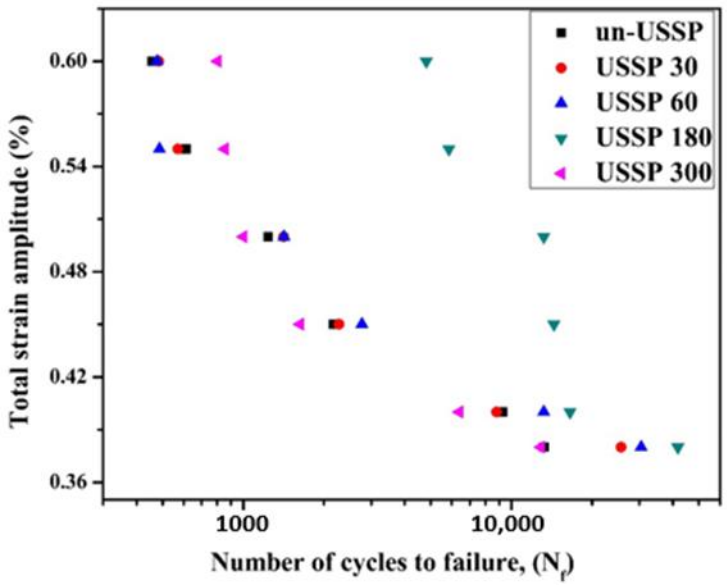

Figure 1-7. Relation between total strain amplitude and fatigue life for untreated and USSPed 7075 aluminum alloy (AA7075) samples (the figures denote the duration of treatment in seconds) [29]**.**

The effect of SMAT has also been investigated in a number of other alloys, including magnesium alloy[76], titanium alloy[77] and IN718 alloy[59,60]. Chen et al. [79] investigated the fatigue strength of AZ31B magnesium alloy treated by SMAT. The results demonstrated a notable improvement in fatigue life for SMAT-treated samples in comparison to coarse-grained samples. Furthermore, samples treated with 3 mm shot exhibited higher fatigue strength than those treated with 2 mm shot. This can be attributed to a thicker deformed layer and higher superficial compressive residual stress induced by larger shot sizes. For the Ti-6Al-4V alloy[80], the fatigue life of specimens treated with ultrasonic shot peening was found to be comparable to that of untreated specimens at the highest applied strain amplitude of ±1.0%. However, at the lowest applied strain amplitude of ±0.60%, the fatigue life increased by a factor of 4.

A study on the LCF behavior of a 316L stainless steel[17] found that the fatigue life of SMAT-treated specimens decreased under high strain amplitude (±1.25%) compared to untreated specimens. Zhou et al. [17] used the Coffin-Manson law and an energy dissipation-based model to analyze the results. The authors concluded that the deterioration in fatigue life is attributed to a decrease in ductility of the surface

layer of the treated material. These findings are consistent with the study performed by Carneiro et al. [81], which revealed that the fatigue strength of 316L stainless steel samples after SMRT is either similar or lower than that of coarse-grained counterparts. Nevertheless, the impact of SMRT on fatigue life in strain-controlled tests becomes positive and discernible when the strain amplitude is lower.

1.2.2 High cycle and very high cycle fatigue after SMAT

In the HCF regime, an improvement in fatigue life is typically observed. Ramos et al. [82] demonstrated that SMAT can enhance the fatigue life of an AA7475-T7351 alloy. For specimens with thicknesses of 4 mm and 8 mm, the fatigue strength up to 10^6 cycles, tested with a stress ratio of R=0, exhibited an improvement of 21.4% and 23.9%, respectively, following SMAT treatment. Furthermore, the fatigue life is found to be enhanced to a greater extent when the tests are fully reversed (R = -1). The fatigue strength up to 10^5 cycles is enhanced by approximately 35% compared to that of untreated specimens. Similarly, Gao et al. reported a significant increase in fatigue life for an AA7075-T6 alloy [54]. The fatigue strength at 1.20×10^6 cycles for samples treated with 3 mm and 2 mm steel balls via SMAT is enhanced by approximately 11.6% and 51.6%, respectively, in comparison to electropolished counterparts.

A multitude of studies have been conducted to evaluate the fatigue life of various steels following surface mechanical nanocrystallization treatment. Roland et al. [7] observed that SMAT-treated 316L steel exhibited approximately a 20% increase in fatigue life compared to untreated counterparts. In their study on 316L and 301LN steels, Uusitalo et al. [83] reported a 50% increase in fatigue limit at 10^7 cycles after SMAT treatment. Dureau et al. [84] observed that the fatigue limit of 304L austenitic stainless steel increased by approximately 20% after SMAT treatment for 60 minutes at room temperature, in comparison to untreated specimens (polished to a mirror finish). Furthermore, SMAT was demonstrated to enhance fatigue strength of SS400 carbon steel by up to 13.1% at 5×10^6 cycles [85].

Significant improvements in fatigue life have also been observed for other metallic materials, including zirconium, C-2000 super alloy, and titanium alloys. For instance,

industrial pure zirconium exhibits an increase in fatigue limit of approximately 28% following nanocrystallization induced by SMAT [86]. Samples of Ti-6Al-4V treated with SMAT for either 30 or 60 minutes exhibited superior or inferior fatigue life, respectively, in comparison to untreated samples. In a study performed by Yan et al. [67], on a selective laser melted Ti-6Al-4V alloy, fatigue resistance was enhanced by approximately 100% compared to the as-fabricated counterparts in both LCF and HCF regimes. In the LCF regime, the fatigue resistance increases from 350 to 675 MPa, while in the HCF regime, it increases from 290 to 580 MPa.

The fatigue properties of welded joints are frequently impaired due to their microstructural and compositional inhomogeneities. Nevertheless, Ultrasonic Impact Treatment (UIT) or Ultrasonic Nanocrystal Surface Modification (UNSM) represents a promising solution for strengthening components with welded joints, due to its capacity to apply directional impacts on material surfaces. The enhancement of fatigue strength in welded joints following UNSM has been widely observed and studied in numerous investigations [87–92]. For instance, Lago et al. [91] demonstrated that UIT can transform tensile residual stresses in welded materials and heat-affected zones into compressive residual stresses. Consequently, the fatigue limit at 10^8 cycles was increased from 370 MPa to 410 MPa for a low-alloy steel, Strenx 700 MC.

In addition to uniaxial tension-compression loading, improvements in fatigue life after SMAT have been widely reported under other loading conditions, including rotating bending [84,93,94] and torsional loading. For example, Dureau et al. [84] demonstrated that SMAT can enhance fatigue life by approximately 30% in rotating bending tests compared to the initial ground state, a more significant improvement than that observed in tension-compression tests. Similarly, in rotating bending fatigue (RBF) study of two 304 stainless steels [94], specimens treated with ultrasonic shot peening exhibited a fatigue limit 80 MPa higher than untreated specimens. Furthermore, rotating bending fatigue tests conducted at room temperature showed that the fatigue strength of an annealed 718 Inconel alloy increased by approximately 42% when subjected to UNSM, as illustrated in Fig. 1-8.

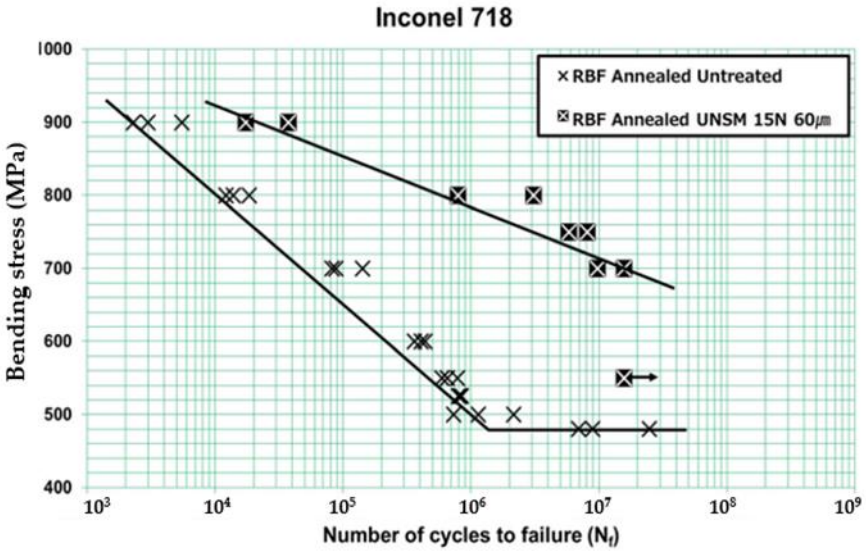

Figure 1-8. S–N curves for the untreated and UNSM-treated annealed Inconel 718 alloy obtained from rotating–bending fatigue (RBF) tests (UNSM with a load of 15 N and an amplitude of 60 μm) [95]**.**

In considering fatigue life under more complex loading conditions, such as multiaxial loading, research has been conducted on nanocrystalline materials treated by CSP [96,97] and SMRT [98]. While studies have reported enhancements in biaxial fatigue life after these treatments, there is a paucity of research on materials treated by SMAT or UNSM.

The VHCF strength of materials treated by SMAT/UNSM has been examined in several studies, including[54,99,100]. Gao et al. [54] observed that specimens of SMATed AA7075-T6 exhibited a lower fatigue limit compared to electropolished specimens. In particular, the fatigue strengths at 1.82×10^8 cycles were reduced by 24.3% and 6.9% for samples treated with 3 mm and 2 mm steel shot, respectively. Interior crack initiation was observed in samples treated with 2 mm shot, while a surface-subsurface multi-initiation mode was noted in samples treated with 3 mm shot. For JIS SCM435 steel[99], the fatigue limit at 10^9 cycles increased by approximately 10% for specimens treated with UNSM under a 40 N load. Furthermore, specimens treated with UNSM under 70 N and 100 N loads exhibited increases in fatigue limit of 20% and 30%, respectively.

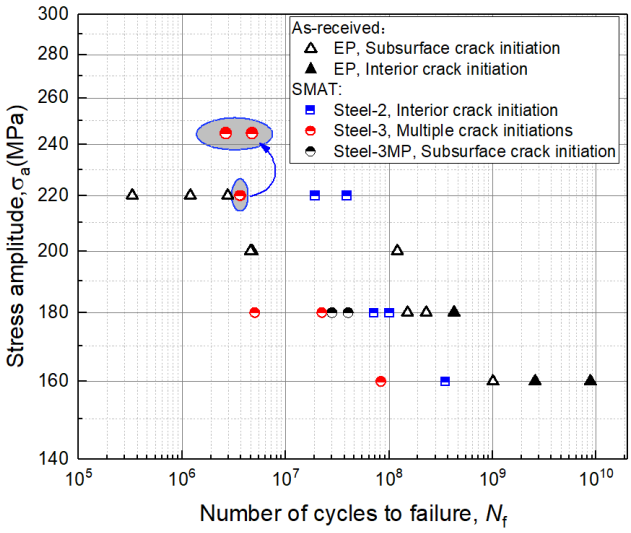

Figure 1-9. S–N plot for the fatigue data points obtained with electropolished (EP) AA7075-T6 samples and samples SMATed under different process conditions, namely, Steel-2 (SMAT using 2 mm steel shot), Steel-3 (SMAT with 3 mm steel shot) and Steel-3 + mechanical polishing (MP) [54]**.**

1.2.3 Factors contributing to the effect of SMAT on fatigue properties

1.2.3.1 Nanocrystallization

It is widely acknowledged that grain refinement plays a critical role in enhancing the fatigue strength of surface-treated materials. This is due to its capacity to impede the initiation and propagation of fatigue cracks [101–103]. These beneficial effects have also been well documented in numerous studies on materials treated by SMAT [46,86,93].

As a result of the nanocrystalline layer induced by surface treatment being typically associated with compressive residual stress and work hardening, post-treatment annealing has been used as a method to reduce the residual stress that occurs after surface treatment. This allows for the individual influence of the nanostructure to be analyzed separately [50]. As illustrated in Figure 1-10(b), after the significant reduction in residual stress after annealing at 400°C for 2 hours, the annealed nanocrystalline Zr-4 samples exhibit a fatigue striation space comparable to that of the as-treated samples, and notably lower than that observed for the coarse-grained samples. This

trend in fatigue striation space is consistent with the fatigue results shown in Figure 1-10(a). This discrepancy indicates that the compressive residual stress is not the primary factor influencing the enhanced fatigue resistance. Rather, it is the nanocrystalline layer itself that plays a critical role.

Another way to analyze the effect of nanostructure is by finite element method (FEM) based numerical simulations. The results of the numerical study conducted by Li et al.[8,10] demonstrate that the nanocrystalline layer and work-hardened region at the surface and subsurface areas play a more significant role in improving the fatigue limit of nanocrystallized C-2000 superalloy samples than the compressive residual stress field. In these studies, finite element (FE) models of the treated materials were constructed. Each FE model was individually configured to include specific surface roughness, work hardening, compressive residual stress, and nanocrystals. A model combining all four features served as a counterpart. Upon the application of relatively high bending loads, plastic strain was observed in the surface of the FE models. The results indicated that the nanocrystalline layer was the most critical factor in enhancing fatigue crack resistance, as indicated by the different values of plastic strain observed.

It is important to consider the stability of the nanostructure, particularly when analyzing its individual effect on fatigue resistance, especially under LCF. The original research conducted by Sun et al. [16] aimed to investigate potential alterations in the microstructure induced by SMAT in the context of subsequent LCF loading. It was observed that new plastic slips were activated in the plastically deformed region, resulting in an increase in grain orientation spread (GOS). Nevertheless, in the nanostructured layer, no significant microstructure changes were observed, likely due to the high dislocation slip resistance in nanocrystalline materials.

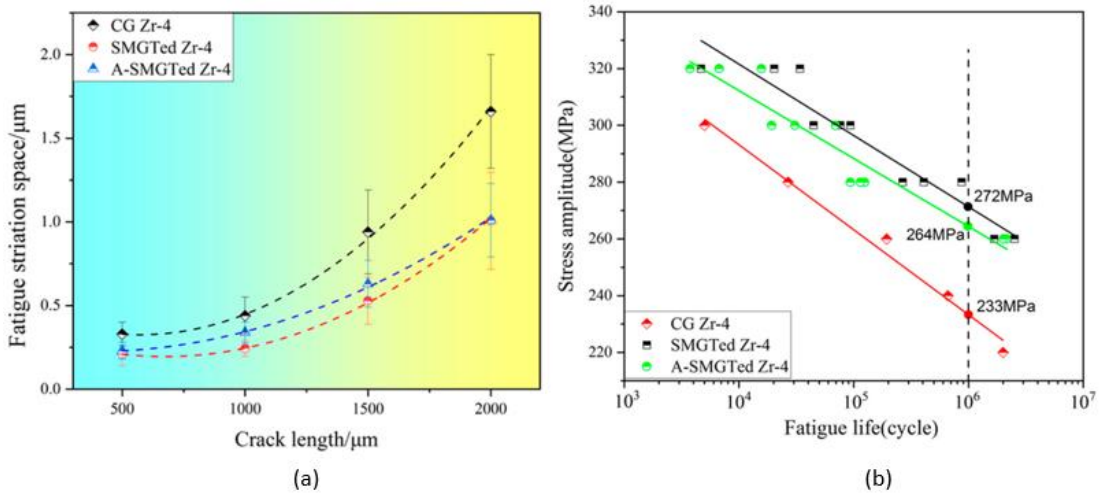

Figure 1-10. (a) fatigue striations space versus crack length curves for Zr-4 with different conditions: CG: coarse grain; SMGTed: after SMGT; A-SMGTed: SMGT and annealed; (b) S–N curves of different Zr-4 SMATed SMGTed samples and SMATed SMGTed samples combined with annealing at 400 °C[50]**.**

1.2.3.2 Residual stress and its relaxation

It is conventionally understood that compressive residual stress impedes both crack initiation and propagation, thereby potentially enhancing fatigue life. This is evidenced by the findings of studies such as those referenced in [85,104,105]. It has been demonstrated that compressive residual stress can enhance resistance to both crack initiation and propagation by reducing the externally applied tensile stress [106].

However, in the case of LCF, the role of compressive residual stress appears to be less critical. For example, in a study on a Ti-6Al-4V alloy[77], an enhancement in fatigue life was observed in specimens treated by USSP followed by a stress-relief treatment (400 °C, 1 h), even though the residual stress induced by USSP was reduced by 50%. A similar phenomenon was observed in a study on an AA2014 alloy treated by USSP[47]. The fatigue life of stress-relieved specimens was found to be more enhanced than that of both USSP-treated and untreated specimens, particularly when the strain amplitude was high. Furthermore, the relaxation of residual stress is a significant factor that should be taken into account. Relaxation of residual stress is primarily a consequence of cyclic plastic deformation during fatigue loading, which is influenced by a number

of factors, including the ductility of the material and the applied load level. In the context of LCF conditions, particularly at high load levels, relaxation is observed predominantly in the early cycles, resulting in a minimal proportion of residual stress remaining by the conclusion of fatigue tests. This phenomenon is illustrated in Figure 1-11. These results indicate that the effect of compressive residual stress on fatigue life improvement is more pronounced at lower load levels.

Conversely, under HCF conditions, where the applied stress level is low, significant plastic deformation at the macro-scale is rarely observed. Consequently, stress relaxation is relatively insignificant, allowing a significant portion of the compressive residual stress state to persist during cyclic loading and even after material failure [107]. However, in the case of VHCF, fatigue crack initiation sites can shift from the top surface to the subsurface region or even the interior of materials. In such scenarios, the tensile residual stress layer beneath the compressive layer in the subsurface region may have a detrimental effect on fatigue strength by promoting crack initiation, as concluded by Gao et al. [54].

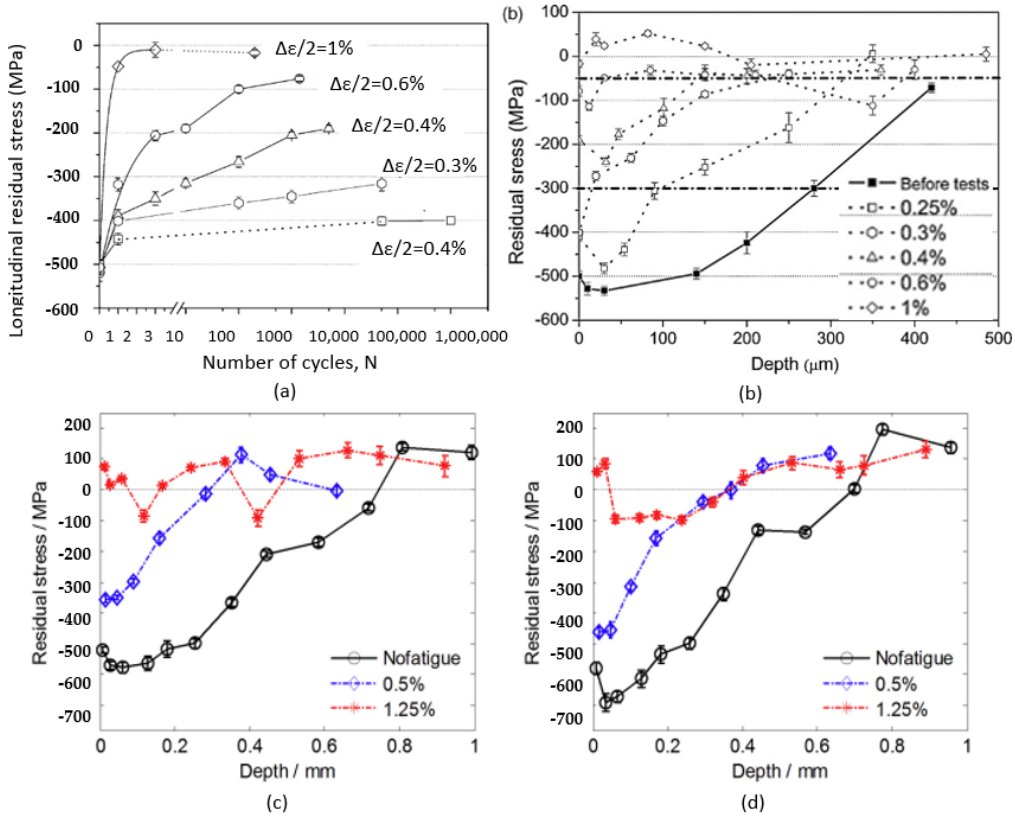

Figure 1-11. (a) Evolution of residual stress at the top surface as a function of the

number of cycles, with different load levels; (b) residual stress profiles with different load levels at N = Nf/2, for a micro alloyed steel [108]**; (c) residual stress profiles of SMATed samples before and after fatigue; (d) residual stress profiles of CSPed samples before and after fatigue, for 316L stainless steel**[109]**.**

1.2.3.3 Surface roughness and integrity

Surface integrity plays a critical role in determining fatigue life. Microcracks induced by severe plastic deformation have the potential to compromise the fatigue strength of materials by creating stress concentrations and facilitating crack initiation [29,93,101,110,111]. In the context of SMAT, it is important to note that excessive peening can result in the formation of surface microcracks. It is evident that these microcracks can have a significant negative impact on fatigue resistance, particularly in materials with high notch sensitivity. For example, the AA7075 alloy is known to be notch-sensitive. Research by Maurel et al. [112] has demonstrated that surface defects induced by SMAT have a profoundly detrimental effect on the fatigue resistance of AA7075 compared to AA2024 counterparts. In the case of VHCF conditions, specimens subjected to SMAT exhibit lower fatigue limits than those that have not undergone this process. The deterioration caused by SMAT is more pronounced in AA7075 specimens treated with 3 mm steel shot, despite the higher superficial compressive residual stress. The presence of micro-damage on the surface results in the initiation of multiple cracks, as illustrated in Figure 1-12. With regard to UIT, since the impact angle is not randomly distributed but directional, weaknesses are formed at the intersecting boundaries induced by UIT, which may potentially lead to subsurface cracks between the surface nanocrystalline layer and the base metal [93].

Surface roughness is commonly considered to be a factor influencing fatigue strength, particularly in processes such as CSP and SSP, which can significantly increase surface roughness due to the high kinetic energy of the shot. Nevertheless, in certain cases, the influence of surface roughness may not be regarded as a significant factor in the enhancement or deterioration of fatigue strength, as high residual stress can

effectively offset the detrimental impact of roughness. Moreover, in certain scenarios, surface roughness can even be improved after UNSM, particularly when applied to structural components such as a ball screw made of AISI 4150H steel [113].

In comparison to CSP and SSP, materials treated by SMAT typically exhibit superior surface quality[82]. Consequently, SMAT is able of inducing a more pronounced enhancement in fatigue life compared to CSP and SSP, contingent upon the effective optimization of the shot size and processing duration[17,54,110].

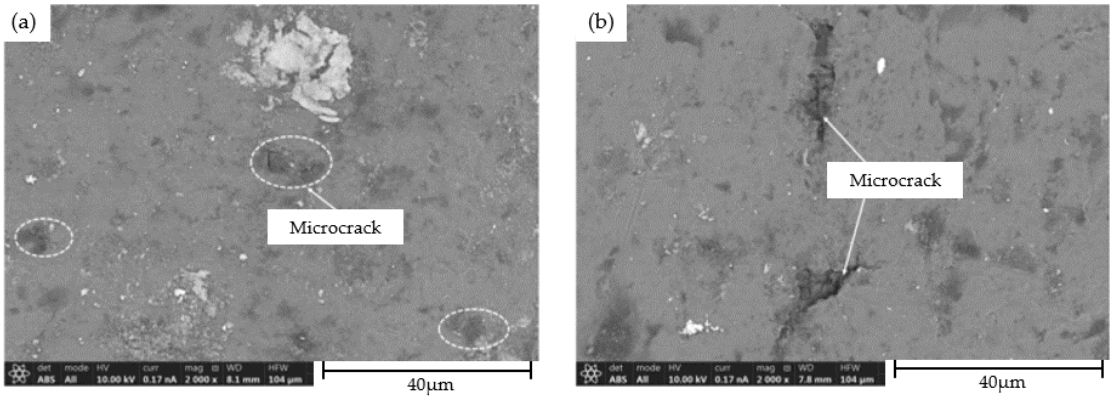

Figure 1-12. SEM observation of microcracks induced by SMAT on an AA7075-T6 alloy with (a) 2 mm steel shots; (b) 3 mm steel shots[54]**.**

1.2.4 Effect of SMAT coupled with other treatment

1.2.3.1 Heat treatment

It has been demonstrated that annealing at 400 °C after surface nanocrystallization significantly improves the fatigue properties of 316L stainless steel, as illustrated in Figure 1-13(c). Although there is relaxation of the superficial compressive residual stress (Figure 1-13(a)), the presence of strain hardening, strain-induced martensitic transformation, and the stable nanocrystalline layer contribute to the observed enhancement in fatigue strength. As illustrated in Figure 1-13(b), the nanostructure remains stable when the annealing temperature is maintained below 500 °C. Kumar et al. [77] also observed a restoration of ductility following post-SMAT annealing [59]. Nevertheless, no concomitant increase in fatigue strength was observed in this study.

Maurel et al. [112] investigated a duplex treatment involving precipitation aging and

SMAT on AA2024 and AA7075 alloys. Aging was performed both before and after the SMAT treatment. The characterization of the microstructures revealed that the microstructure resulting from precipitation aging after SMAT (referred to as S+A) exhibited finer and denser precipitates compared to the untreated core microstructure and the microstructure obtained by SMAT after precipitation aging (referred to as A+S). However, the S+A treated specimens exhibited a comparatively shorter fatigue life than the A+S treated samples. The reduction in fatigue life observed in the S+A-treated samples was attributed to a number of factors. First, in the S+A treatment, SMAT was performed on a softer surface, resulting in higher surface roughness and the formation of fold-like defects. In addition, the relaxation of compressive residual stress caused by the post-SMAT aging process contributed to a reduction in fatigue resistance. For the AA2024 alloy, the fatigue resistance after A+S treatment was 25% higher than that after S+A treatment, while for AA7075, the difference was 20%. It is noteworthy that the samples of AA2024 processed by S+A exhibited fatigue resistance comparable to that of the untreated samples.

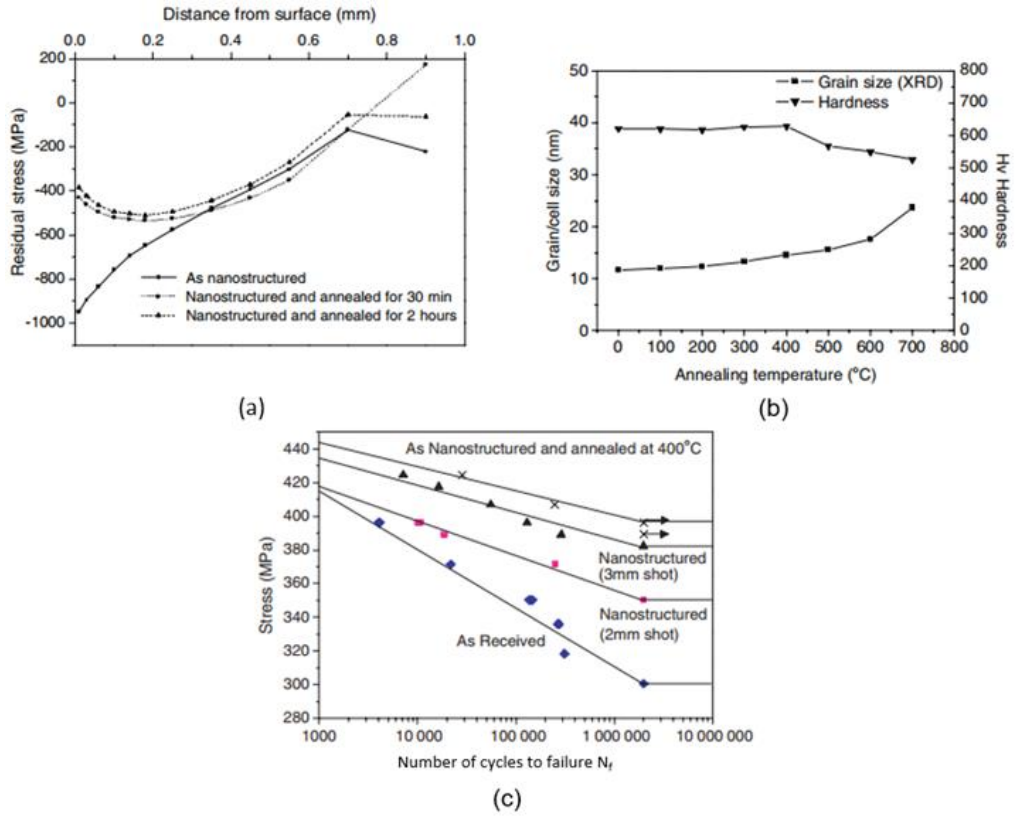

Figure 1-13. (a) Residual stress profiles obtained for different conditions on 316L steel

samples; (b) variation of grain size and hardness with annealing temperatures for the top surface layer; (c) S–N curves of different SMATed samples and SMATed samples combined with annealing[7]**.**

The thermal stability of SMAT-induced modifications is a critical consideration in the development of duplex mechanical-heat treatment processes. This stability has been extensively investigated through the characterization of microhardness and grain size evolution during post-SMAT annealing treatments [23,25,58]. For example, a study performed by[58], examined the thermal stability of a 316L steel nanocrystallized by SMAT over a temperature range of 100 to 800 °C. It was demonstrated that the grain size within the nanostructured layer remained unchanged up to a temperature of 600 °C. This finding is consistent with the observations made by Todaka et al. [32] on various steel types, where annealing at 600 °C for one hour resulted in a significant reduction in grain growth without recrystallization. Similarly, Han et al. [25] investigated the thermal stability of nano-grained pure zirconium (Zr) and found that it remained stable during annealing treatments up to temperatures of 650 °C for 10 hours, beyond which significant grain growth occurred. This conclusion was confirmed by Geng et al. [50] for the Zr-4 alloy. Furthermore, Liu et al. [23] investigated the thermal stability of pure aluminum (Al) through isothermal and isochronal annealing treatments. The study revealed that the nanostructured layer of pure Al generated by SMAT exhibited high thermal stability up to 275 °C, representing approximately 59% of the melting temperature (0.59 Tm). Furthermore, research conducted by Bagherifard et al. [99] indicated that the nanocrystalline layer of a low-alloy steel subjected to surface stress peening (SSP) exhibited good thermal stability up to temperatures of 200 °C and 300 °C for a duration of three hours.

As discussed in Section 1.1, austenitic stainless steel can undergo a phase transformation during severe plastic deformation. Further research conducted by Novelli et al. revealed that the volume fraction of martensite in SMATed 304L austenitic stainless steel samples increase at lower temperatures [2,97]. Another potential advantage of cryogenic temperatures (CT) is that SMAT performed at such temperatures can result in lower surface roughness, which may lead to a more

pronounced enhancement in the fatigue strength of the treated material[114].

In light of the above advantages, Dureau et al. [84] conducted research to evaluate the fatigue strength of a 304L austenitic stainless steel subjected to SMAT at cryogenic temperatures. SMAT was conducted on samples under cryogenic conditions at approximately -100 °C for a duration of 20 minutes. The process resulted in a reduction in surface roughness, an increase in the amount of martensite, an enhancement in surface hardness, and the development of elevated residual stresses in both the γ austenite and α' martensite phases. Despite these improvements, the results of the rotating bending tests indicated that the expected additional improvement was not achieved with CT-SMAT. The increase in fatigue life was found to be nearly identical for samples processed by SMAT and CT-SMAT compared to the initial ground state, as depicted in Fig. 1-14.

Maurel et al. [115] also performed SMAT at cryogenic temperatures on a β-metastable 5553 titanium alloy. The results demonstrated that martensite formation occurs within the kink bands for specimens subjected to SMAT at both room temperature (RT) and cryogenic temperature. However, the latter process facilitates the formation of martensite at a greater depth within the subsurface. Furthermore, the surface roughness of specimens subjected to CT-SMAT is reduced by a factor of four in comparison to those subjected to RT-SMAT. The combination of these observations leads to the conclusion that CT-SMAT results in an 8% improvement in fatigue resistance compared to RT-SMAT.

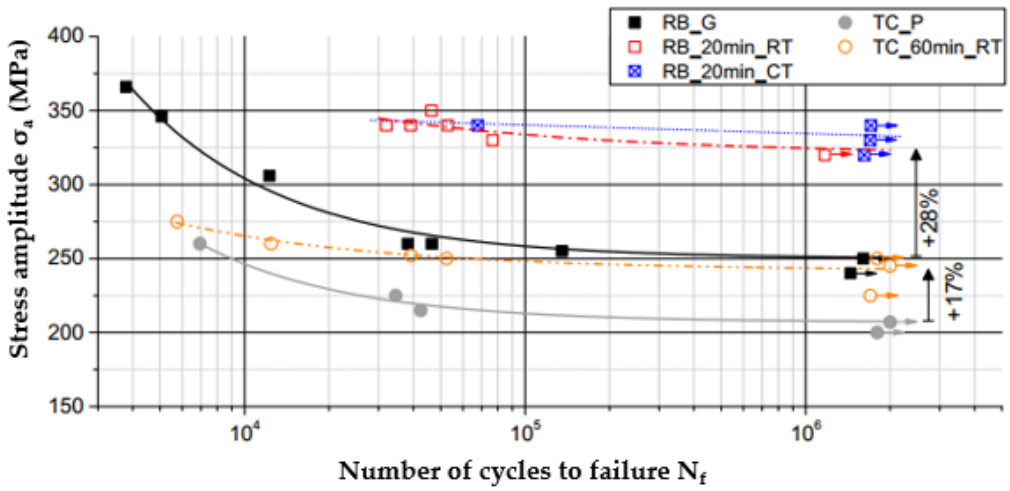

Figure 1-14. S–N curves obtained at 10 Hz fatigue tests for a 304L austenitic stainless

steel (RB: rotating bending; TC: tension–compression; G: ground state; P: polished state; RT: room temperature; CT: cryogenic temperature) [84]**.**

1.2.4.2 Other mechanical surface treatments

Bagherifard et al. [116] investigated a number of techniques to mitigate the adverse effects of high surface roughness on fatigue strength after severe shot peening (SSP). The researchers investigated the effectiveness of re-peening and grinding techniques applied to specimens subjected to SSP. Re-peening with smaller and harder shot yielded promising results, although surface roughness was not significantly reduced. The improvement in fatigue strength was attributed to the introduction of a more homogeneous and regular surface morphology by re-peening.

In a study performed by Amanov et al. [113], a duplex peening process was conducted on an AISI 304 stainless steel. This involved the application of CSP prior to UNSM. The rotating bending fatigue life after each treatment (CSP, UNSM, and CSP+UNSM) was found to be extended in comparison to the fatigue life of the untreated samples. Nevertheless, the fatigue strength after CSP+UNSM was found to be greater than that observed after CSP alone, although it was notably lower than that observed after UNSM alone. This reduction was attributed to surface damage induced by over-peening. The results suggest that a duplex peening approach may be beneficial only to enhance the effects of CSP.

1.2.4.3 Nitriding

Nitriding is a thermochemical surface modification process that has gained considerable attention in the engineering applications. It is distinguished by a multitude of advantages over traditional surface modification techniques. The formation of a unique composite structure consisting of a hard compound layer and a diffusion zone containing submicron-sized nitrides results in a significant improvement in the surface hardness, wear resistance, and corrosion resistance of ferrous materials [102][103]. Nevertheless, it has been observed that the resulting nitrided layer often

exhibits significantly reduced toughness[117].

In a study conducted by Wu et al. [104], UNSM was applied to S42C steel subjected to plasma nitriding for durations of 8 hours (N8) and 48 hours (N48), respectively. Material characterization and fatigue tests revealed the generation of a plastically deformed layer with lower roughness and significantly higher microhardness at the surface of both N8-UNSM and N48-UNSM samples. Furthermore, the thickness of this layer was observed to increase with longer nitriding times. Notably, a significant enhancement in fatigue strength was observed in the N8-UNSM samples, while no improvement was observed in the N48-UNSM samples. The plastic deformation layer was observed to be thicker in the N8-UNSM samples than in the N48-UNSM samples. Furthermore, the locations of inclusions that induced fish-eye cracks were found to be deeper in the N48-UNSM samples compared to the samples subjected to other conditions (Fig. 12(b)).

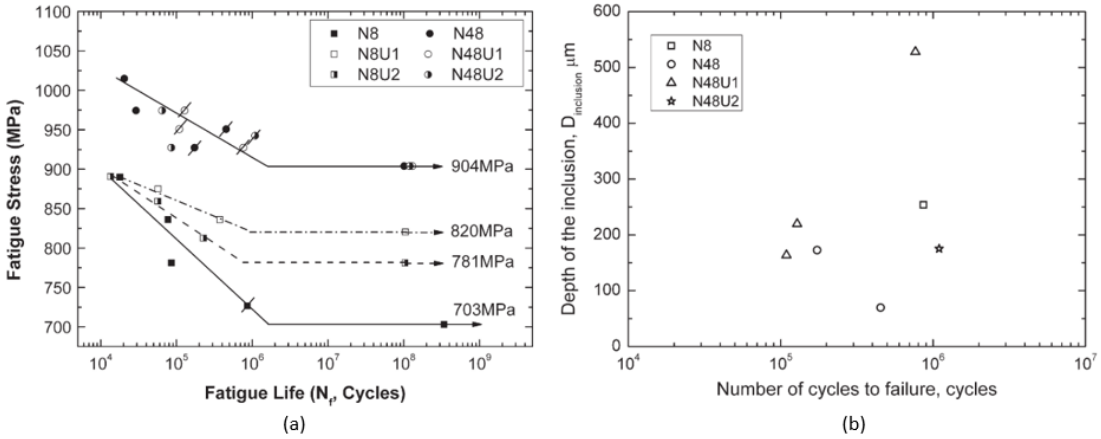

Figure 1-15. (a) S–N plot of samples in different conditions (N8: nitrided for 8 h; N48: nitrided for 48 h; U1: UNSM with a strike number of 34,000 mm−2; U2: UNSM with a strike number of 69,000 mm−2); (b) depth of inclusions inducing fish-eye initiations [104]**.**

1.3 Aluminum alloy 7075

1.3.1 Microstructure of AA7075

The 7xxx series of aluminum alloys, including AA7075, is employed primarily in the aerospace industry due to its exceptional strength and resilience. The mechanical

properties of AA7075 are largely influenced by the presence of second-phase particles, including intermetallic and strengthening particles[118]. Moreover, the microstructure of 7xxx precipitation-hardening aluminum alloys can undergo significant alterations through heat treatments, resulting in substantial changes in their mechanical characteristics[119]. In general, the microstructure of AA7075 is composed of three distinct types of second-phase particles[120,121]: intermetallic (Fe or Si impurities or excessive quantities of major elements), dispersoids (intermetallic particles formed from Zr, Cr, and Mn), and strengthening precipitates (MgZn2). Figure 1-16(a) provides a visual representation of the aforementioned types of second-phase particles in 7xxx series aluminum alloys. An illustration of the microstructure of AA7075, as observed by Pandey et al.[29], is depicted in Figures 1-16. The micrographs demonstrate the presence of larger particles (Figure 1-16 (b)), which are likely to be coarse intermetallic such as Al_3Fe and Al_7Cu_2Fe dispersed throughout the grains of AA7075, as indicated in the literature[122,123]. Figure 1-16 (c) depicts needle-shaped η precipitates ($MgZn_2$) and plate-like η' precipitates within the grains, along with segregated η precipitates at grain boundaries.

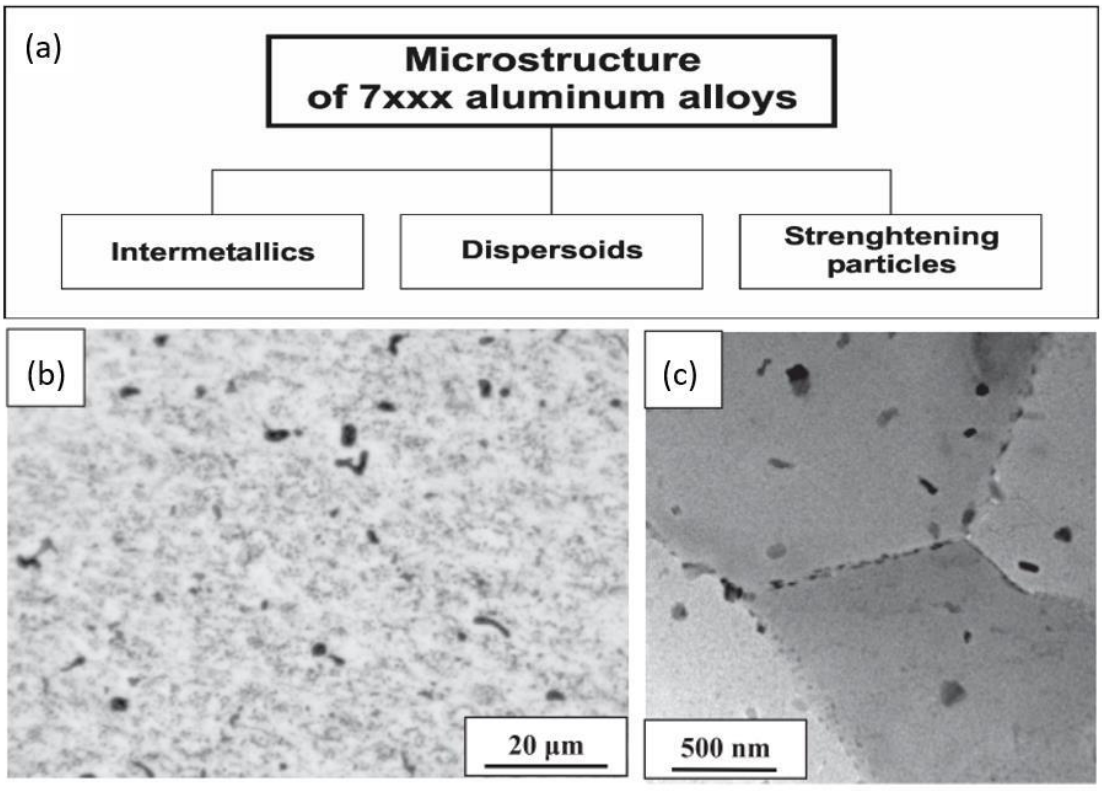

Figure 1-16. (a) Microstructure of 7xxx alloys; (b) optical micrograph; (c) TEM micrograph[29]**.**

1.3.2 Heat treatment of AA7075

In order to achieve high strength in AA7075, it is necessary to perform a heat treatment process in order to enhance the mechanical properties of the material after the forming phase. The T6 heat treatment is a prominent method for optimizing both solution heat treatment and artificial aging, thereby significantly improving the alloy's mechanical characteristics[124]. The T6 heat treatment for AA7075 is well-established within the solution temperature range of 465-490 °C and an aging temperature of 0 °C, as illustrated in Figure 1-17.

The specific processes involved are defined as follows:

1. Solution heat treatment is defined as: This process involves subjecting the alloy to a heat treatment, raising it to an appropriate temperature and holding it at that temperature for a sufficient time to facilitate the constituents entering into a solid solution. The alloy is then rapidly cooled in order to effectively retain the constituents in solution.

2. Aging: This process involves the precipitation of the alloy from a supersaturated solid solution, resulting in a change in the properties of the alloy. Aging may occur in a gradual manner at room temperature (natural aging) or in a more accelerated manner at elevated temperatures (artificial aging).

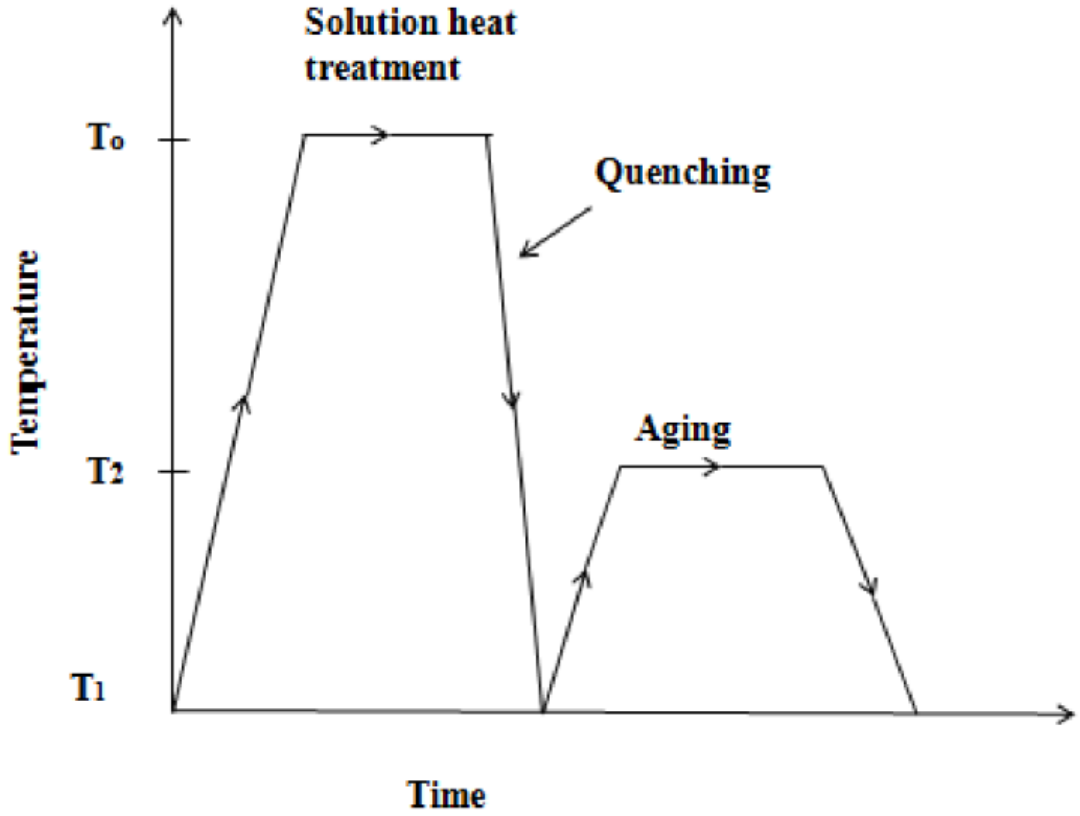

Figure 1-17. Schematic of T6 heat treatment of 7xxx aluminum alloys[125].

1.3.3 Fatigue fracture mechanism of AA7075

The fatigue properties of AA7075 have been the subject of investigation for decades, since this material has been widely used as components in automotive and aerospace industries. In the low-cycle fatigue regime, AA0775-T6 exhibits typical cyclic hardening during the initial stage of fatigue loading, followed by relatively good cyclic stability[126]. Dislocations are found to migrate towards the interface between the precipitates and the substrate, thereby inducing stress concentration. Furthermore, the interface between the second phase particles and the substrate is susceptible to debonding, void formation, and stress concentration under cyclic loading. Therefore, the probability of crack initiation is increased in both cases.

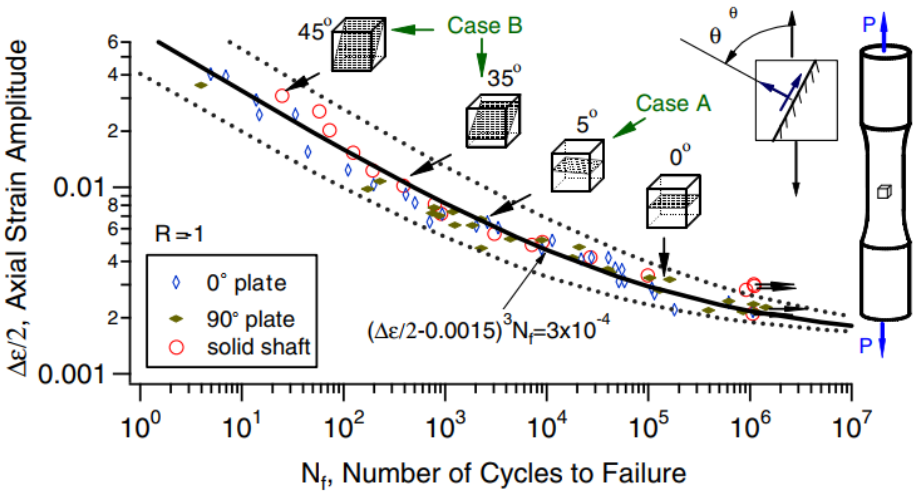

(a) Strain–life and cracking behavior under fully reversed uniaxial loading

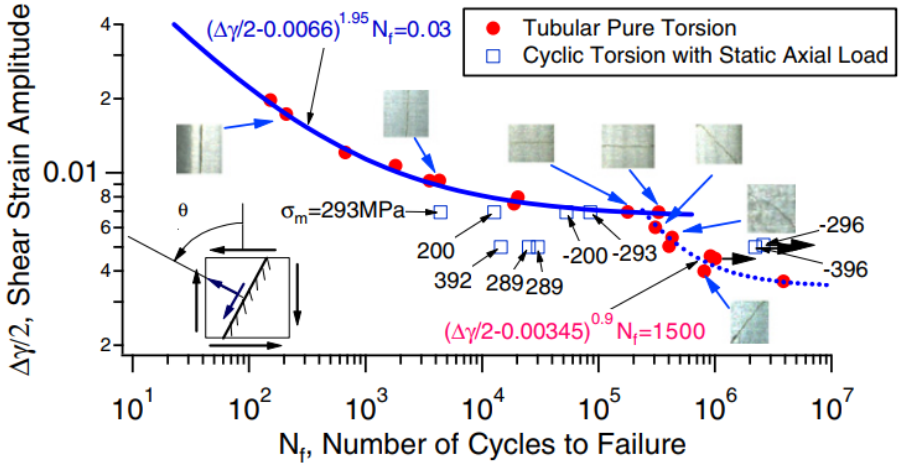

(b) Shear strain amplitude versus fatigue life for pure torsion and torsion with a static axial stress

Figure 1-18. S-N curves and cracking behaviors of AA7075-T651[127]**.**

From low-cycle to high-cycle regime, the AA7075-T651 displays 3 different cracking modes, including shear cracking, mixed cracking, and tensile cracking. The occurrence of different cracking modes is highly dependent on the magnitude of the loading, according to the results obtained by Zhao and Jiang [127]. As illustrated in Figure 1-18(a), the AA7075-T651 exhibits shear cracking behaviors at relatively high load levels under uniaxial loading. As the applied load is reduced, the observed cracking mode changes from shear to tensile. It is considered possible that mixed cracking may occur at intermediate load levels. The same cracking mode transition is also found in the torsional loading condition, as shown in Figure 1-18(b). Furthermore, the mean stress

has been demonstrated to exert a significant influence on fatigue life.

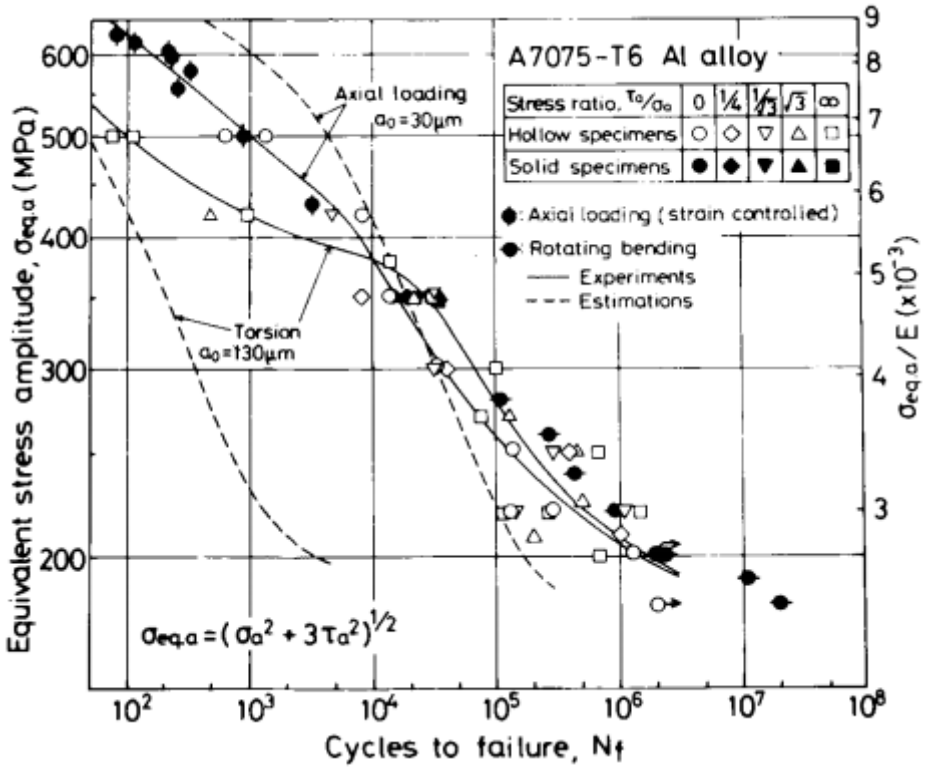

Figure 1-19. S-N plot of AA7075-T6 under uniaxial, torsional and combined loadings[128]**.**

According to the study of Tanaka[128], the S-N diagram of AA7075-T6 tested in axial, combined and strain-controlled loading conditions with both solid and hollow specimens is presented in Figure 1-19. The axial loading curve is steeper in the high cycle regime ($N_f > 10^4$ cycles). The curve in the low cycle regime seems to coincide with the curve of strain-controlled tests. The torsional fatigue strength was slightly higher than that of axial loading in the relatively high cycle regime. However, when the relevant equivalent stress amplitude value increases to more than 400 MPa, the torsional fatigue lives decreased drastically to less than 10% of the axial fatigue lives.

Fatigue fracture modes of AA7075 in relatively complex loading conditions are primarily classified into two types based on the crack growth planes and directions involved: stage I and stage II cracks. Stage I cracks propagate within the plane of maximum shear, involving mode II and mode III crack growth. In contrast, stage II cracks propagate within the plane of maximum principal stress through a mode I crack growth mechanism. The fracture mechanism map was conducted by Tanaka[128] for

better understanding of fracture mechanism of AA7075 in different biaxial loading conditions. It can be seen in the Figure 1-20 that the fatigue strength of AA7075 is sensitive to the fracture modes. The map also helps to explain the crossover of axial and torsional curves at 400 MPa in Figure 1-19. It can be found that for $\tau_a/\sigma_a = 1$, a stage II crack changes to a stage I crack at higher stress levels. While for $\tau_a/\sigma_a = 1/\sqrt{3}$, a stage II crack changes to a longitudinal stage I crack. For $\tau_a/\sigma_a = \sqrt{3}$ and ∞, the circumferential stage I cracks change to longitudinal stage I cracks as load level increases. The preferred circumferential orientation in torsional tests is possibly attributed to the texture structure of FCC materials, which makes it easier for slips to occur in circumferential direction.

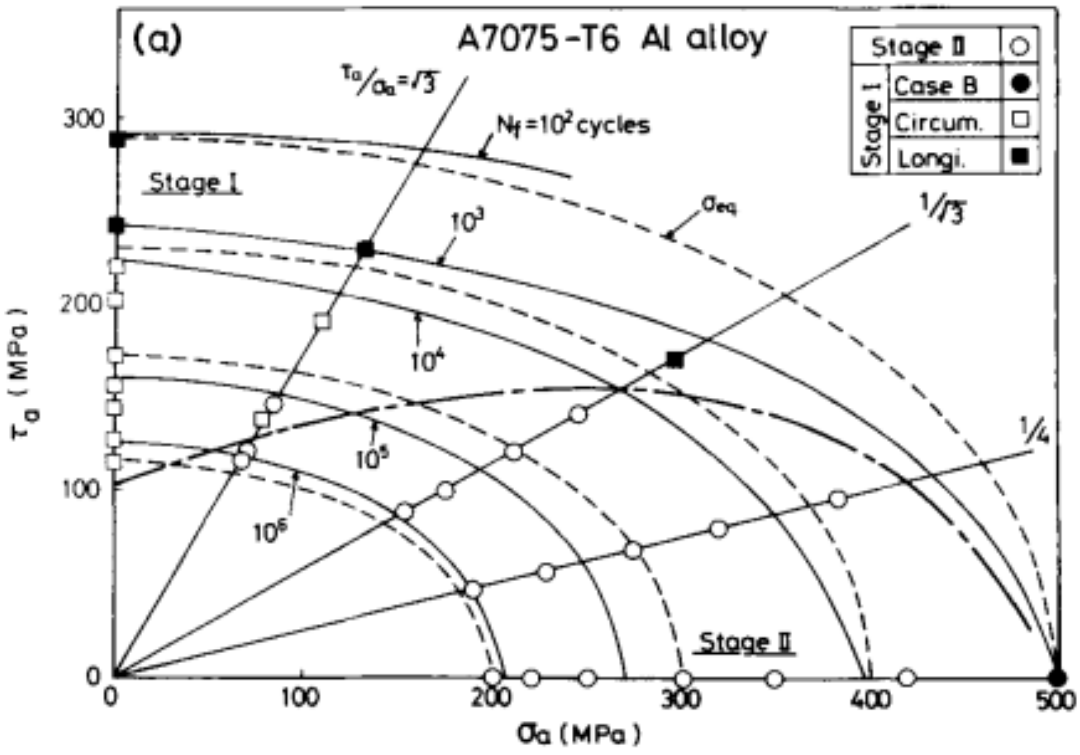

Figure 1-20. Fracture mechanism map of AA7075-T6 in different biaxial loading conditions[128]**.**

For AA7075-T6 subjected to torsion-bending combined loadings, crack nucleation is found on the plane of maximum shear stress and identified as a shear-dominant brittle cleavage fracture[129]. The crack propagation in this biaxial load can be divided into two distinct regions: one dominated by mode I crack growth and the other one by pure

mode II growth, as illustrated in Figure 1-21.

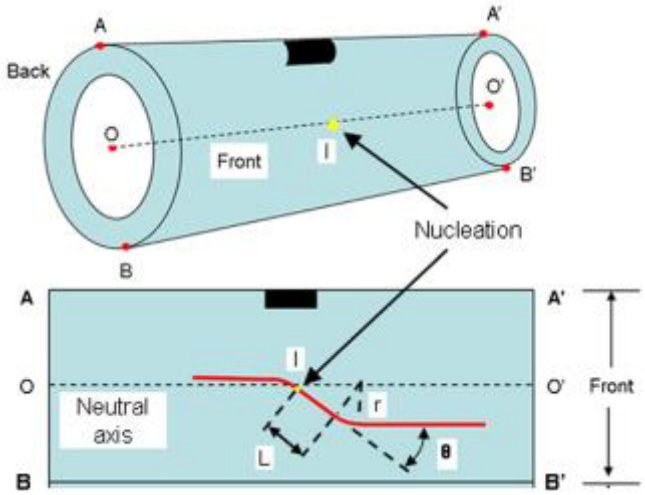

Figure 1-21. A schematic of the crack trajectory of AA7075 tested under in-phase bending and torsional loading[129]**.**

In the lab of LASMIS UTT, some research has already been done on the fatigue properties of SMATed AA7075. Yizhuo's work[1,130] reveals that SMAT could have beneficial effect on uniaxial and torsional fatigue strength of AA7075. However, the effect of SMAT can be highly related with the heat treatment condition. In comparison with the as-machined state, the fatigue lives of SMATed specimens tested under uniaxial loading exhibited an increase under high stress amplitudes, but a decrease under low amplitudes. Conversely, the fatigue lives of heat-treated specimens demonstrated an increase under all the studied stress amplitudes after SMAT.

1.4 Multiaxial fatigue

Multiaxial loads and stress states are commonly encountered in industrial applications, such as those pertaining to the automotive and aerospace industries. Even when a component is operated under uniaxial loading, a multiaxial stress state may still exist due to the presence of geometric constraints such as notches. Multiaxial loadings can be categorized as either in-phase or out-of-phase loads. Systematic research on multiaxial fatigue has been conducted for approximately five decades[131].

1.4.1 Non-proportional hardening

In the low-cycle regime, non-proportional hardening is a common phenomenon observed in metallic materials[132–134], such as steels[101,135]. The extent of non-proportional cyclic hardening is dependent on a number of factors, including the shape, sequence, and amplitude of the loading path, as well as the microstructure of the material. Shamsaei and Fatemi[101] demonstrated that the hardening coefficient of a certain material is contingent upon its microstructure and hardness level. Furthermore, they observed that materials exhibiting cyclic hardening could also demonstrate non-proportional hardening under non-proportional loading, whereas materials exhibiting cyclic softening typically do not exhibit additional cyclic hardening.

In materials with high SFE, such as titanium[136], this additional hardening is rarely observed. As illustrated in Figure 1-22, the cyclic stress response of a 304L stainless steel is markedly elevated when subjected to out-of-phase loadings in comparison to in-phase loadings. In contrast, the cyclic stress response curves for titanium alloy are found to be overlapped.

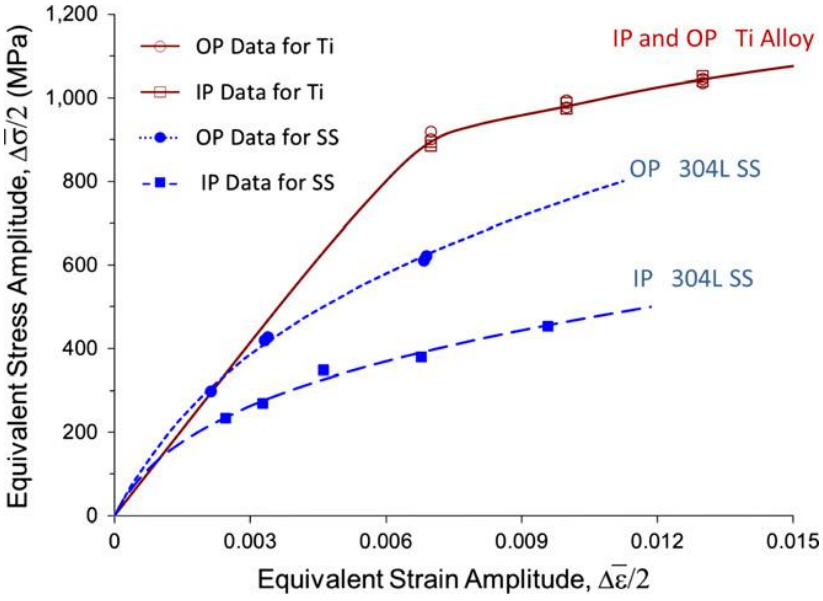

Figure 1-22. Comparison of in-phase (IP) and 90° out-of-phase (OP) equivalent stress–strain data for Ti–6.5Al–3.4Mo (Ti)[136] **and 304L stainless steel (SS)**[101]**.**

1.4.2 Damage mechanism

Studies carried out by Socie[137,138], and Brown and Miller [139,140], have demonstrated that in multiaxial fatigue cases cracks can nucleate and propagate along a preferred direction rather than randomly. The orientation of this preferred plane is primarily dependent on the microstructure characters of the material and the applied stress states. For instance, in a normalized medium-carbon steel, the preferred orientation of cracking is illustrated in Figure 1-23. Obviously, for this 1050 steel, cracks nucleate in the direction where the maximum shear strain exists under an in-phase axial-torsion loading.

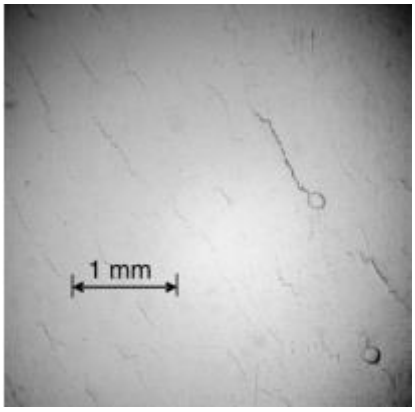

Figure 1-23. Preferred cracking orientations observed for 1050 normalized steel under in-phase axial–torsion loading[141]**.**

1.4.3 Damage criterion and life estimation

Classical yield criteria, such as the von Mises distortion energy criterion, have been extended to multiaxial fatigue regimes. Although these criteria may be effective in cases of in-phase or proportional loadings, underestimation of the typical shorter lives occurs frequently, especially in out-of-phase or non-proportional loading conditions.

The shorter fatigue life observed in non-proportional condition is mainly attributed to the additional hardening phenomenon[142,143]. Nevertheless, materials that do not exhibit additional hardening may also show a shorter fatigue life when tested with non-proportional loadings[136,144,145].

The critical plane approach for estimating multiaxial fatigue strength is thus

established based on the observation of the preferred cracking orientation. The critical plane is observed predominantly on either the maximum shear failure plane or the maximum principal strain or stress failure plane. In shear cases, fatigue damage is primarily driven by shear strain or stress, whereas in principal cases, the driving force for damage is the maximum principal stress or strain.

An illustration of damage distribution with plane orientation for in-phase and 90-out-of-phase axial–torsion loading with the same equivalent strain for Ti–6.5Al–3.4Mo[136] based on the Fatemi–Socie (FS) parameter is presented in Figure 1-24. It can be observed that a higher normal stress on the maximum shear plane for out-of-phase loading results in a higher damage value.

Research conducted over the past decades has demonstrated that critical plane approaches are the most reliable and robust for multiaxial fatigue life estimations. These approaches reflect the physical nature of the fatigue damage process by considering a specific plane or planes with the greatest fatigue damage as the critical plane. Consequently, they are able to identify the orientation of damage, such as cracks. Critical plane approaches are reported to be applicable to both proportional and non-proportional loading conditions.

These approaches can be classified as stress-based, strain-based, and strain-stress-based or energy-based models. Stress-based critical plane models, such as the Findley model[146], may be effective in the context of HCF, where plastic deformation is minimal or non-existent. Strain-based critical plane models, such as the Brown and Miller model[139], are based solely on strain terms. Although these models mentioned above are applicable to both low and high cycle fatigue regimes, the constitutive behavior of the material cannot be revealed and the phenomena such as non-proportional cyclic hardening, cannot be taken into account.

Critical plane models that incorporate both stress and strain have been pronounced the most appropriate for both LCF and HCF, and with the ability to capture the material's constitutive response under non-proportional loading. Strain-stress-based critical plane criteria typically include a driving strain parameter and a secondary influencing stress parameter. Commonly-used examples of such models are the

Fatemi–Socie (FS) parameter[147] for shear failure mode materials and the Smith–Watson–Topper parameter[148] for tensile failure mode materials.

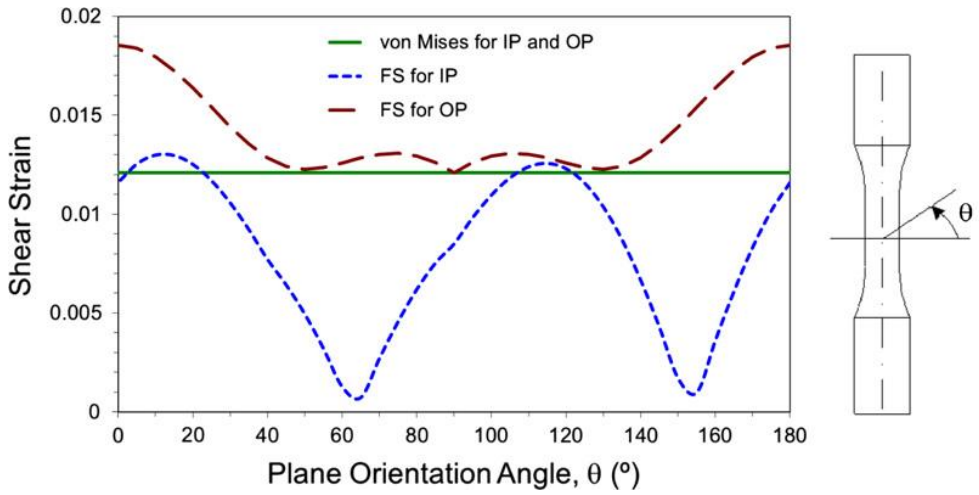

Figure 1-24. Variation of von Mises and FS damage parameters with plane orientation forτ_a=0.7% of Ti–6.5Al–3.4Mo for in-phase (IP) and 90° out-of-phase (OP) axial–torsion loadings[131]**.**

1.5 Scope of the thesis

This chapter presents the background to this research, including the concept of Surface Mechanical Attrition Treatment (SMAT), the effect of SMAT on fatigue properties of metallic materials, the basic information on the studied material 7075 Aluminum Alloy and a brief review of multiaxial fatigue. A preliminary conclusion can be drawn from the literature review that SMAT is able to improve the mechanical properties of various metallic materials, including fatigue properties in both low-cycle fatigue (LCF) and high-cycle fatigue (HCF) regimes. Nevertheless, the fatigue properties of AA7075 alloy treated by SMAT have not been revealed thoroughly, particularly in the context of complex loading conditions such as tension-torsion combined loading. Consequently, the present study aims to investigate the effect of SMAT on the fatigue properties of AA7075 in complex loading conditions. The impact of SMAT is primarily characterized through experimental investigation, encompassing the presentation of experimental data and fractographic observation. A series of specially-designed experiments is conducted in order to ascertain the impact of various factors induced

by SMAT, including surface integrity and residual stresses. The fatigue life of both untreated and SMATed AA7075 is estimated via different fatigue damage criteria.

Chapter 2 Pre-test treatment and characterization

This chapter presents the information on the pre-fatigue-test treatment and characterization of the as-received AA7075 alloy. First, the basic information on the as-received AA7075 and the dimensions of the fatigue test specimens are introduced. The non-standard heat treatment and the mechanical polishing are then presented, followed by the SMAT procedure. The results of characterization after SMAT are shown in the next section, including surface quality, hardness, residual stress and microstructure.

2.1 Basic information on AA7075 material and specimen

The material investigated in this work is a commercial precipitation hardening AA7075 subjected to a T6 heat treatment, which is commonly applied to enhance mechanical properties of this alloy through solution and artificial aging. The as-received material is in the form of an extruded bar with a diameter of 15 mm. The nominal chemical composition (in wt.%) of the material is shown in Table 2-1.

Table 2-1. Chemical composition of as-received AA7075 alloy (in wt.%)

Cr	Cu	Fe	Mg	Mn	Si	Ti	Zn	Al
0.18-0.28	1.2-2.0	0.50	2.1-2.9	0.30	0.40	0.20	5.1-6.1	Balance

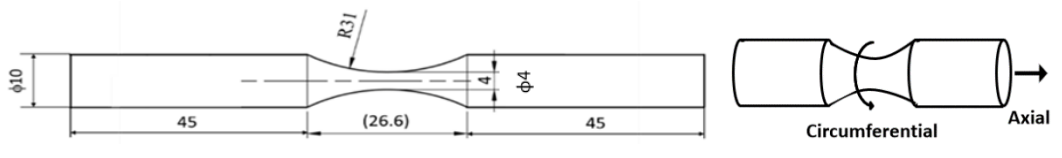

(a) **(b)**

Figure 2-1. (a) dimension of the AA7075 fatigue test specimens; (b) two typically investigated directions.

As illustrated in Figure 2-1, the AA7075 material is fabricated into dumbbell-shaped

fatigue test specimens. The two directions which will be investigated in this work are shown in Figure 2-1(b). All of the treatments, measurements and tests presented in this work are performed directly on specimens with these dimensions.

2.2 Heat treatment and mechanical polishing

The initial state of the as-received AA7075 investigated in this work is T6, which means that the strength is high while the ductility is relatively low. As indicated in the previous research [1], the T6 condition is not considered as a suitable state for SMAT. Therefore, a non-standard heat treatment is applied. The heat treatment includes a period of solution phase at 450℃ for 4 hours, followed by water quenching and an aging phase at 185℃ for 12 hours, as shown in Figure 2-2. The purpose of this treatment is to improve the ductility without reducing the strength too much. The monotonic tensile strength test is done with both the initial T6 condition and the heat-treated state (abbreviated as “HT”), as shown in Figure 2-3.

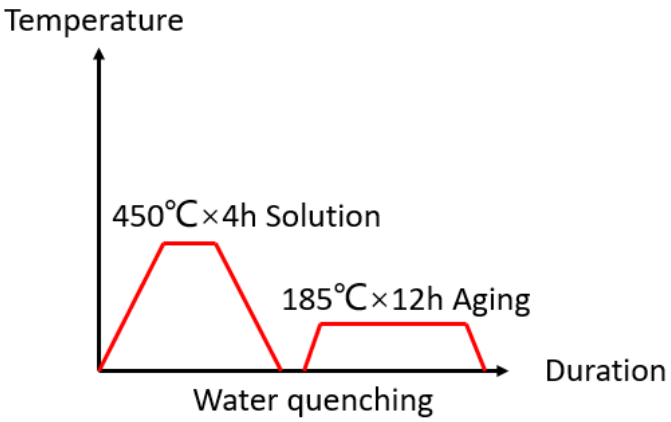

Figure 2-2. Schematic of heat treatment performed on AA7075 alloy.

The monotonic test shows that the yield stress was reduced from 600 MPa to about 400 MPa after the heat treatment, while the elongation was significantly increased. Since the kinetic energy of impacts in SMAT is high, damage could be avoided with such high ductility, as announced in [1].

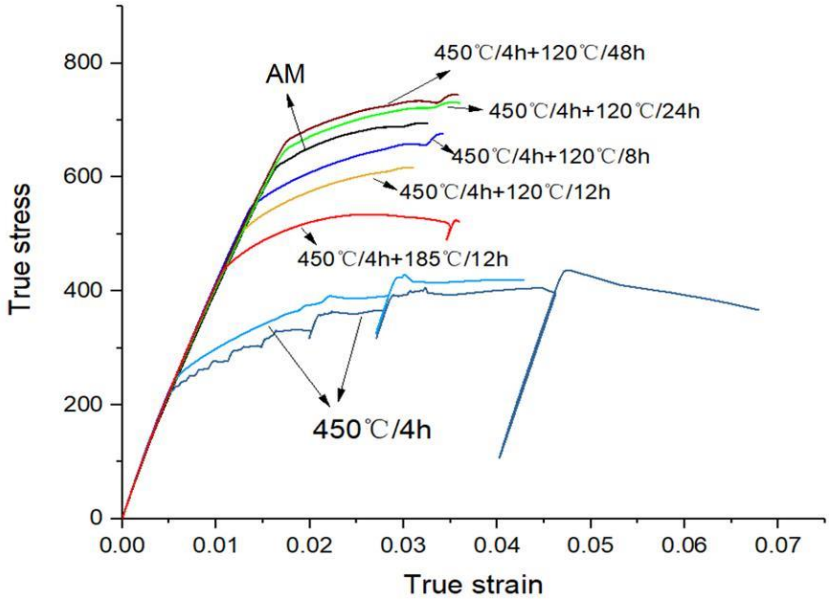

Figure 2-3. Results of monotonic tensile tests with different heat treatments [1]**.**

As shown in Figure 2-4(a), a large number of turning traces can be observed on the initial surface state of the as-received samples. Such traces could cause stress concentration and become the sources of crack nucleation when subjected to cyclic loading. Furthermore, the traces could also make it difficult to observe the crack initiation and propagation behaviors. Thus, in this work, the specimens were mechanically polished after the non-standard heat treatment. Considering the cylindrical shape of the specimens, the mechanical polishing was performed with a lathe and some abrasive papers. It can be seen that after mechanical polishing, the turning traces were replaced by polishing traces (Figure 2-4(b)). Although the mechanically-polished surface is still not mirror-like, the roughness is assumed to be significantly reduced.

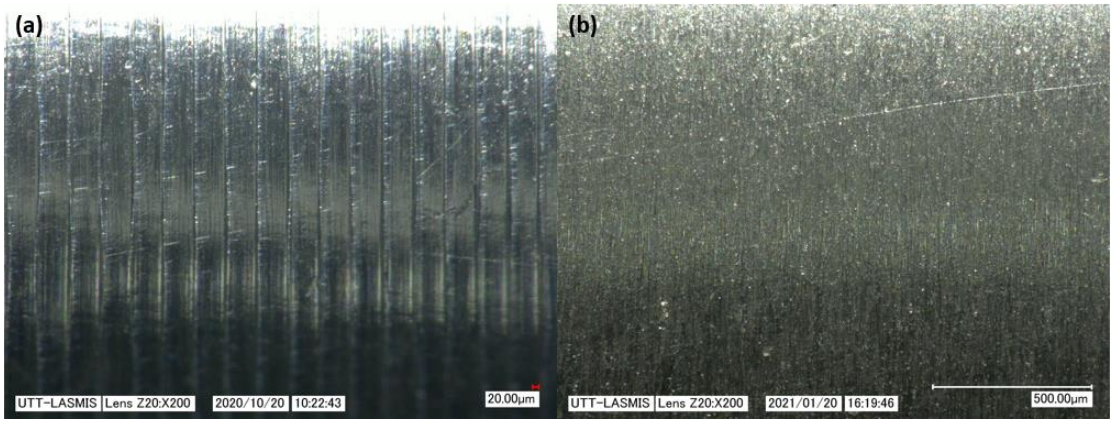

Figure 2-4. The surface of the specimen in the: (a) as-received state; (b) mechanically polished state.

2.3 SMAT procedure

In this work, SMAT was performed on AA7075 samples using a device shown in Figure 2-5(a). This device basically consists of an ultrasonic signal generator, a transformation part and a peening chamber. Considering the geometry, the specimens were placed in the middle of the chamber and were rotated at a speed of 30 rpm during SMAT, in order to treat the entire lateral surface homogenously, as shown in Figure 2-5(b).

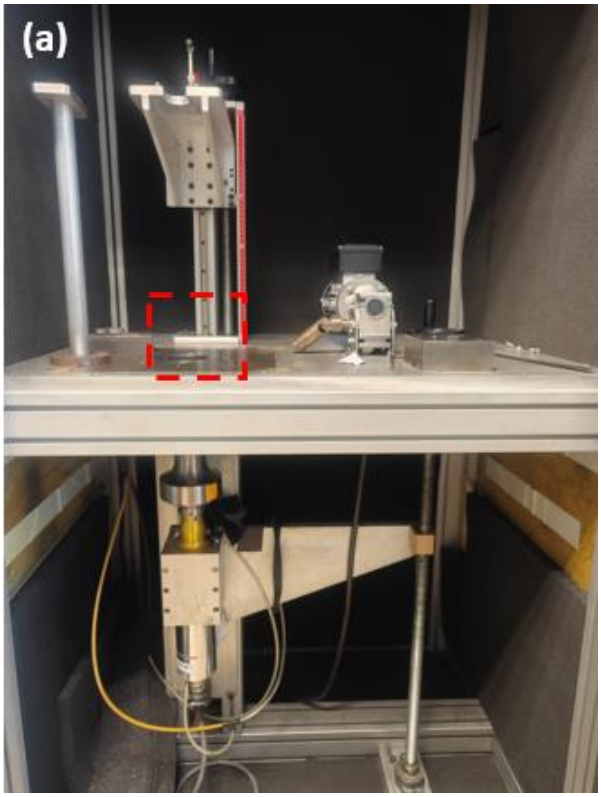

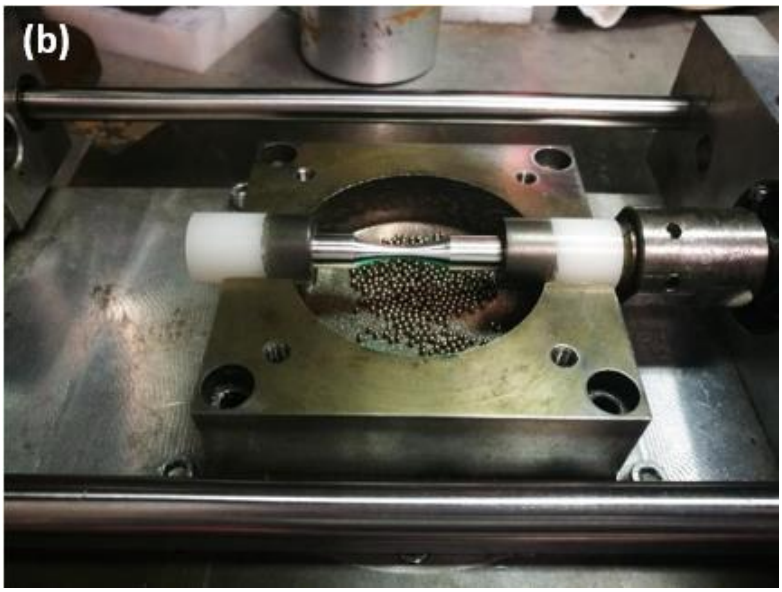

Figure 2-5. (a) The SMAT device in LASMIS UTT; (b) A specimen fixed in the SMAT chamber with spherical shot (located at the place marked in red in (a)).

As discussed in Section 1.2.3.3, the parameters of the SMAT process have been shown to be essential to the effect of SMAT, especially on the surface integrity[17,54] . In general, the size of the shot, peening intensity and peening duration are considered as the most important parameters. In the present work, the SMAT parameters were confirmed according to the previous research[1], as listed in Table 2-2. With these parameters, AA7075 specimens are confirmed to be SMATed with a coverage rate of 1000%.

Table 2-2. Parameters of SMAT

Shot size	SMAT duration	SMAT coverage	Generator power
2mm	25min	1000%	27%

2.4 Post-SMAT characterization

2.4.1 Surface quality

As illustrated in Section 1.2.3.3, the surface quality of the SMATed material is considered as an important factor contributing to the effect of SMAT on fatigue properties. Therefore, in this work, the surface quality of SMATed AA7075 specimens

was characterized, including the surface roughness and integrity.

2.4.1.1 Surface integrity

First, the SMATed surface was observed by both optical and scanning electron microscopy (SEM). Comparing Figure 2-6 with Figure 2-4(b), the surface was found to be completely modified after SMAT. Before SMAT, the mechanically polished surface was basically flat, while some traces induced by mechanical polishing can be observed. After SMAT, almost all of the traces of can no longer be observed, while a large number of dimples can be found over the entire treated area.

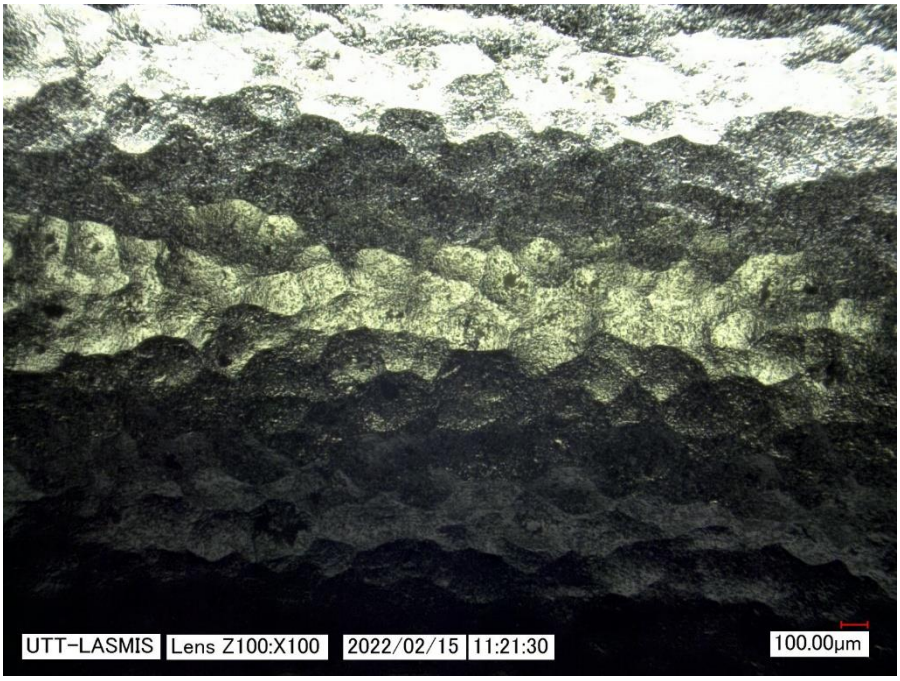

Figure 2-6. A SMATed surface observed with a KEYENCE optical microscope.

When observed at higher magnification, micro-scale defects can be found on the SMATed surface. As shown in Figure 2-7, within the observation area, several defects such as cracks are found on the SMATed surface. The dimension of these defects is about 10-15 μm, which is not easy to detect by optical microscope.

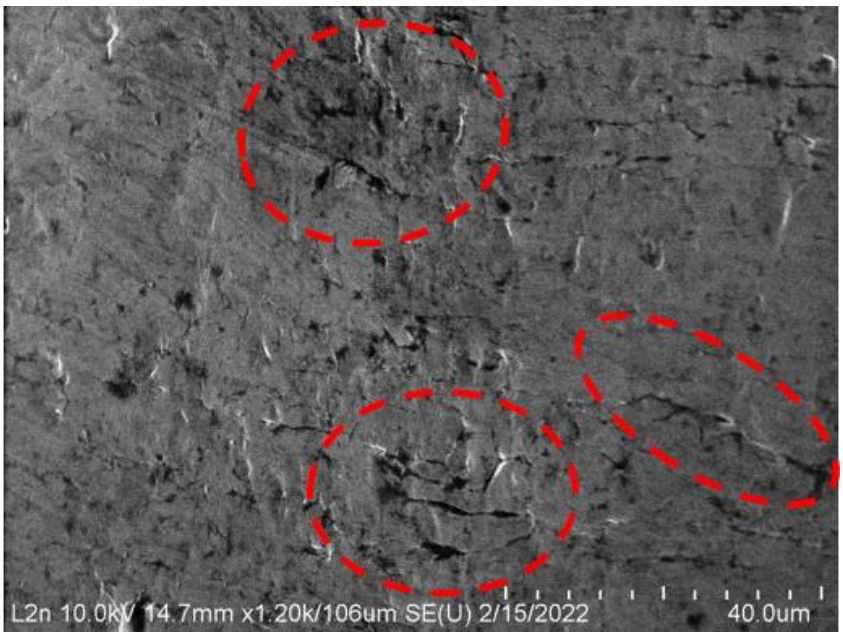

Figure 2-7. Micro-scale defects (marked in red) observed on a SMATed surface by SEM.

2.4.1.2 Surface roughness

Surface roughness was measured using a profilometer, which provides the average roughness value of a given area or a profile. The results of scanning are shown in Figure 2-8.

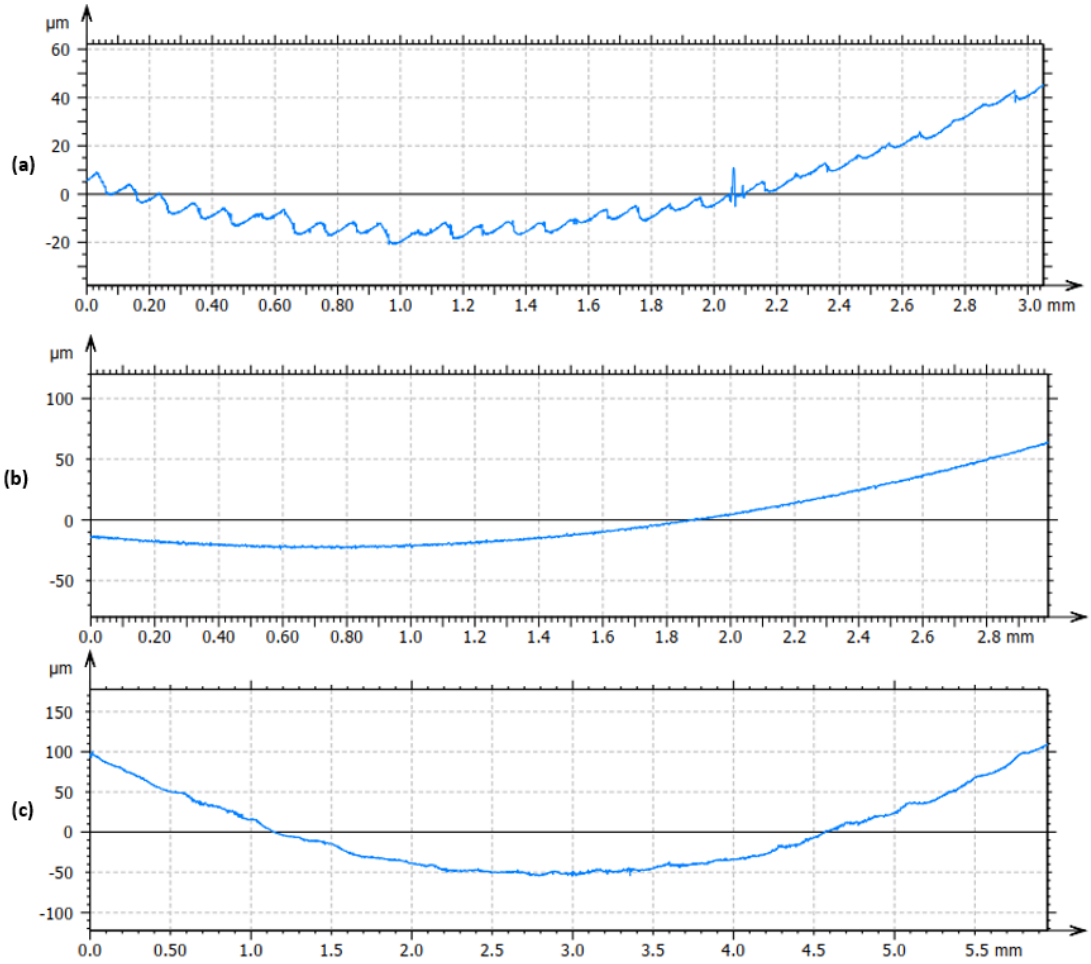

Figure 2-8. Scanning profiles of specimens in (a)AM; (b)MP; (c) SMAT states.

Table 2-3. Roughness of surfaces in different states (μ m)

Surface state	AM	MP	SMAT
Ra (μm)	0.5381	0.2812	0.4324
Rt (μm)	14.90	3.098	10.33

As illustrated in Table 2-3, the measurement result of a profile shows that the surface of the as-received specimens has the highest roughness. Compared to the as-received state, the mechanically polished state has a much lower roughness, while the SMAT state has an intermediate roughness.

2.4.2 Residual stresses

The residual stress and work hardening are important factors contributing to the mechanical properties after SMAT, especially the fatigue properties. Thus, X-ray diffraction method is used to measure the residual stresses. The X-ray diffraction is

performed using a SEIFERT XRD machine with a Cr $K\alpha_{1+2}$ X-ray tube.

SMAT is pronounced capable of generating a residual stress layer, and the profile of residual stress distribution is measured in this work with the help of electropolishing method. By controlling the polishing time, the AA7075 specimens with both as-received and SMAT states are polished and measured layer by layer. The interrupted polishing is performed with an electropolishing device in LASMIS UTT, which is explained in detail in Chapter 4. After each polishing step, the diameter of the central part of the specimen (where the polishing is performed) is measured with a 3D measuring machine MMT in LASMIS UTT. The SEIFERT XRD machine and the MMT 3D measuring machine are shown in Figure 2-9.

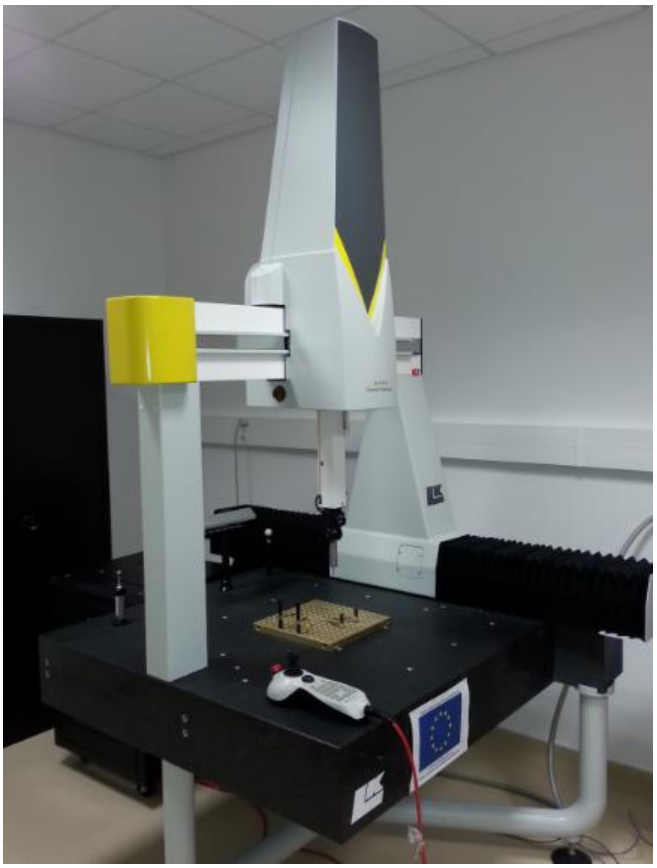

(a)

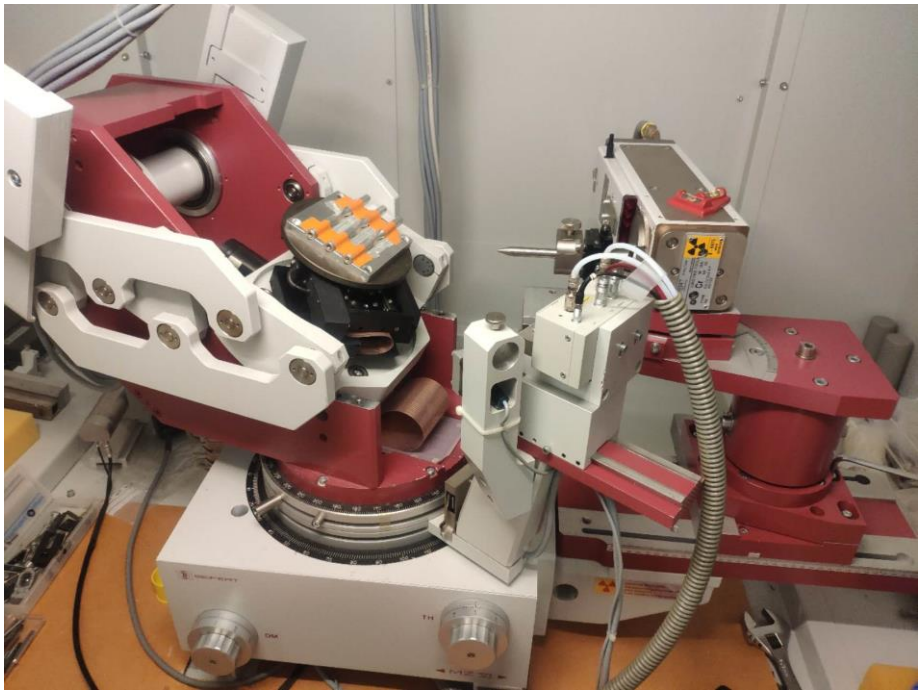

(b)

Figure 2-9. (a) MMT 3D measuring machine; (b) specimens fixed on the SEIFERT XRD machine in LASMIS UTT.

Material removal causes a redistribution of residual stresses which, depending on the geometrical parameters of the specimen, can greatly modify the initially introduced stress. The analytical method used to account for this redistribution is thus presented here.

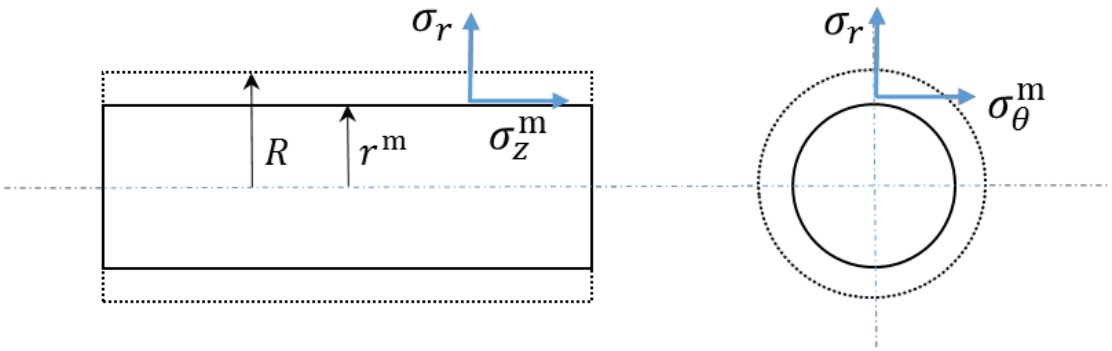

Figure 2-10. Schematic of the material removal.

In the case of a cylindrical sample, a series of axial and circumferential stresses (denoted as $\sigma z\mathrm{m}$ and $\sigma\theta\mathrm{m}$) can be measured through a gradual removal of the material layer, as depicted in Figure 2-10. When electrolytic polishing is used to remove

material from the periphery of the sample, the sample transitions to a new state of self-equilibrium. This transition causes a shift in the residual stress field, the magnitude of which varies with the thickness of the removed layer. Consequently, the stress measurements obtained via X-ray diffraction (XRD) capture the state of equilibrium after this adjustment, rather than the initial residual stresses introduced by processes like Surface Mechanical Attrition Treatment (SMAT). Moreover, radial residual stress assessment is challenging due to stress release during the iterative removal of outer material layers.

Based on the self-equilibrium and stress coupling relationship in a cylindrical coordinate system, the true residual stresses (σrt, $\sigma\theta$t, σzt) can be obtained by correcting the measured stresses ($\sigma\theta$m, σzm) using the following equations:

$$\sigma_r(r^m) = -\int_{r^m}^{R} \sigma_\theta^m(r)\frac{dr}{r}$$

$$\sigma_\theta^t(r^m) = \sigma_\theta^m(r^m) + \sigma_r(r^m)$$

$$\sigma_z^t(r^m) = \sigma_z^m(r^m) - 2\int_{r^m}^{R} \sigma_z^m(r)\frac{dr}{r}$$

Figure 2-11 shows the measured and corrected profiles of a SMATed specimen. It can be seen that the difference between the corrected and the measured profile is not negligible, especially for the residual stress in the axial direction. This analytical correction is applied to all the measurements made in the present work.

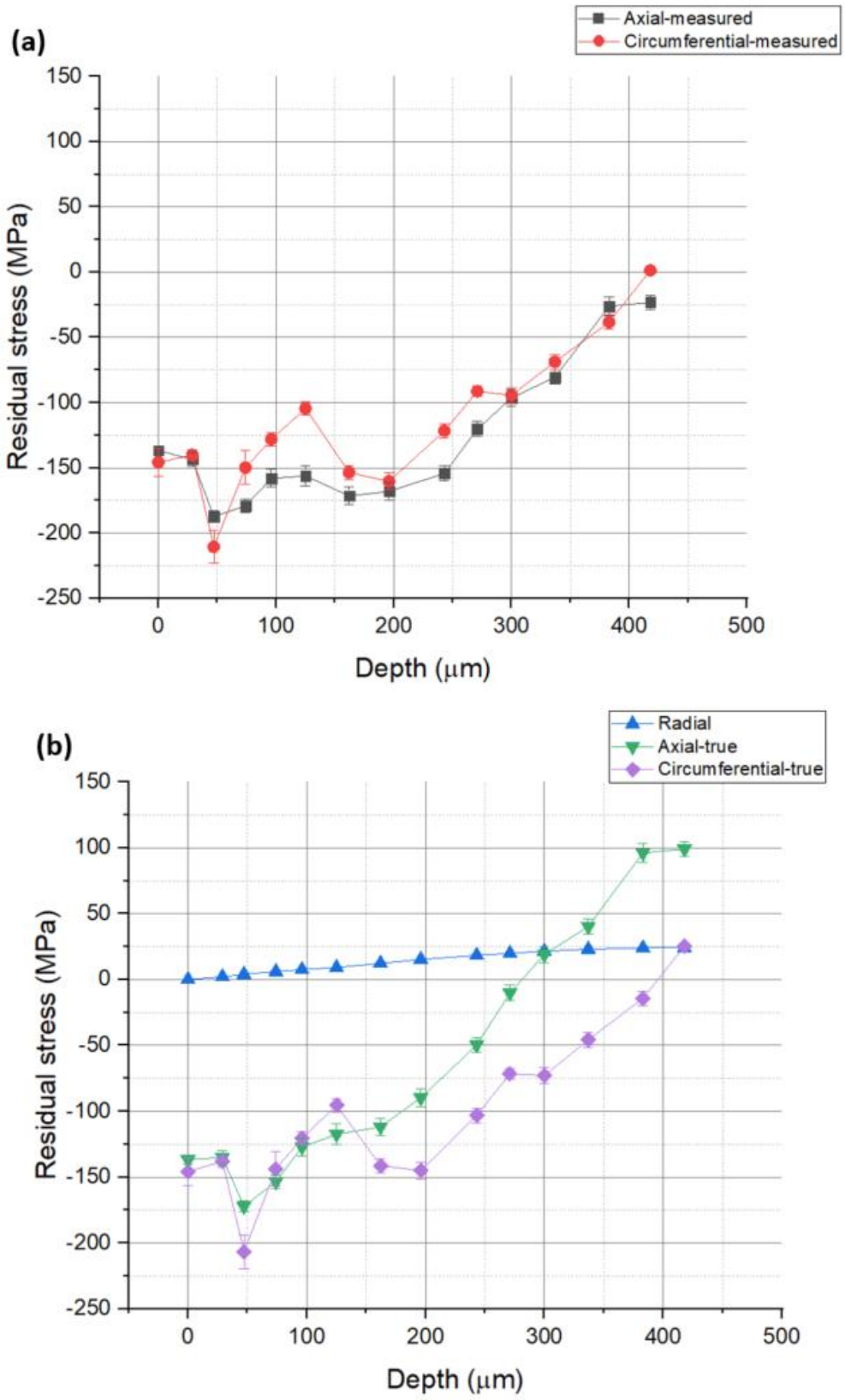

Figure 2-11. Residual stress profiles of a SMATed specimen (a) before and (b) after correction.

Figure 2-12 presents the residual stress distribution of specimens with both MP and

SMAT states after correction. It can be seen that both the mechanically polished and SMATed specimens have a residual stress gradient distribution. The SMATed specimen exhibits a SMAT-affected layer of approximately 400 μm. The SMAT-induced residual stresses occur in both the axial and circumferential directions, and the stresses in these two directions have almost the same trend along the radial direction. The SMAT-induced residual stresses at the top surface are measured to be around -150 MPa. As the distance from the surface increases, the value of compressive residual stress first increases to a peak value of -210MPa and then decreases until the distance reaches 400μm. The specimen with MP state shows a residual stress of about -50MPa on its surface as a result of mechanical polishing process. However the effect of MP is not significant since the depth of the MP-affected layer is measured to be less than 50μm, which is much smaller than that of the SMAT-affected layer.

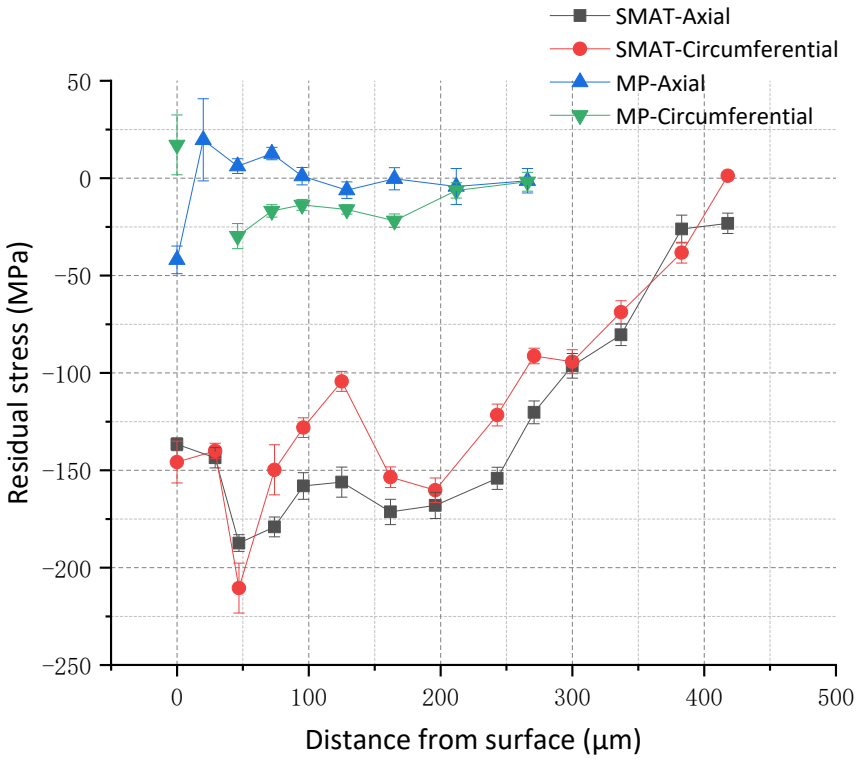

Figure 2-12. Residual stress profile of MP and SMAT specimens.

2.4.3 Hardness and tensile strength

According to the research mentioned in Chapter 1, the increase in hardness is

another significant modification induced by SMAT. The hardness measurement of AA7075 alloy both before and after SMAT is performed in the lab of UTT. And the results are shown in Figure 2-13.

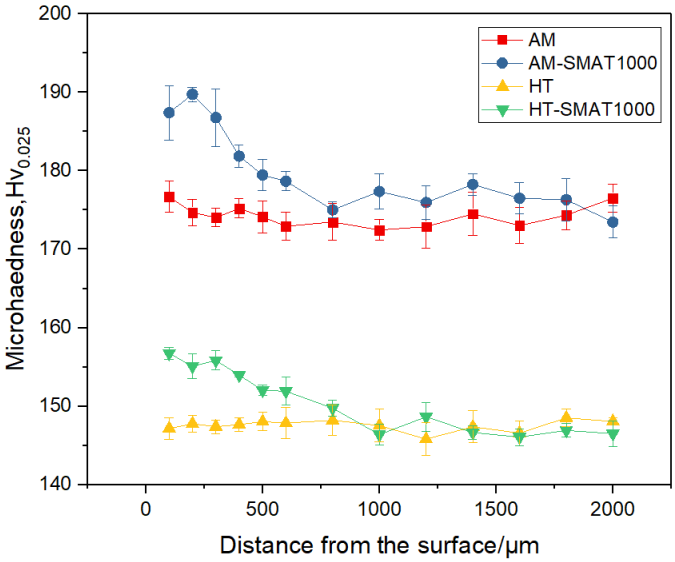

Figure 2-13. Hardness profile measured on AA7075 alloy in as-received (labelled "HT") and SMAT (labelled "HT-SMAT 1000") states [130]**.**

It can be seen from Figure 2-13 that the surface hardness of the AA7075 specimens is increased from 147$HV_{0.025}$ to 157$HV_{0.025}$ after SMAT. The value of hardness decreases as the distance from the top surface increases. The value of hardness after SMAT becomes the same as that of the as-received state at the depth of approximately 600 μm, which is considered to be the border of the gradient structure.

The tensile strength of AA7075 is also studied by performing monotonic tensile tests with the testing machine in UTT. As shown in Figure 2-14, the tensile strength of AA7075 is increased after SMAT (the green curve), although the increase rate is not significant when compared with the effect of heat treatment.

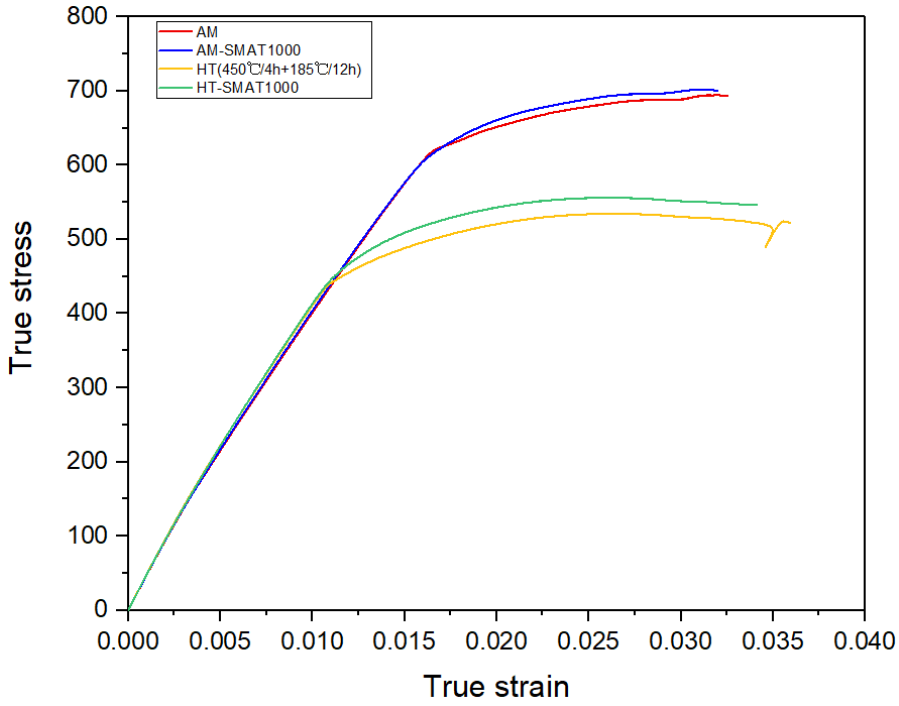

Figure 2-14. Tensile test curves of AA7075 in as-received (labelled "HT") and SMAT (labelled "HT-SMAT 1000") states [1]**.**

2.4 Conclusion

In this chapter, first, basic information is given on the material investigated in the present work, as well as the parameters of SMAT procedure. Second, the characterization of the effects of SMAT is presented, including the surface roughness, surface integrity, residual stresses, hardness and tensile strength. Through various measurements, SMAT is found to be able to significantly increase the tensile strength and surface hardness. A compressive residual stress layer can also be generated on the AA7075 specimens, which has a thickness of approximately 350μm and a peak value of -200MPa. However, the surface roughness of AA7075 specimens is found to be dramatically increased after SMAT. Defects such as micro-scale cracks are observed on the SMATed surface.

Chapter 3 Fatigue properties of SMATed AA7075 under biaxial loadings

In this chapter, the biaxial fatigue tests and results are presented. The experimental procedure is first introduced, including the testing device and the information on the cyclic loadings. Secondly, the obtained S-N data are presented with some basic statistical analyses. Fracture analysis based on fractography is also discussed and summarized for understanding the fracture mechanism of the failed specimens under different conditions.

3.1 Fatigue test procedure

3.1.1 Fatigue test device

In the present work, all the fatigue tests were performed with an electropuls fatigue machine (Instron). As shown in Figure 3-1, cylindrical specimens were fixed with grippers so that both uniaxial and torsional loads can be applied.



Figure 3-1. Fatigue testing machine Instron ElectroPuls E10000 with a specimen fixed on it

3.1.2 Biaxial cyclic loadings

The fatigue tests are performed with a loading path in which the axial and torsional loadings are proportionally applied in the form of a sinusoidal wave, as shown in Figure 3-2. The ratio between the shear stress and the normal stress is chosen as equal to $1/\sqrt{3}$, which is commonly investigated in the literature[131]. The frequency of the test is set as 5Hz, according to the limit of the testing equipment. The tests are performed at room temperature.

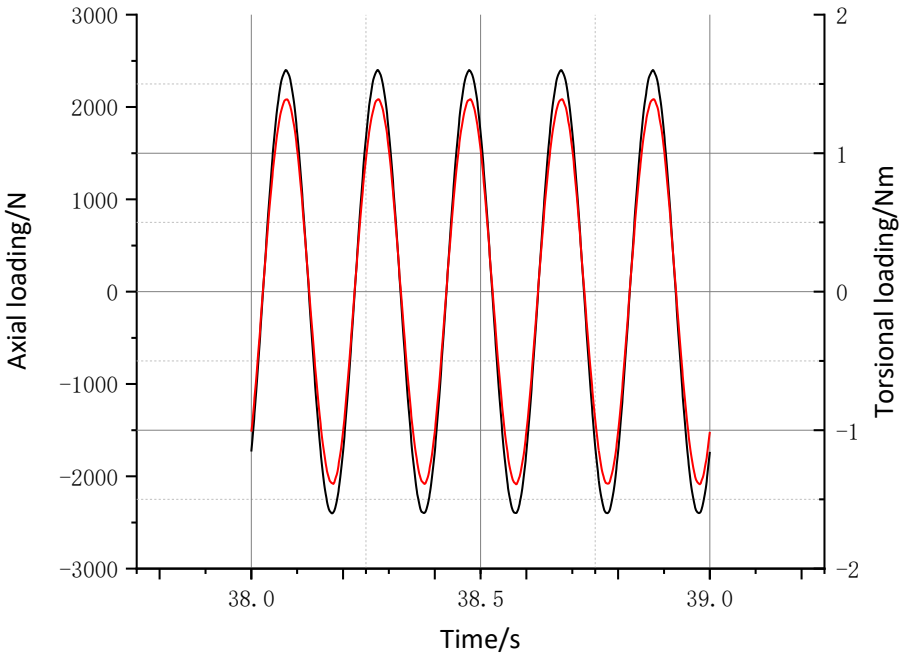

Figure 3-2. Input signal of axial and torsional loadings.

3.2 S-N data of biaxial fatigue tests

For biaxial fatigue tests conducted in the present work, the main data to be recorded is the fatigue life, i.e. the number of cycles loaded until the fracture of the specimen. The data of both MP and SMAT specimens are plotted and analyzed in the formality of equivalent stress amplitude versus total fatigue life (S-N).

3.2.1 Mechanically-polished state

As shown in Figure 3-3, the S-N plot of the experimental data of MP specimens gives

the basic information on fatigue strength. As illustrated in this figure, most of the MP specimens tested in the present work exhibit a fatigue life within a range of $10^{\wedge 4}$ to $10^{\wedge 6}$ cycles, which is commonly recognized as high-cycle fatigue regime. For relatively high stress amplitudes, such as equivalent stress amplitudes of 280 MPa and 300 MPa, the fatigue lives are less than $10^{\wedge 5}$ cycles. Specimens tested at intermediate load levels show fatigue lives between $10^{\wedge 5}$ and $10^{\wedge 6}$ cycles. While for specimens tested at a lower load level such as 220 MPa, the fatigue life is found over $4\times10^{\wedge 6}$ cycles.

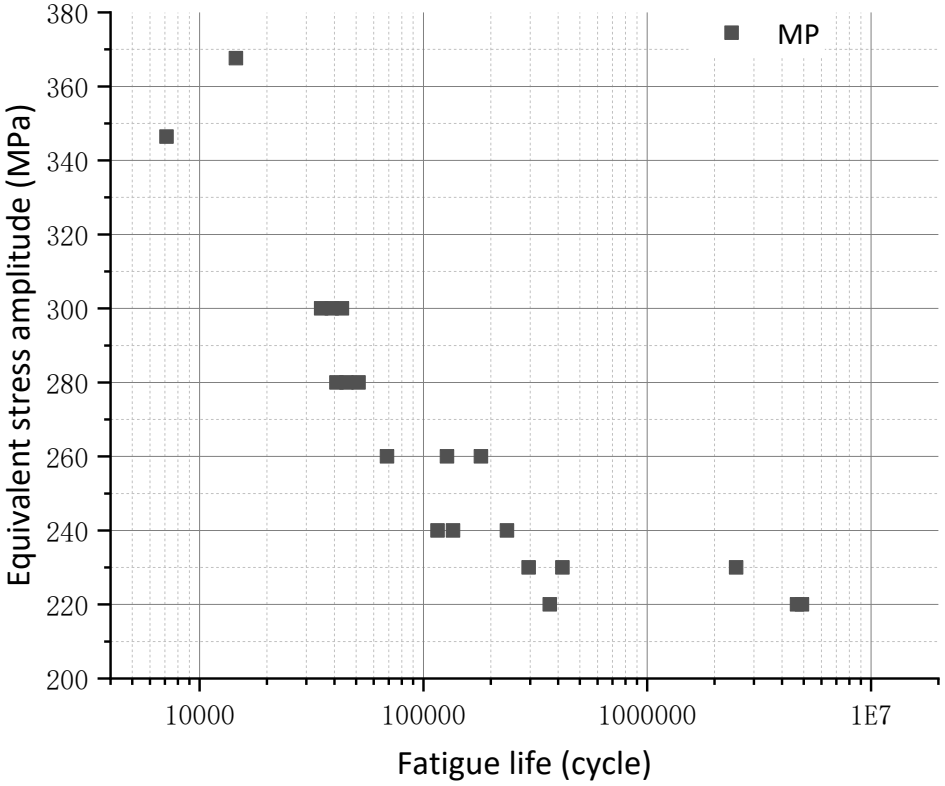

Figure 3-3. S-N plot of biaxial fatigue tests for specimens in MP state.

3.3.2 SMATed state

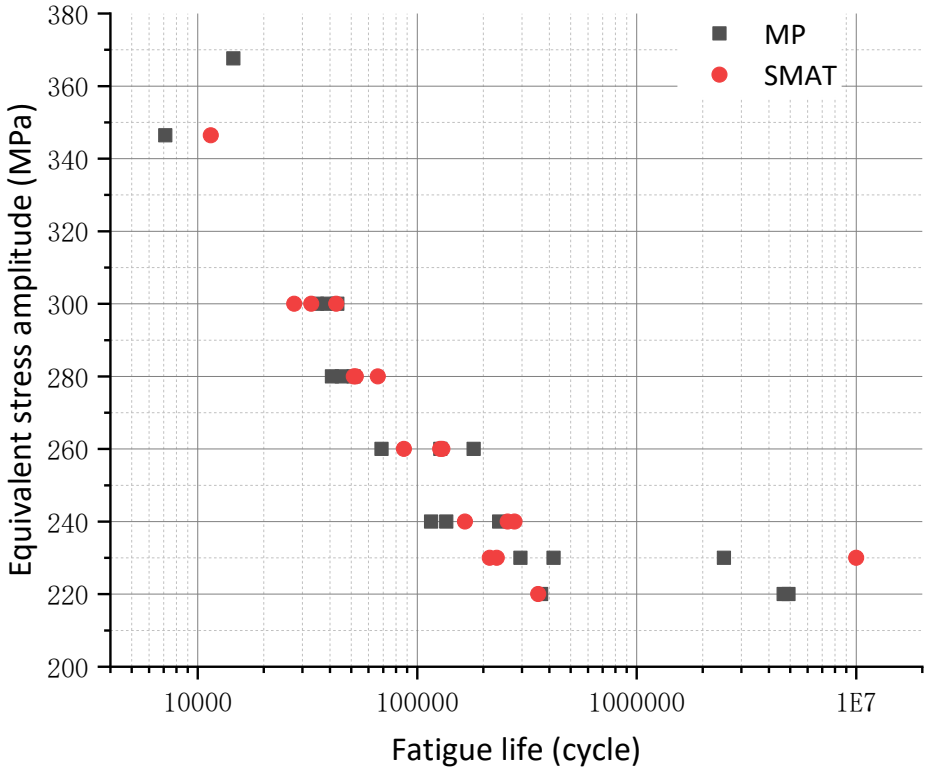

Figure 3-4. S-N plots of fatigue tests for specimens in MP and SMAT states.

The S-N plot of SMAT state is presented in comparison with MP state in Figure 3-4. As illustrated by these plots, the fatigue life of SMAT state exhibits no significant difference compared with MP state, for all the stress amplitudes applied. The relation between S and logN seems to be linear from 300 MPa until 220 MPa, except for one specimen tested with an equivalent stress amplitude of 230 MPa. The little difference in fatigue life data is considered interesting since the research in the literature has reported considerable enhancement of fatigue strength thanks to SMAT when testing with both uniaxial and torsional loading conditions.

3.3 Statistical analysis of S-N data

3.3.1 Basquin equation

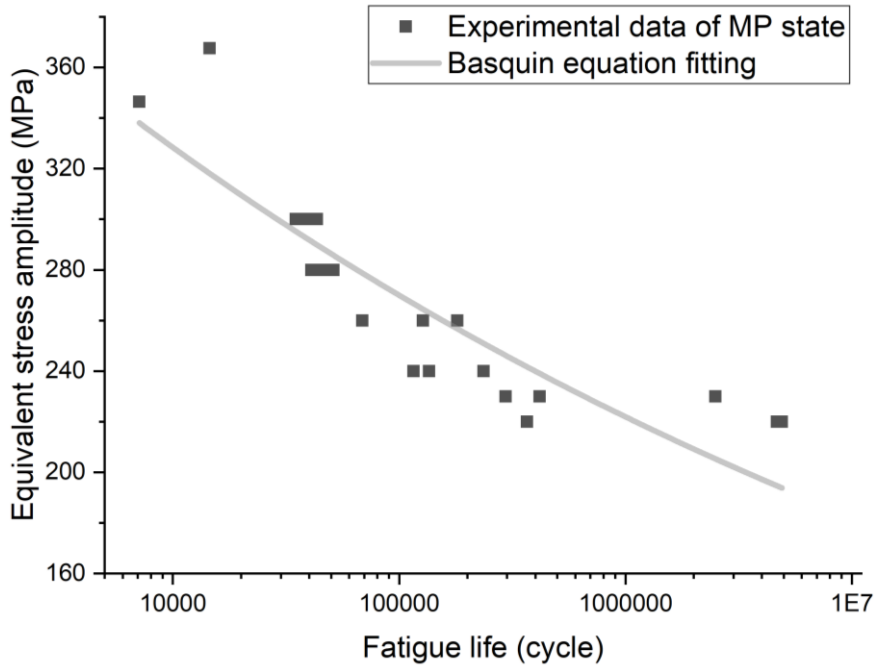

(a)

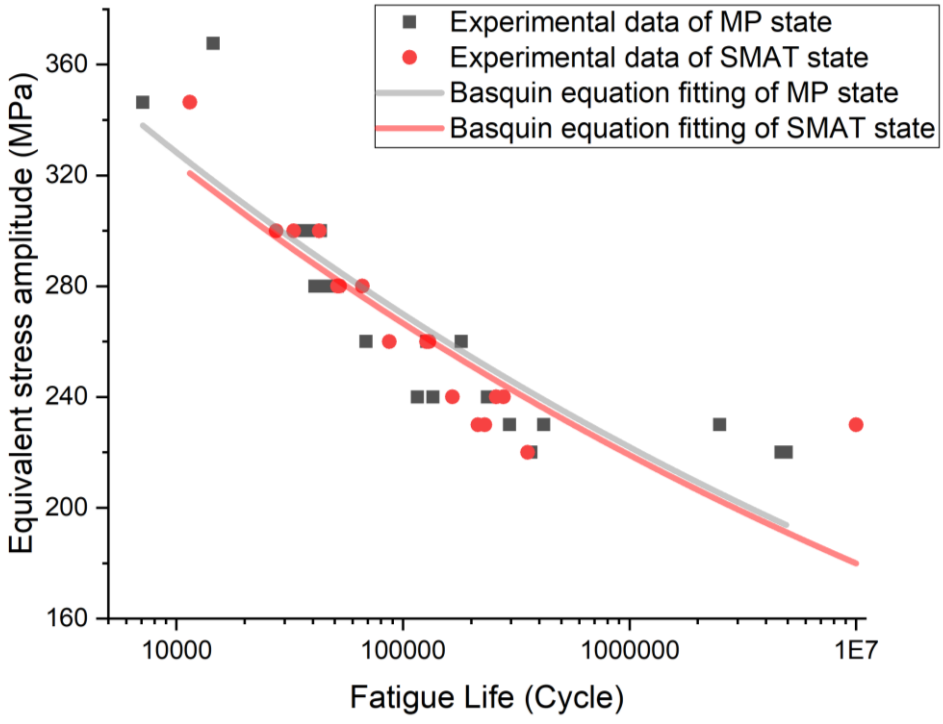

(b)

Figure 3-5. Basquin equation fitting of (a) MP state; (b) MP and SMAT states.

The Basquin equation is commonly used to fit the S-N data. Hence, in this section, the fitting is performed for both MP and SMAT states. The Basquin equation can be expressed as:

$$S = a \cdot (2N)^b$$

Where S is the stress amplitudes, N is the fatigue life, a and b are fitting parameters. According to the fitted curve shown in Figure 3-5(a), the Basquin equation fits the data points well, except for the tests at extremely high or low stress levels. The fitted curves of MP and SMAT states are quite close to each other. The similarity in the slope of the curves indicates little difference in fatigue strength between MP and SMAT states.

The parameters of Basquin equation of MP and SMAT states are listed in Table 3-1.

Table 3-1. Basquin equation parameters of MP and SMAT states.

	a	b
MP	762.717	-0.0850953
SMAT	756.004	-0.0853823

The similarity in the values of a and b helps to confirm that the fatigue strength of specimens in MP and SMAT state is almost the same under biaxial fatigue loading condition.

3.3.2 P-S-N analysis

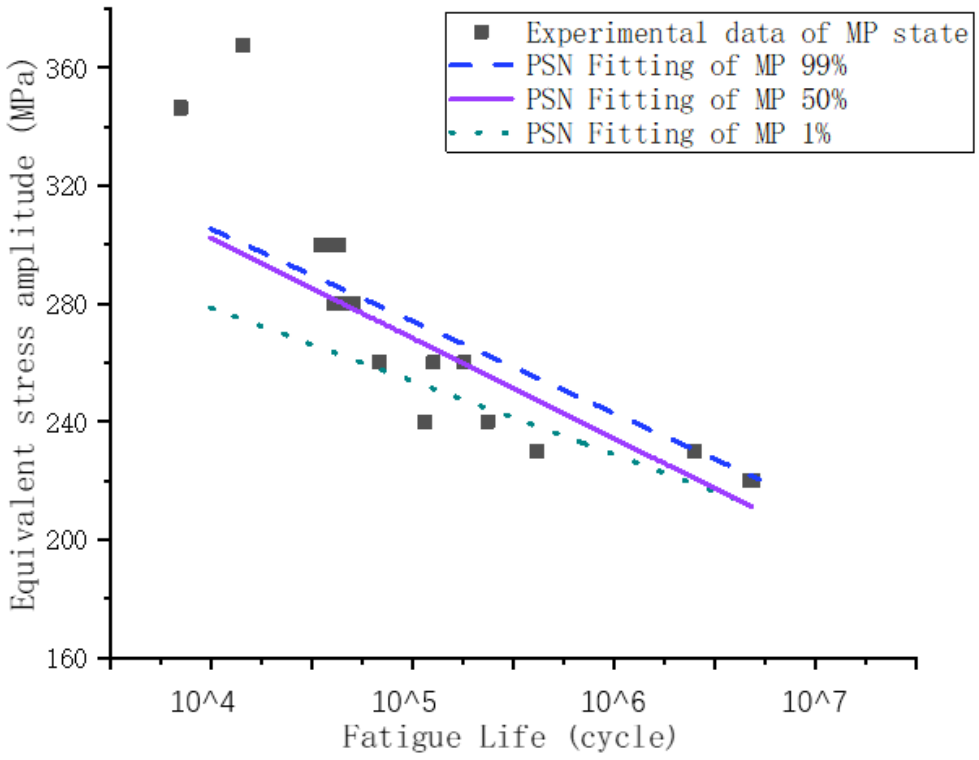

(a)

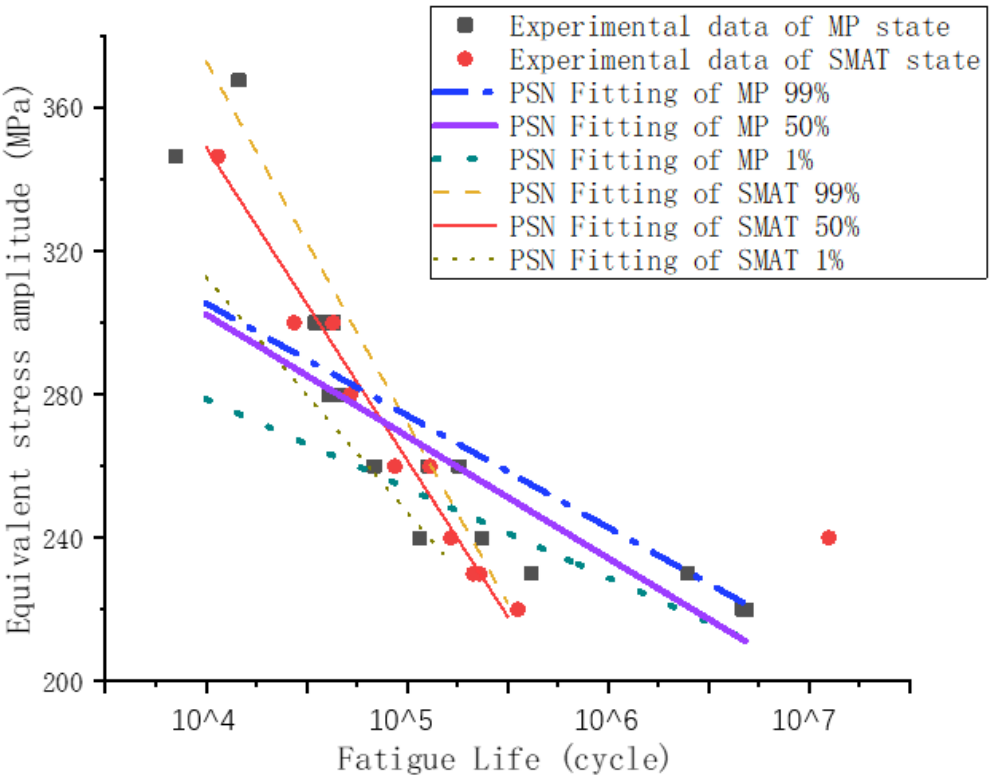

(b)

Figure 3-6. P-S-N fitting of (a)MP state; (b)MP and SMAT states.

P-S-N fitting is a commonly used method for quantitative analysis of the S-N data. S-N data obtained from experiments with different loading levels are fitted to a Weibull distribution by maximum likelihood estimation:

$$P = 1 - exp\left[-\left(\frac{N}{N_a}\right)^b\right]$$

Where b and N_a are the shape and scale parameters of the Weibull distribution.

The fitted Weibull parameters of MP state specimens are partly listed in Table 3-2. Similarly, experimental data of SMAT is also fitted into Weibull distribution. Based on the fitted Weibull distribution, the P-S-N curves with fracture possibility of 1%, 50% and 99% are plotted with least square method, as shown in Figure 3-6. According to Figure 3-6, it is also clear to see that the fatigue strength is reduced after SMAT when testing at low stress amplitudes like 230MPa or 220MPa.

Table 3-2. Weibull distribution fitting parameters for several MP state specimens

Stress amplitude (MPa)	Shape parameter b	Scale parameter N_a
300	138.526	4.609
280	128.919	4.679
260	36.511	5.148

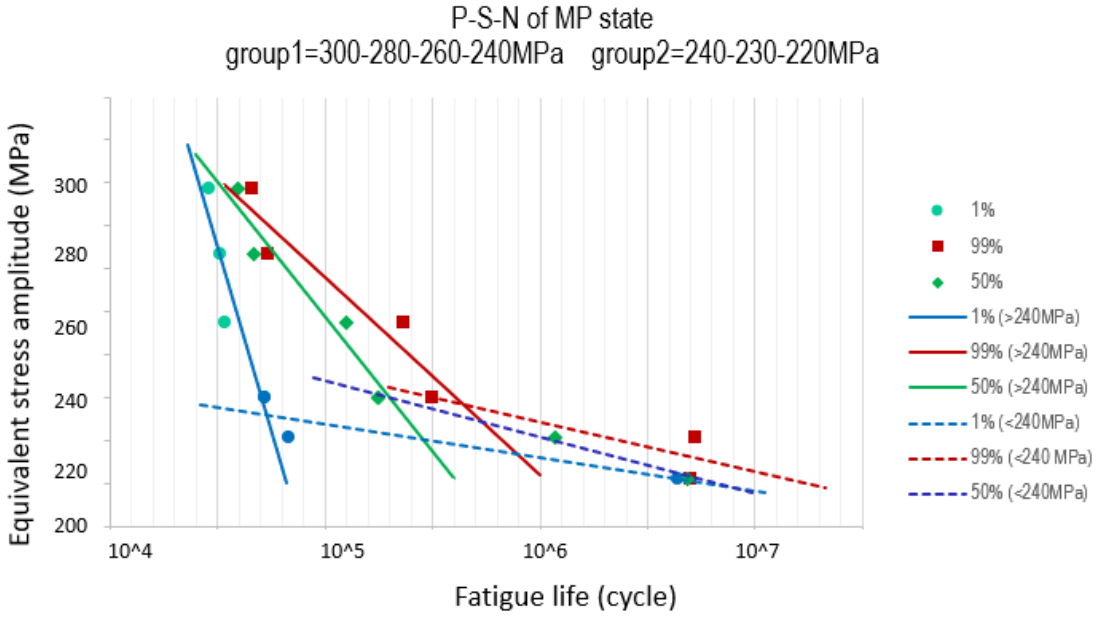

Figure 3-7. 2-part fitted P-S-N curves of MP state.

It can also be noted that the P-S-N curves of MP state can be fitted by 2 parts: 260-300MPa and 220-240MPa. The 2-part fitting makes the P-S-N curve much more reasonable since the experimental data points are mostly on the left side of the 99% possibility curve. Such phenomenon is consistent with the observation in S-N plot.

3.4 Fractography observation

The analysis focuses on the fractography of the tested specimens. The fractured specimens are first observed using a digital optical microscope, which provides basic information about the failure. SEM observations are also performed for more detailed characterization at higher magnification. Information on the fracture mechanism is therefore gathered from the fractographic observations.

3.4.1 MP state

As presented in Figure 3-8, the MP specimen tested at a high stress amplitude (equivalent value of 368MPa) exhibits an extremely rough morphology. Such a “factory roof” phenomenon is likely to be related to multiple initiation sites and the difference in crack propagating rate between mode Ⅰ and mode Ⅱ/Ⅲ. As shown in the zoom-in figure (Figure 3-8.b), several sites can be observed with macro-scale deformation and can be assumed as the crack initiation sites. According to research in literature, the crack propagation can be roughly divided into 2 stages: stage Ⅰ and stage Ⅱ. During the Stage Ⅰ, cracks propagate on the plane of maximum shear, including mode Ⅱ and mode Ⅲ crack growth. During the Stage Ⅱ, cracks propagate on the plane of maximum principal stress by a mode Ⅰ crack growth mechanism. Among these sites observed in the present cases, almost all exhibit similar stage Ⅰ propagation while only one becomes the main crack and leads to the final fracture. This main crack, marked by the red arrow in Figure 3-9, is found initiating at the surface of the material. If observed from the lateral surface in the perpendicular direction to the specimen axis, the main

crack initiation area and its vicinity can be divided into 3 parts: the shear-crack initiation area, the shear-propagation area, and the tensile-propagation area, the latter 2 corresponding to the stage Ⅰ and stage Ⅱ of propagation. As illustrated by the red arrow in Figure 3-9, the initiation of the main crack appears to be at an angle of approximately 70° to the specimen axis, which is actually close to the plane of maximum shear stress for the applied combined tension-torsion loading. The cracking angle indicates the high possibility of a shear-cracking phenomenon in this case. The area marked with the orange dotted line is the stage Ⅰ propagation area, where the propagation of the crack is mainly driven by the maximum shear stress. Thus, the angle of the crack path does not change much compared to the initiation location. While the area marked with the blue dotted line is the stage Ⅱ propagation area, where the driving force of the propagation changes to the principal opening stress. Hence, the angle of the crack path changes significantly when compared to that in stage Ⅰ.

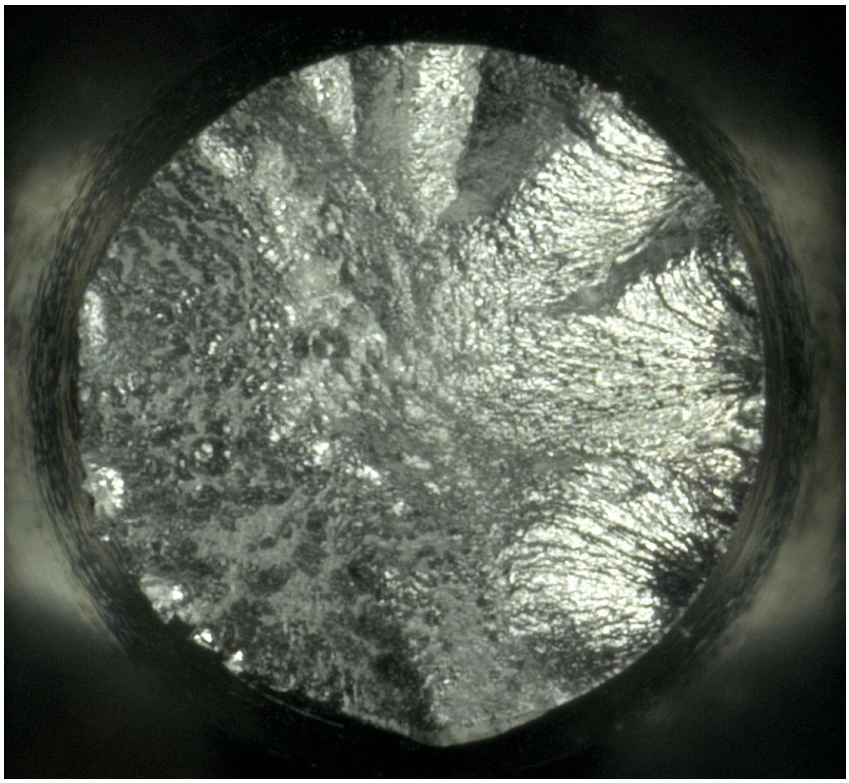

(a)

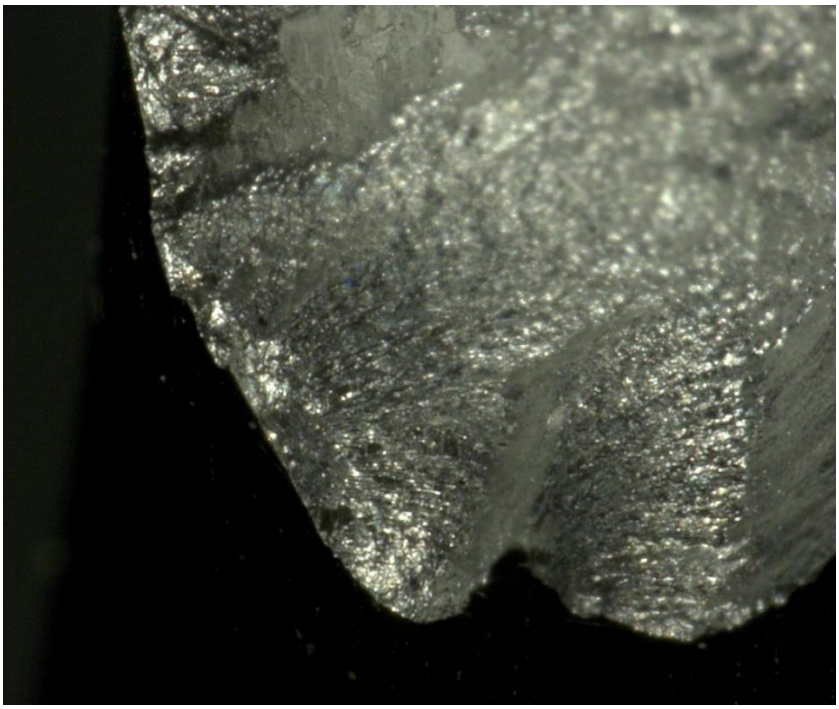

(b)

Figure 3-8. (a) fracture surface of an MP state specimen tested at a high stress amplitude (368MPa); (b) a zoom-in figure of the multiple initiation sites.

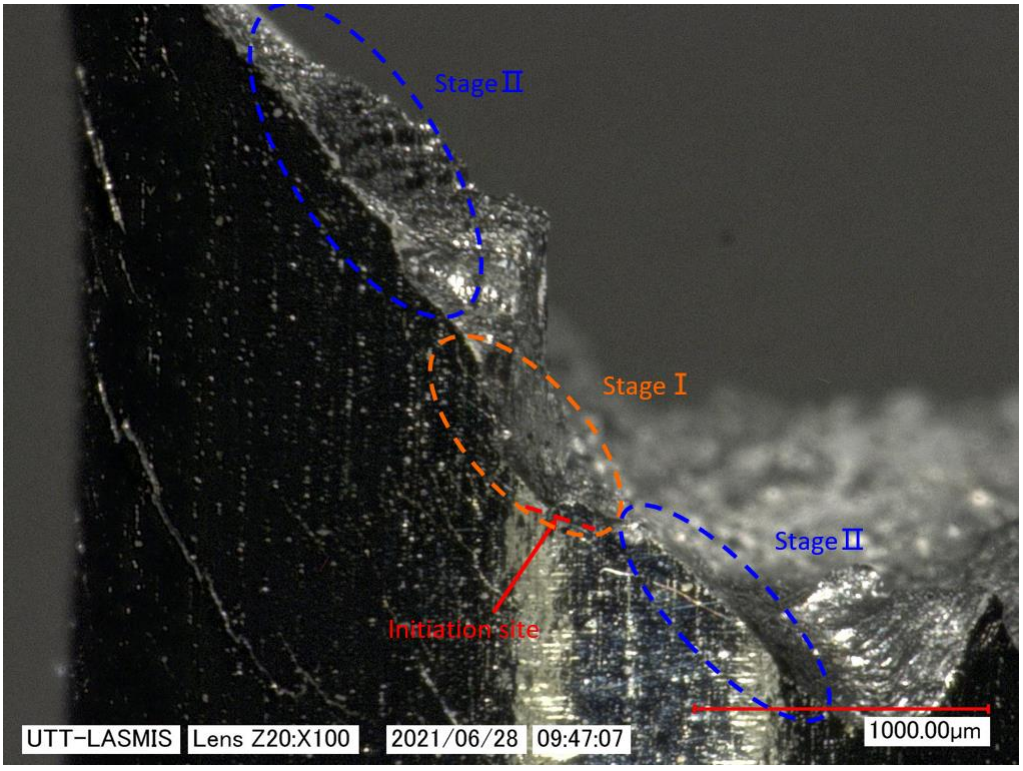

(a)

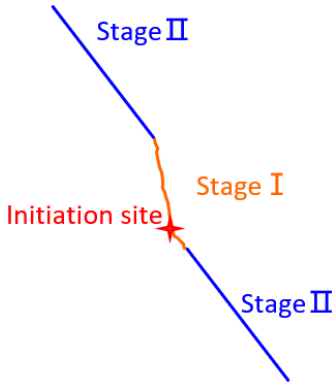

(b)

Figure 3-9. Different crack propagation stages in the case of high stress amplitude: (a) microscope image; (b) schematic.

For intermediate stress amplitudes, the fractography shows obvious difference compared with the case of high stress amplitudes. As shown in Figure 3-10, the fracture surface of a specimen tested at 280MPa is taken as a typical example. The first thing to be noticed is that only a single initiation site can be found on the superficial area instead of multiple sites. Secondly, if observed from the axial direction, the fracture surface can be easily divided into 2 parts. As illustrated in Figure 3-10, the area marked with the red dot line is considered to be the stage Ⅰ area, which is an oblique and relatively flat plane. The rest of the fracture surface is much rougher and consists of the stage Ⅱ area and the final fracture area. Unlike the high stress amplitude case, the proportion of the stage Ⅰ area significantly increases.

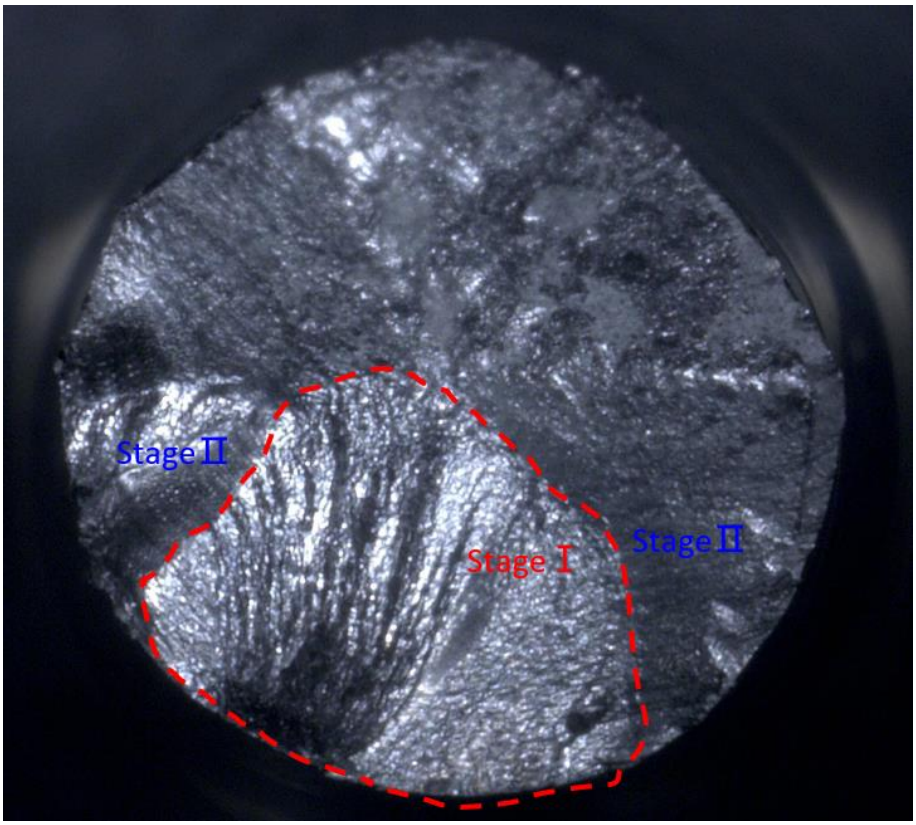

Figure 3-10. Fracture surface of a MP specimen tested at 280MPa

According to the observation, the crack is located on the upper surface, but the angle of initiation is not exactly the same as the angle of the stage Ⅰ area. As shown in Figure 3-11(a), the initiation can be seen as a combination of 2 cracks, one with the same angle as stage Ⅰ and the other with an angle of approximately 64° (close to stage Ⅱ). This is confirmed by the SEM magnified image in Figure 3-11(b). Some extrusion can be seen at the initiation site, indicating that the crack initiates in a one direction and then propagates in another direction at the early stage Ⅰ. Mixed-cracking, driven by both shear stress and principal stress may be the explanation for this phenomenon.

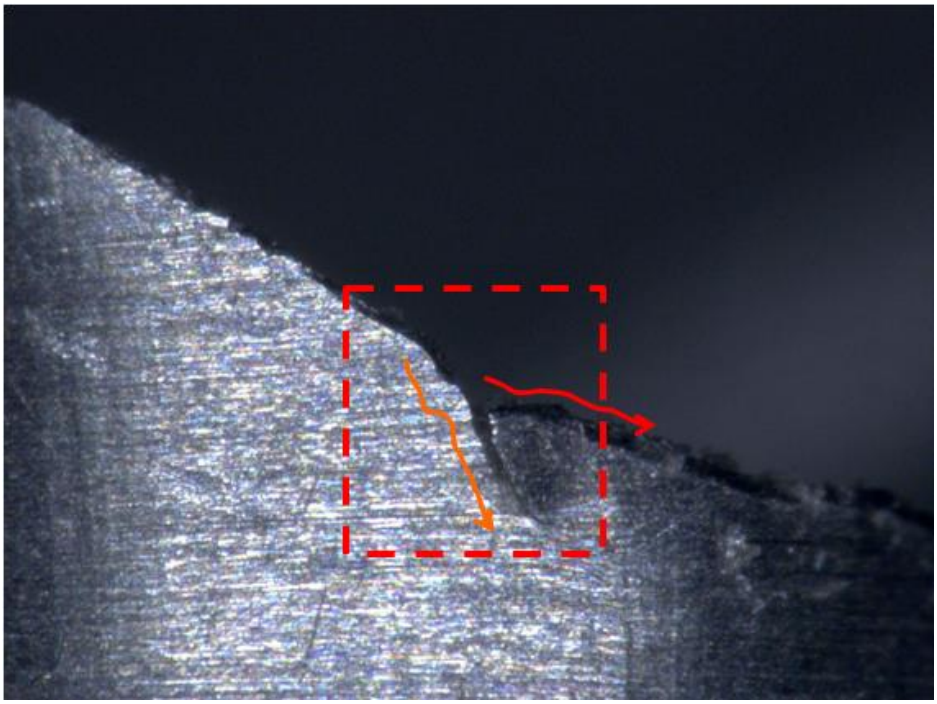

(a)

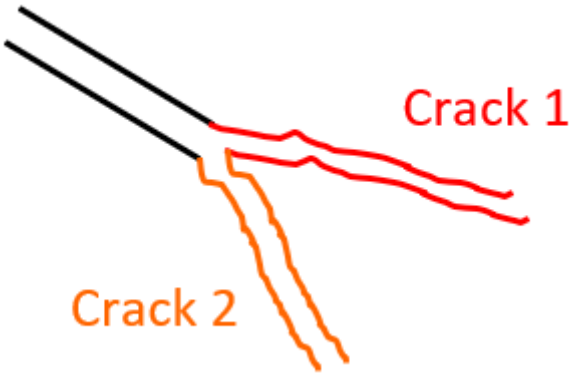

(b)

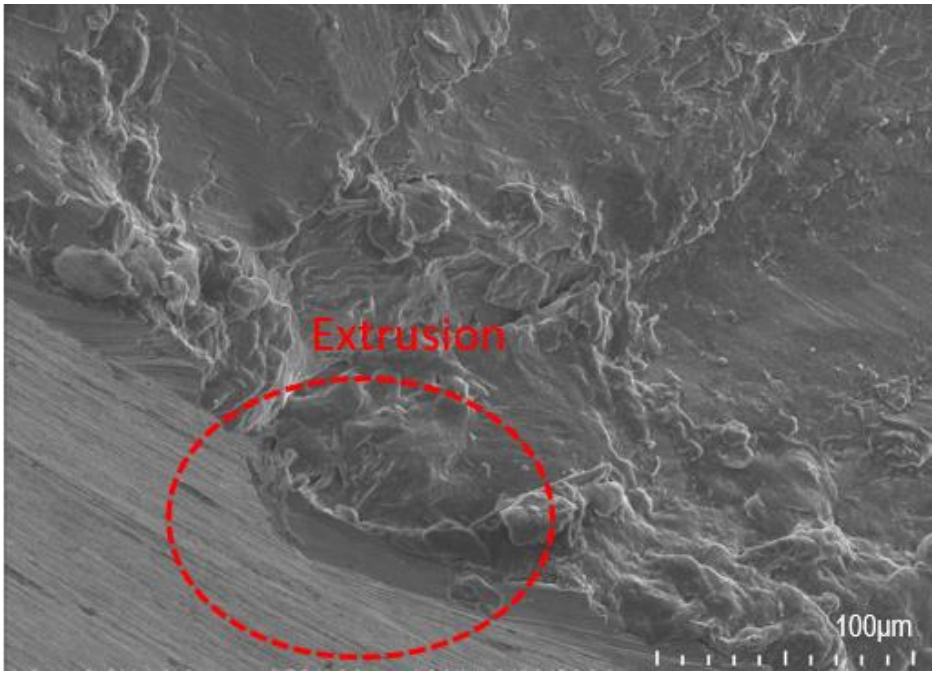

(c)

Figure 3-11. (a)(b) Observation of crack initiation on the lateral surface (tested at 280MPa); (c) a close-up of the crack initiation site.

The proportion of stage Ⅰ area continues to increase as the stress amplitude decreases. As shown in Figure 3-12, compared with the cases of 368MPa and 280MPa, the MP specimen tested at 220 MPa has the largest stage Ⅰ area, which is almost half of the cross-section area.

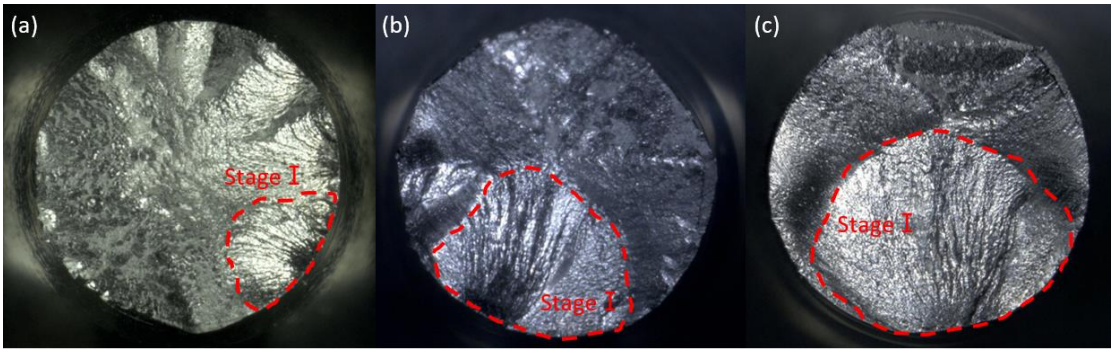

Figure 3-12. Fracture surfaces of MP states tested at: (a)368MPa; (b)280MPa; (c)220MPa.

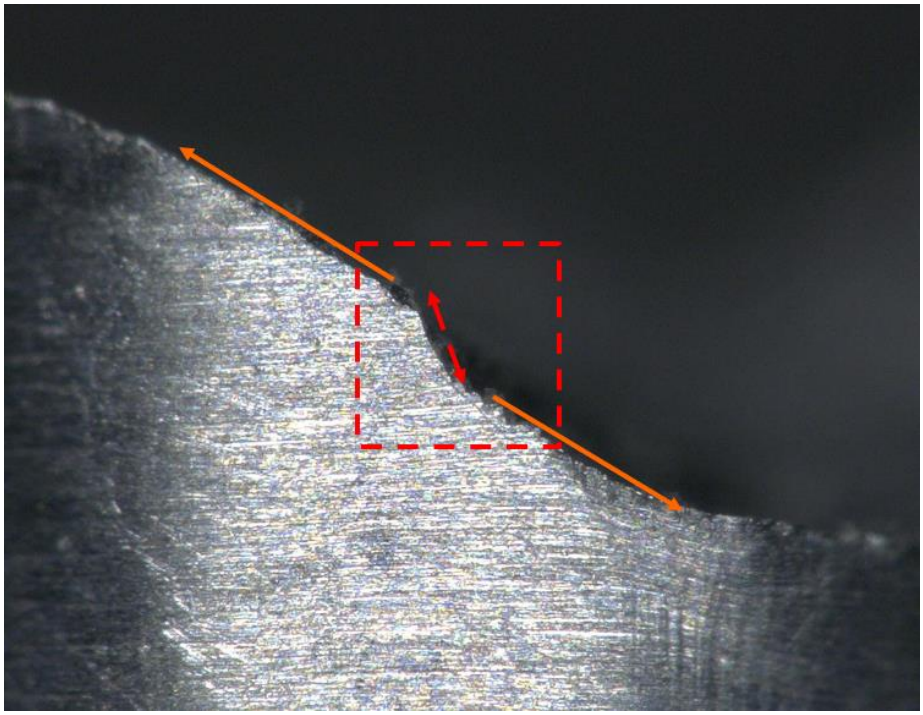

(a)

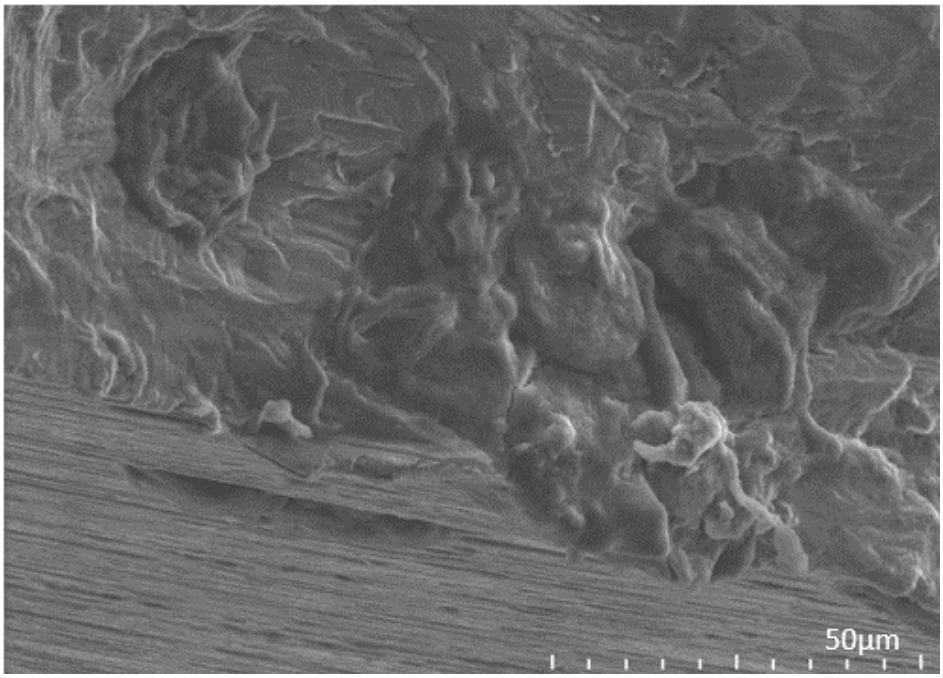

(b)

Figure 3-13. Observation of the crack initiation site of MP state tested at 220MPa: (a) Optical microscope; (b) SEM.

Although the specimen exhibits a fatigue life of more than 4×10^6 cycles, a crack initiation site is found on the top surface. As shown in Figure 3-13(a), the angle of the

crack path is also found different between the initiation site and the stage Ⅰ area, and this time the difference is even more significant. First, the crack initiates in the direction at an angle of about 68° to the specimen axis. Then, after a very short propagation, the crack changes direction to 29°. The value of the initiation angle is close to the plane of maximum principal stress, indicating a tensile crack rather than a shear or mixed crack. This can be confirmed by the SEM image in Figure 3-13(b), in which the extrusion of the surface material is more severe compared to the 280MPa case.

The transition of the cracking mode has also been reported in the literature. As mentioned in the research of Zhao[127], the modified SWT criterion[148,149] can be used to analyze and predict the cracking behavior, which has the expression as:

$$FP = 2b\Delta\varepsilon\langle\sigma_{max}\rangle + \frac{1-b}{2}\Delta\tau\Delta\gamma$$

Where FP is the fatigue parameter, b is the material parameter, where r and s are the normal stress and shear stress, respectively, in a material plane. e and c are the normal strain and shear strain corresponding to the normal stress, r, and the shear stress, s, respectively. The symbol D denotes the range in a loading cycle and the subscript ‘‘max’’ represents the maximum in a loading cycle. This criterion is applied to predict the cracking behavior of AA7075 material. The research[127] in the literature has concluded that AA7075 material exhibits different cracking modes when the material parameter b changes, which depends not only on the nature of material but also on the applied load level. As shown in Figure 3-14, for both tensile and torsional fatigue tests, the AA7075 material shows a tensile cracking when the parameter b is large and a shear cracking when b is small, and mixed cracking for intermediate values of b. While for AA7075, the parameter b increases as the load level decreases. A combined cracking mode can be found for intermediate load levels. Different cracking modes are also found for AA7075 when tested in multiaxial loading condition. As shown in Figure 3-15, the cracking modes for AA7075 under different loading conditions are summarized in a fracture mechanism map. From this map, it

can be clearly seen that for the cases in the present study – biaxial loading with a ratio of $1/\sqrt{3}$, stage Ⅰ fracture (shear cracking) can be found only for high stress amplitudes. When the stress amplitude is low, stage Ⅱ fracture (tensile cracking) is the common case, which is consistent with the observation in the present work.

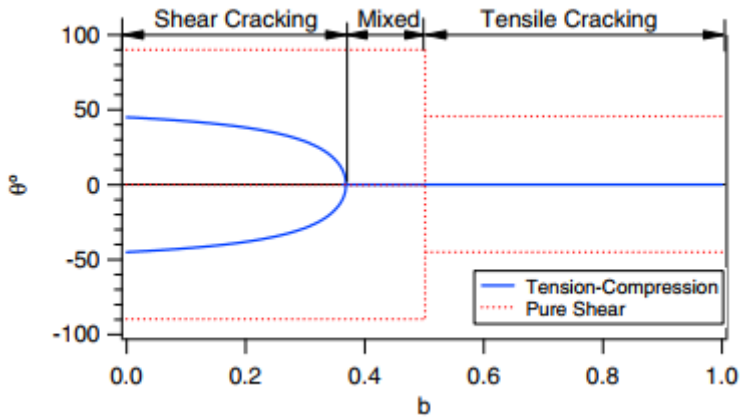

Figure 3-14. Dependence of cracking modes on material parameter b for fully reversed uniaxial and pure torsion loading[127]

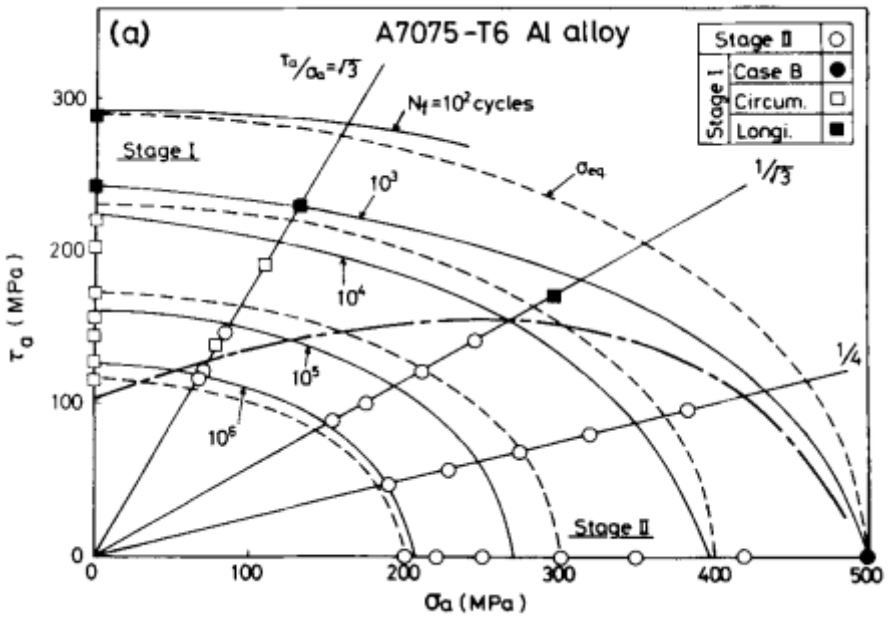

Figure 3-15. Fracture mechanism map for AA7075T6 alloy under combined axial and torsional loading [128]

In summary, the fracture mechanism of MP state material tested under biaxial loading varies at the load level. When tested at a high load level, the MP state material could exhibit multiple initiation sites and these sites are assumed to be shear-cracking.

Mixed-cracking appears when the stress amplitude decreases, and finally the crack initiation mechanism becomes tensile-cracking when the stress amplitude decreases to 220MPa. The transition of the fracture mechanism can explain the fitting problem in Section 3.3.

3.4.2 SMAT state

For the SMAT state, observation of the fracture surfaces is also presented in the order of stress level. Similar to the 368MPa case in MP state, the SMAT state specimen tested at a high stress level exhibits multiple initiation sites. As shown in Figure 3-16, taking the SMAT state specimen tested at 280MPa as an example, the stage Ⅰ area is even smaller than that of the MP state specimens tested at 368MPa. And when compared with MP state specimen tested at the same stress amplitude of 280MPa, it is obvious that only the SMAT specimen shows a multi-initiation phenomenon, which indicates that the poor surface integrity after SMAT may facilitate the initiation of fatigue cracks.

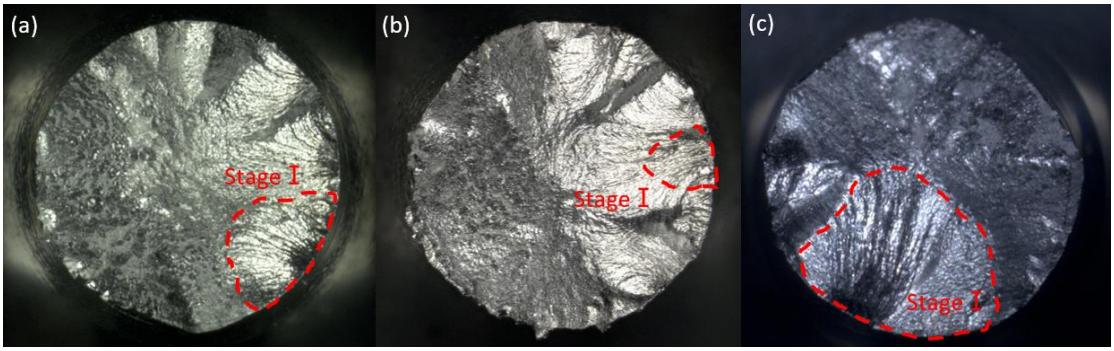

Figure 3-16. Observation of fracture surfaces of: (a) MP state 368MPa; (b) SMAT 280MPa; (c) MP 280MPa.

For SMAT specimens tested at intermediate stress levels such as 260MP and 240MPa, the fractography is presented in Figure 3-17. Single-sited crack initiation and stage Ⅰ area are more clearly observed in these cases.

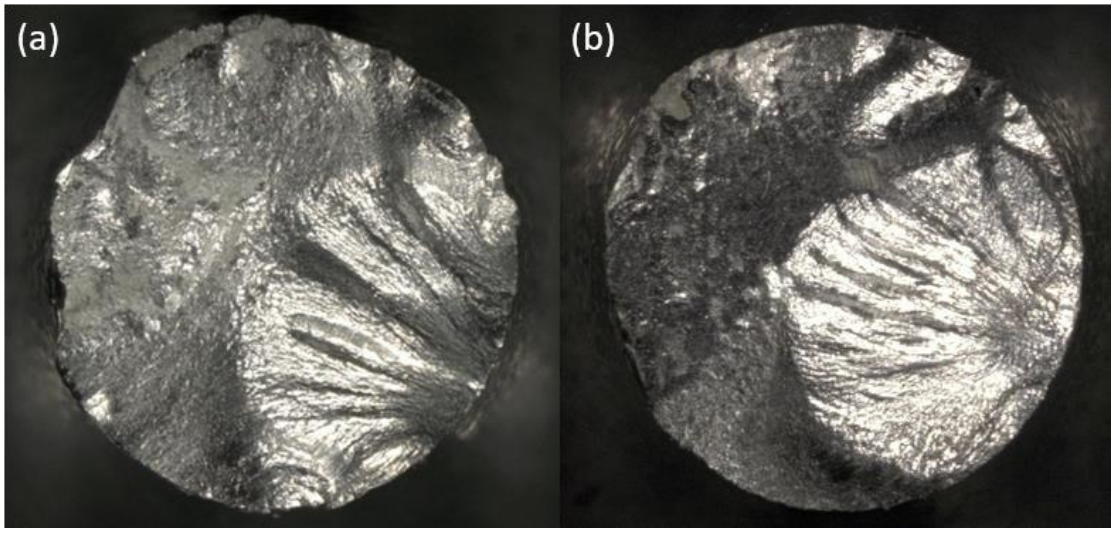

Figure 3-17. Fracture surface of SMAT specimens tested at: (a)260MPa;(b)230MPa.

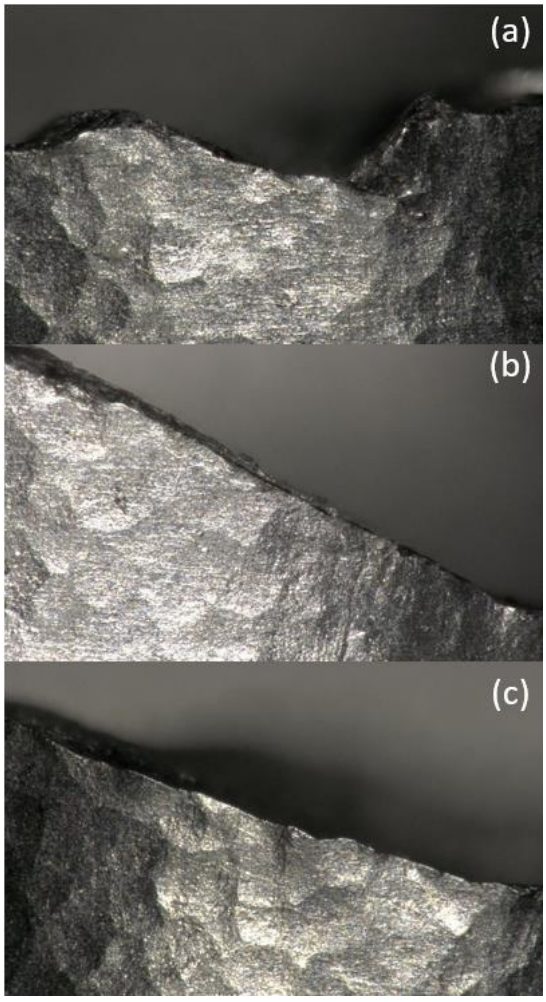

Figure 3-18. Lateral surfaces of SMAT state specimens tested at: (a) 280MPa; (b)240MPa; (c)230MPa.

However, it should be noted that the cracking angles of SMAT specimens barely change as the stress level decreases, as presented in Figure 3-18. The cracking angle

has a value close to the angle of stage Ⅰ area, indicating that the cracks are mainly driven by shear stress. The absence of the transition of cracking modes makes the fracture mechanism of the SMAT state different from that of the MP state. Since the transition phenomenon has been reported in the literature, the possible explanation could be that the SMAT retards the occurrence of tensile cracking.

Moreover, for SMAT specimens tested at extremely low stress levels such as 220 MPa, a SMAT-affected zone can be found on the fracture surface. As shown in Figure 3-19, a layer with a depth of approximately 340μm is present right beneath the surface of the material. A clear difference can be observed in this layer since the fracture surface is significantly less rough, compared to the inner material. The depth of this SMAT-affected zone is quite close to the depth of the SMAT-induced compressive residual stress layer, as highlighted in Section 2.4.2. A possible explanation may be that the compressive residual stresses generated by SMAT limit the effect of axial loading. Thus, the fractography of this layer is more similar to the that of a pure torsion case, where the fracture surface is likely to be flat due to the friction caused by torsion.



Figure 3-19. The SMAT-affected zone in a SMAT 220MPa case observed by SEM.

In summary, the fractography of the SMAT specimens indicates that the fracture

mechanism doesn't change much with stress levels. Most of the SMAT specimens exhibit a shear cracking phenomenon, instead of a tensile or combined cracking mode. The effect of SMAT can be verified by noting the SMAT-affected zone on the fracture surface, the depth of which appears to have the same value as the compressive residual stress layer.

3.5 Conclusion

The results of biaxial fatigue tests performed on both MP and SMAT state specimens are presented and discussed in this chapter.

First, the test conditions are presented, including the test equipment and test parameters. The results of the fatigue tests are then presented in the form of S-N curves, fitted Basquin equation and P-S-N curves. A comparison is made between the results of MP and SMAT specimens, and little difference in fatigue strength was found between these 2 states.

The analysis is also based on the observation of the fractured specimens. It is concluded that the fracture mechanism of the MP specimen changes from shear cracking to tensile cracking as the load level decreases. While most of the SMAT specimens exhibit only shear cracking behavior and tensile cracking can hardly be observed, indicating that the poor surface quality may retard the occurrence of tensile cracking.

Chapter 4 Analysis of fatigue properties affected by SMAT

The conclusion of Chapter 3 indicates that the difference in fatigue strength between the MP and SMAT states is not significant. In fact, the fatigue strength of SMATed material even decreases compared with that of the MP state, especially at relatively lower load levels. Nevertheless, the research on SMAT has demonstrated its capability of enhancing fatigue resistance for different metallic materials. This contradiction between the results in the literature and the present work may indicate that the effect of SMAT on the fatigue strength of AA7075 is complex. Both detrimental and beneficial factors are induced by SMAT, and these factors compete with each other to determine fatigue lives. This chapter presents and discusses an analysis of these factors on the effect of SMAT in order to further understand the influencing mechanism of SMAT on the fatigue strength of AA7075.

4.1 Effect of surface integrity on fatigue properties after SMAT

4.1.1 Post-SMAT electropolishing process

As demonstrated in Chapter 2, the surface of AA7075 material can be totally modified by SMAT. The formation of dimples with irregular size and shape on the surface is a consequence of severe plastic deformation. In general, such deformation appears to be homogeneous throughout the treated area. However, upon closer examination with higher magnification, defects such as pits and microcracks can be observed. As illustrated in Figure 4-1, the surface subjected to SMAT displays a number of defects when observed under a scanning electron microscope (SEM).

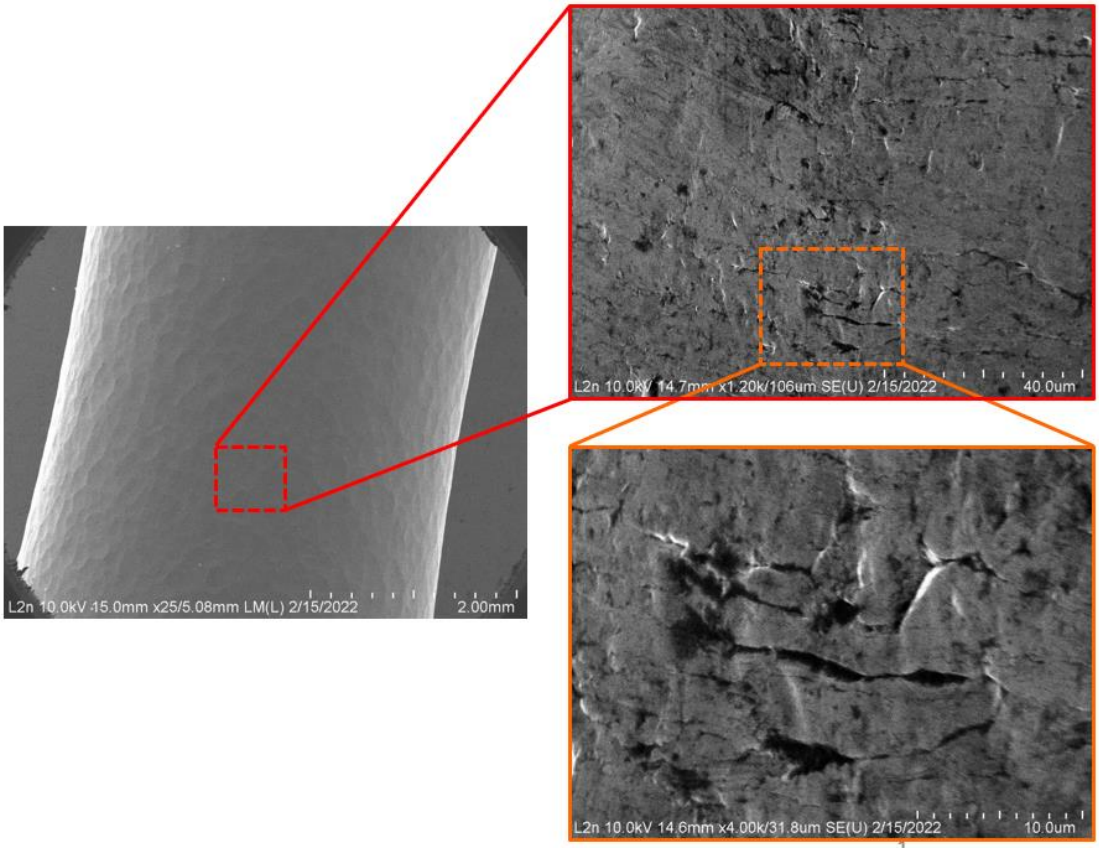

Figure 4-1. Microcracks observed with SEM on a SMATed surface

Similar micro defects are also mentioned in some research on AA7075 treated by SMAT. For example, it is found that the defects on the SMATed surface cannot be neglected when analyzing the sources of crack initiation. Some researchers even draw conclusions that materials like AA7075 are too notch-sensitive to be surface modified [112].

In order to ascertain the extent to which surface integrity affects fatigue strength following SMAT, a specially-designed experiment is conducted in this study. In order to negate the detrimental impact of surface integrity, post-SMAT polishing is incorporated into the present study. Mechanical polishing techniques using emery papers or vibration polishing machines are not employed in order to prevent any relaxation of residual stress due to deformation during polishing.

Consequently, electropolishing is considered an optimal method for the removal of superficial material. According to the literature, a solution comprising perchloric acid and ethanol is employed as the electrolyte. The volume ratio of the perchloric acid and ethanol is 2:8. Given that the samples to be polished in this study are fatigue

specimens with cylindrical shapes, standard electropolishing devices are unsuitable for the polishing of the specimens' surfaces in a uniform manner. In this work, an electropolishing device is set up for cylindrical specimens. As illustrated in Figure 4-2, the device consists of a power supply, an electrolytic tank, an anode and a cathode. A magnetic stirring machine is applied to stir the electrolyte in the electrolytic tank, which is a metallic beaker. The efficiency of the electropolishing is reported in relation to the current density acting on the polished area. The cylindrical shape of the electrolytic tank and the stirring of the electrolyte are assumed to ensure that the current density is homogeneously distributed. Paraffin is used to cover the specimen, with the exception of the area to be polished, as shown in Figure 4-3(b).

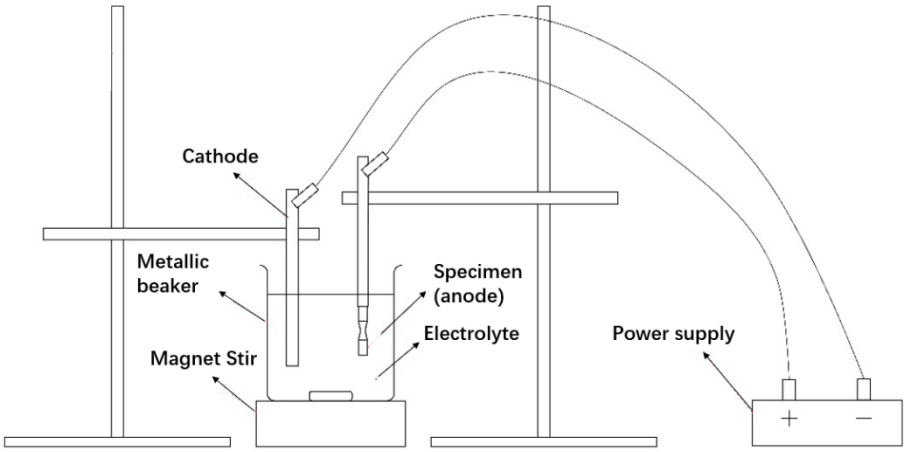

Figure 4-2. Schematic of the electropolishing device for cylindrical specimens

Given that the current density is assumed to be stable throughout the polishing process, the thickness of the layer removed by electropolishing should be proportional to the polishing time. The peak-to-valley surface roughness of SMAT material is measured as slightly more than 10μm. Therefore, a layer of superficial material with a thickness of 15 μm should be removed by electropolishing. As discussed in Chapter 2, the residual stress profile exhibits a peak value at a depth of 50–75 μm. Therefore, the residual stress at a depth of 15 μm should be slightly higher than the value at the top surface. Consequently, the removal of a 15 μm thick layer would not significantly impact the surface state, with the exception of roughness.

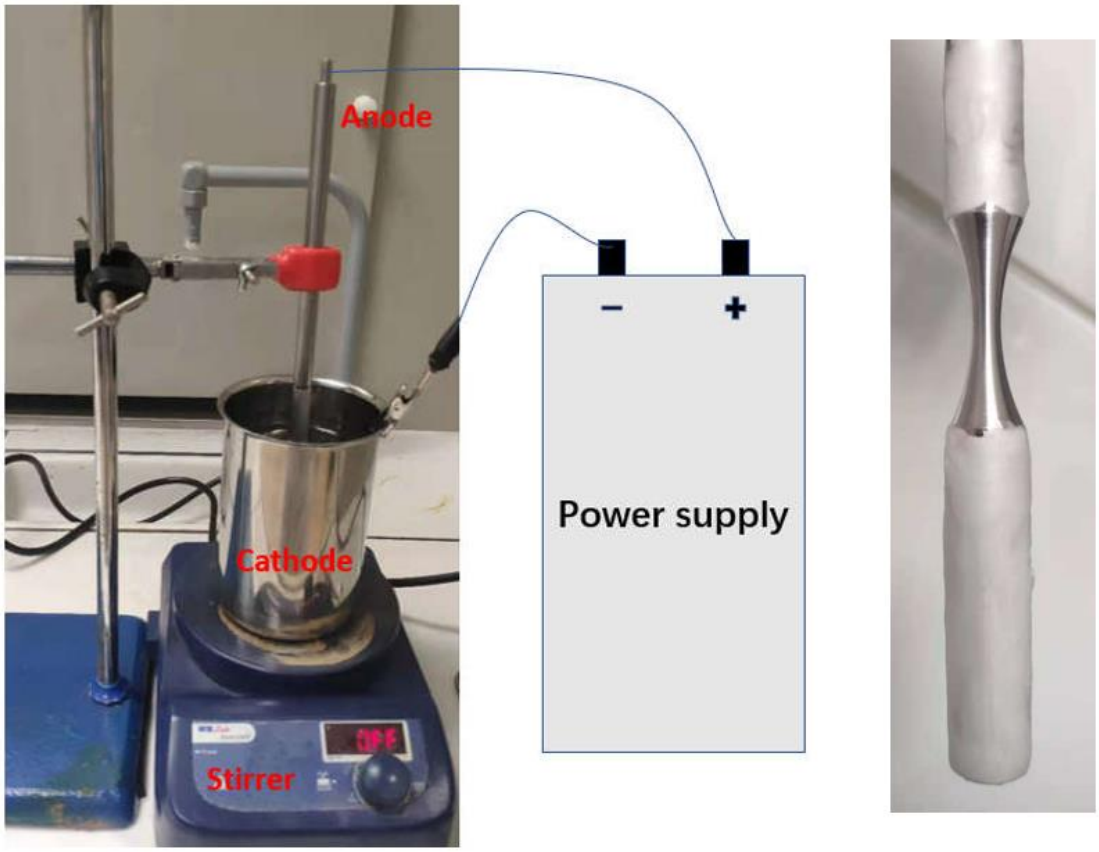

Figure 4-3. (a) Set-up of the electropolishing device in the lab; (b) a specimen to be polished

Figure 4-4 illustrates the impact of electropolishing. The dimples on the SMATed surface (Figure 4-4(a)) are eliminated after electropolishing (Figure 4-4(b)), as are any potential microcracks. While some porosity persists (Figure 4-4(d)), the polished surface exhibits superior surface quality in comparison to the SMAT state. A roughness measurement was conducted. The maximum height value $R_t$of the polished surface decreased from 18 µm to 3 µm, while the mean height value $R_a$decreased from 0.96 µm to 0.33 µm. These quantitative measurements demonstrate the improvement in surface quality. Figure 4-5 presents the profile of the roughness measurement.

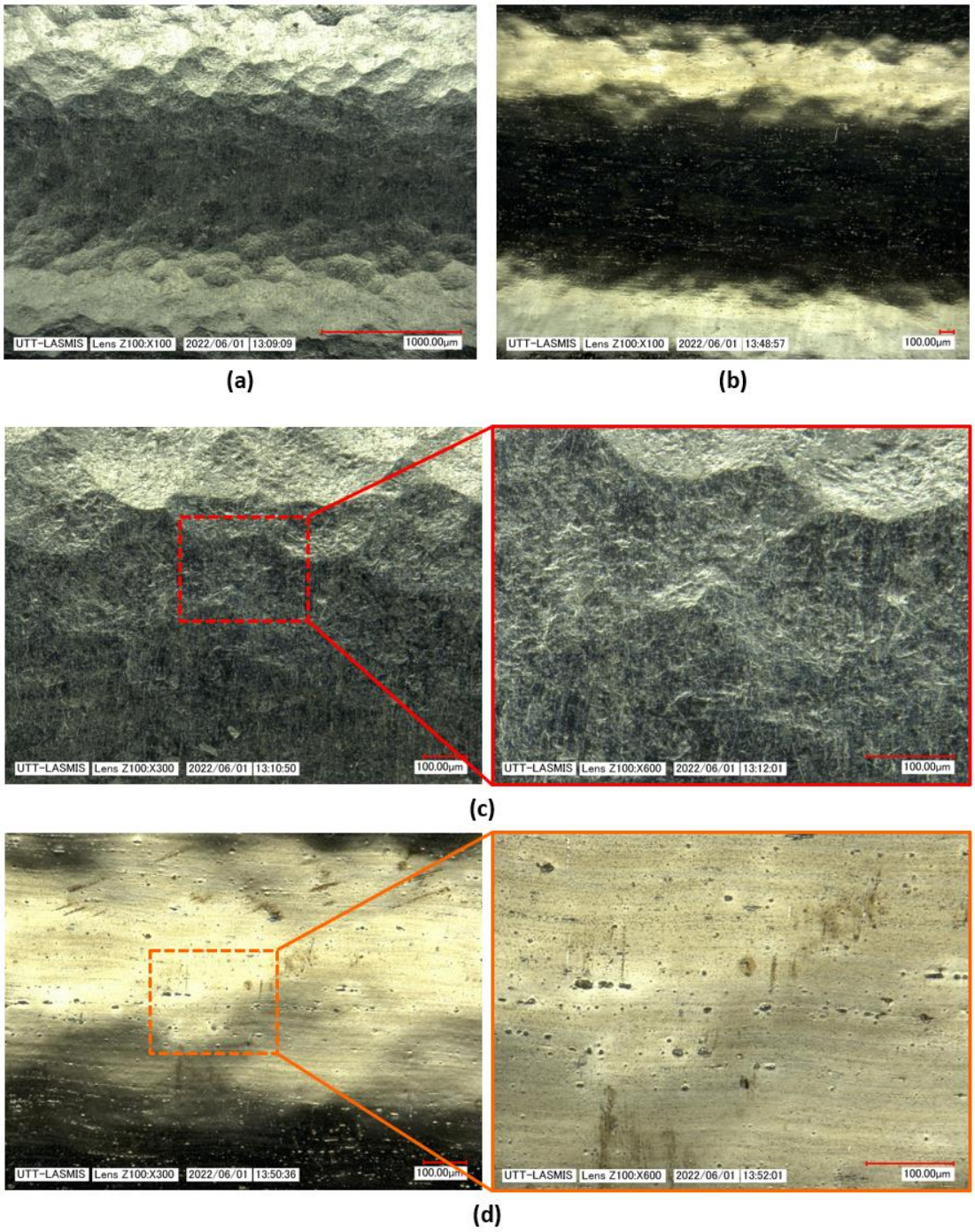

Figure 4-4. Comparison between surfaces in SMAT and SMAT-EP states: (a) SMAT; (b) SMAT-EP; (c) details of SMAT surface; (d) details of SMAT-EP surface.

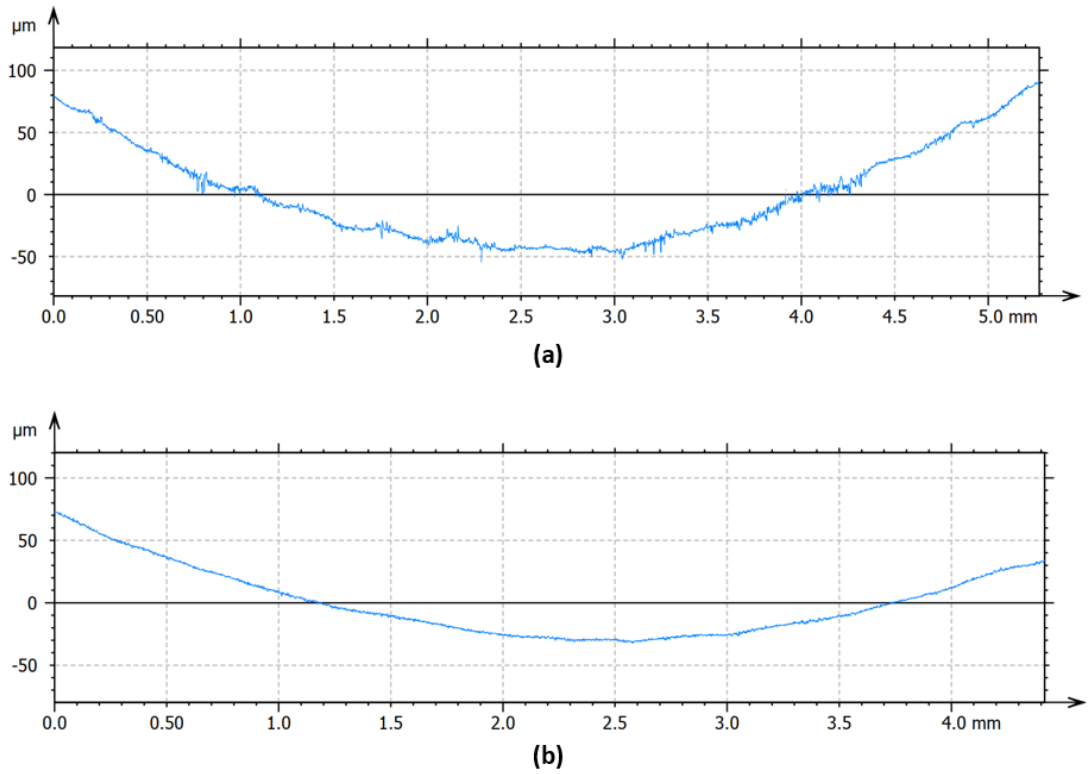

Figure 4-5. Profile of (a) SMAT and (b) SMAT-EP surface.

4.1.2 Fatigue strength of SMAT-EP specimens

4.1.2.1 S-N data plots and analysis

Biaxial fatigue tests, as outlined in Chapter 3, were also conducted with specimens processed by SMAT and electropolishing (hereinafter referred to as 'SMAT-EP'). It is important to note that calibration of stress amplitude is based on the measurement of the diameter of the polished specimens.

The outcomes of the fatigue tests conducted with SMAT-EP specimens are presented in the S-N plots in Figure 4-6, along with a comparison of the results with those obtained in the MP and SMAT states.

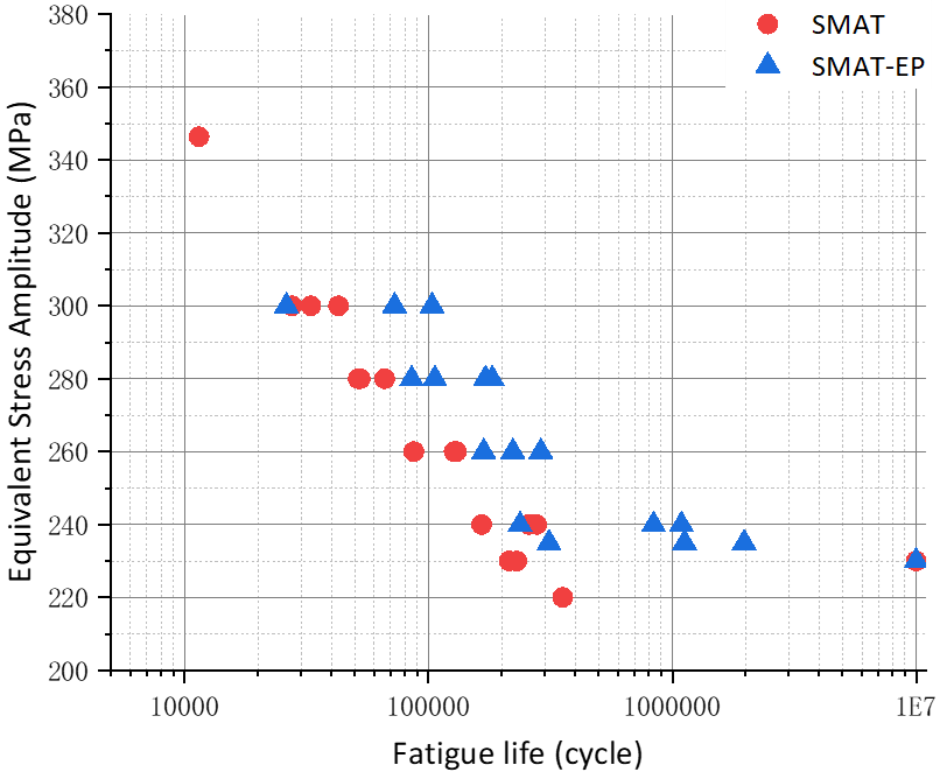

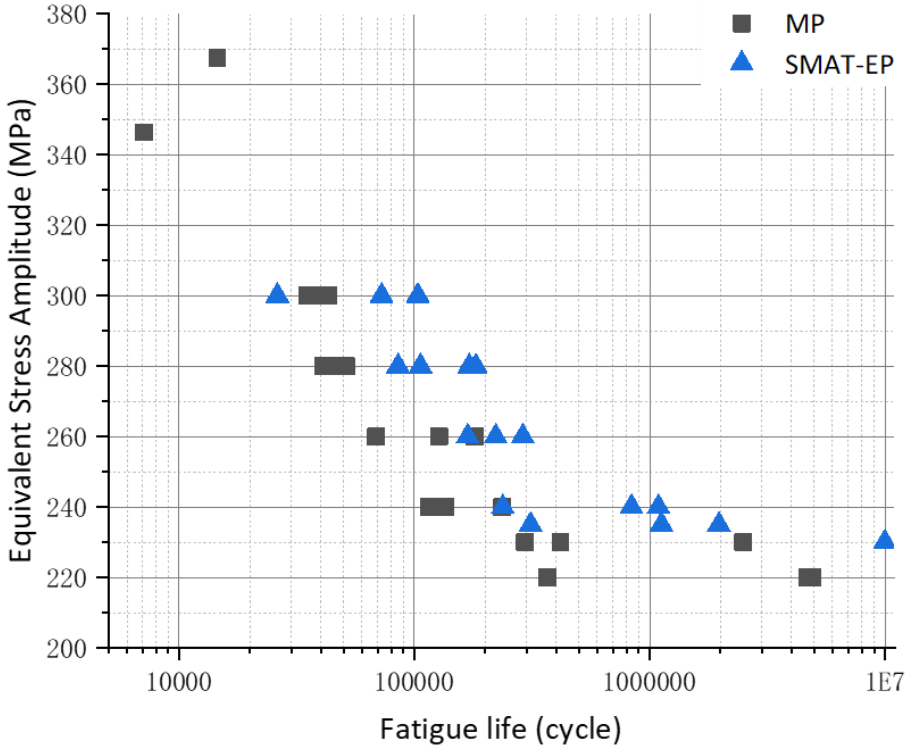

Figure 4-6. Comparison in S-N plots of (a) SMAT and SMAT-EP; (b) MP and SMAT-EP.

Figure 4-6(a) presents the results of tests conducted on SMAT and SMAT-EP specimens. The data indicate that SMAT-EP specimens exhibit higher fatigue strength than SMAT specimens, particularly when tested at relatively lower stress amplitudes.

However, at relatively high loading levels, such as tests at amplitudes exceeding 300 MPa, the difference is not as pronounced. At intermediate load levels, such as 280 MPa and 260 MPa, the difference between SMAT and SMAT-EP states becomes more pronounced. In this regime, at the same stress amplitude, SMAT-EP specimens exhibit fatigue life approximately 80% to 100% longer than SMAT specimens. This represents a significant increase in fatigue strength. For relatively low stress levels, such as tests with stress amplitudes less than 240 MPa, the SMAT-EP specimens exhibit an extremely remarkable enhancement in fatigue strength. SMAT-EP specimens tested at 240 MPa attain fatigue lives close to or even more than 10^6 cycles, which is approximately 300% more than the SMAT state. It is also noteworthy that the data points for the SMAT-EP state are less scattered than those for the SMAT state. This may indicate that the polishing process mitigates the influence of surface quality on the fatigue strength. A comparison between the SMAT-EP and MP states is presented in Figure 4-6(b). The SMAT-EP specimens achieve longer fatigue life than the MP specimens.

4.1.2.2 Fractographic analysis of SMAT-EP state

As previously discussed in Chapter 3, the fractography of SMAT state exhibits differences when observed with an optical microscope compared with MP state. The main difference occurs at the subsurface region, where the SMAT-affected zone can be observed. This section will discuss the fractography of SMAT-EP specimens.

For SMAT-EP specimens subjected to relatively high loading levels, for instance with an equivalent stress amplitude of 300 MPa, the fracture surface displays a "factory-roof" morphology (Figure 4-7), which is commonly observed in fatigue tests with uniaxial pure torsional fatigue tests [150] and also observed in both MP and SMAT specimens. Although similar "factory-roof" and multiple crack initiation sites are observed, slight differences can be found. The number and size of "roofs" are smaller on SMAT-EP specimens.

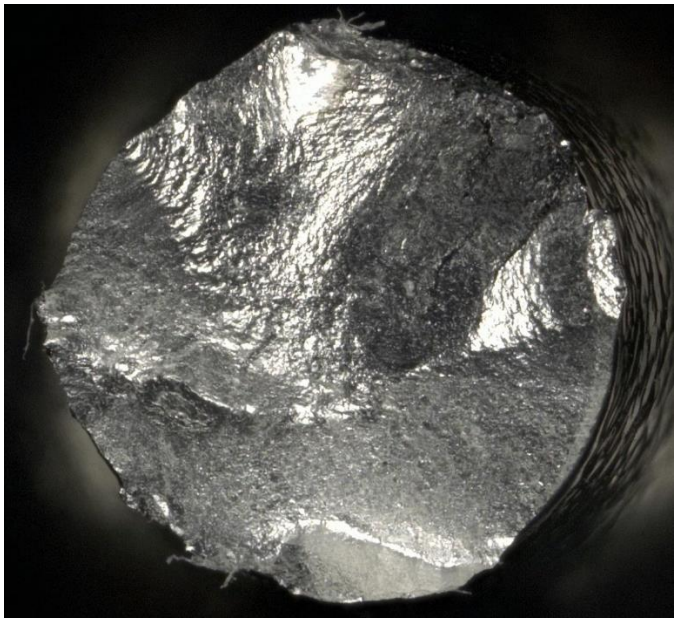

Figure 4-7. Image of fracture surface of a SMAT-EP specimen tested at 300MPa

With regard to the crack initiation angle observed at intermediate load levels, the SMAT-EP specimens exhibit no significant difference. As illustrated in Figure 4-8, the crack initiation angles for specimens tested at 280 MPa, 260 MPa and 240 MPa are all found to be approximately 30°, which is comparable to that of the SMAT state. The aforementioned observations lead to the conclusion that the fracture mechanism of SMAT-EP specimens remains unchanged in comparison to the SMAT state.

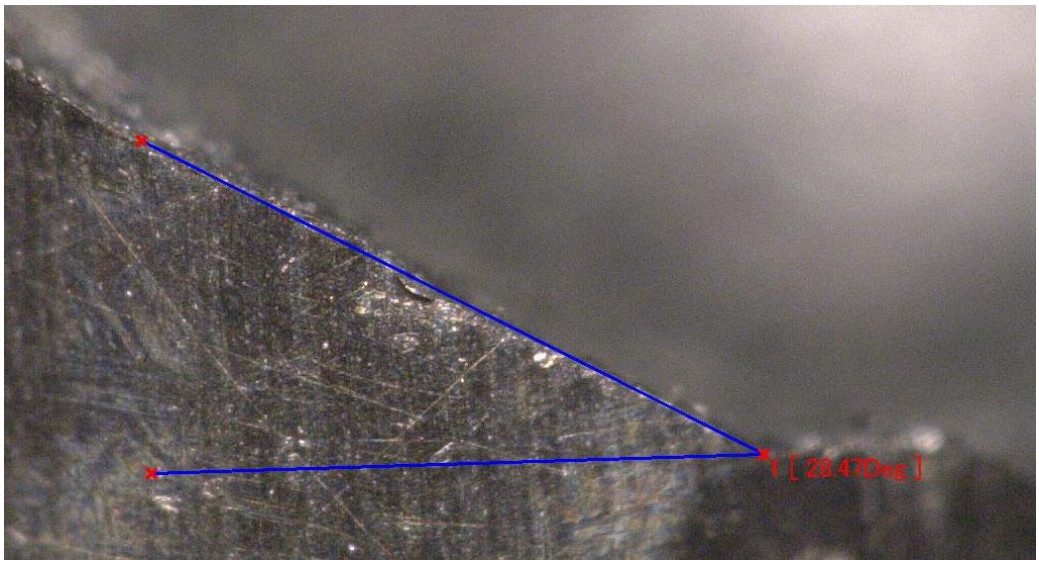

(a)

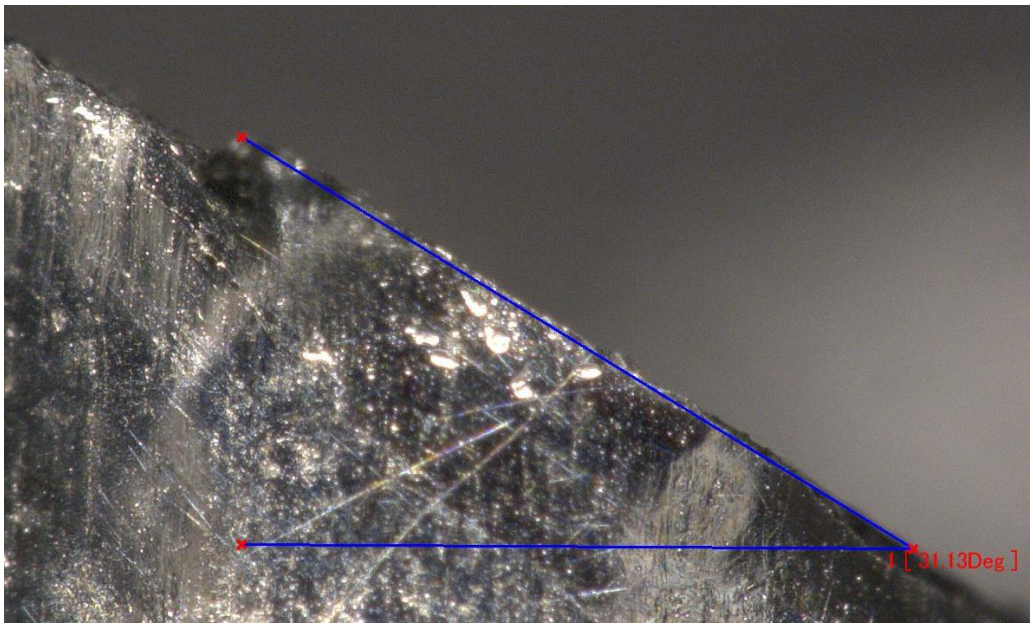

(b)

Figure 4-8. Crack initiation angle of a SMAT-EP specimens tested at (a) 260MPa; (b) 240MPa

The primary distinction between SMAT-EP and SMAT or MP states is the presence of interior initiation sites, which can only be discerned on SMAT specimens at extremely low loading levels (220 MPa) and never observed on MP specimens. While for SMAT-EP specimens, interior crack initiation sites can be observed when tested at 240 MPa (Figure 4-9) and 230 MPa. The presence of interior initiation sites is observed in the SMAT-EP state at a higher loading level than in the SMAT state. This suggests that the poor surface quality, particularly the micro defects on the SMATed surface, may still be considered the primary source of crack initiation even at low load levels, when the interior initiation should have occurred. The relatively delayed interior initiation phenomenon provides further evidence that poor surface integrity is the primary detrimental factor influencing fatigue strength after SMAT.

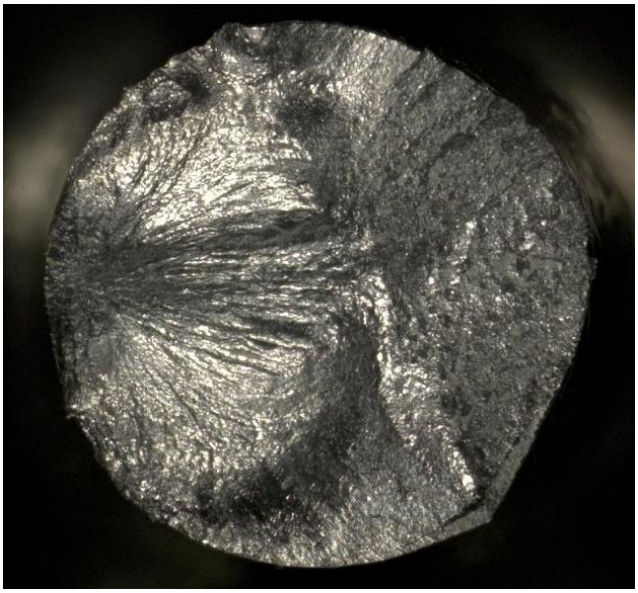

(a)

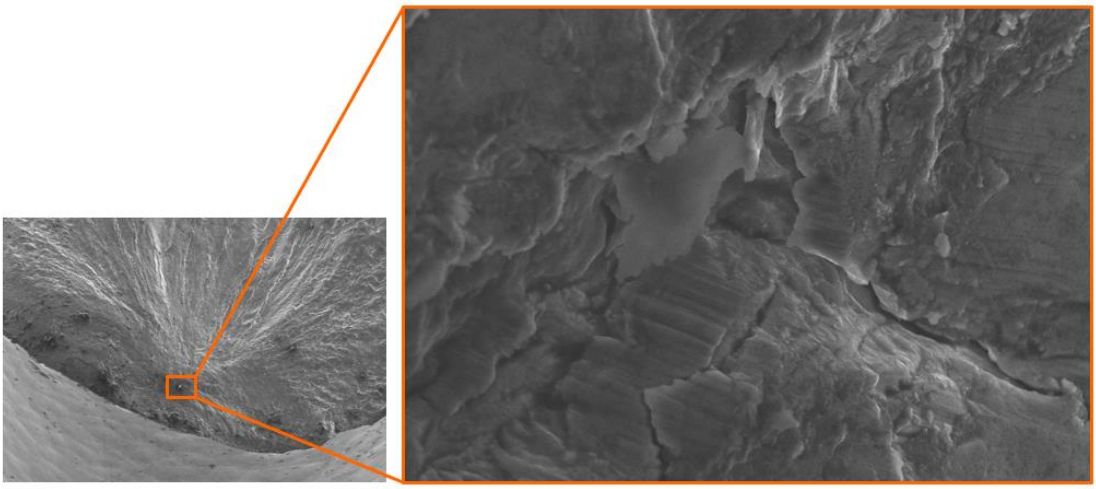

(b)

Figure 4-9. (a) fractography of a SMAT-EP specimen tested at 240MPa; (b) SEM image of (a) with an interior crack initiation site observed.

4.2 Effect of SMAT-induced residual stresses on fatigue properties

4.2.1 Evolution of residual stress and FWHM during cyclic loadings

It is widely acknowledged that residual stress plays a pivotal role in fatigue behaviors. As outlined in Chapter 1[84,104,105], residual stress is recognized as a key factor in enhancing resistance to both crack initiation and crack propagation. However, it is important to note that the relaxation of residual stress during cyclic loading in fatigue

tests can not to be overlooked. This relaxation can be attributed to the movement of dislocations during the deformation cycle, and it can start from the initial cycle of fatigue loading. It may persist for a certain number of cycles before reaching a state of equilibrium. The proportion of relaxed residual stress is dependent on the applied load level. In this study, the relaxation of residual stress is investigated experimentally. SMATed specimens are measured by XRD, followed by fatigue tests. The fatigue tests are interrupted on purpose so that the specimens can be unloaded from the testing machine and measured by XRD before being reloaded and tested again. The first interruption is set at the early stage of the cyclic loading (less than 5% of the total fatigue life). The XRD measurements are conducted until the residual stress value stabilizes, allowing for the comprehensive assessment of the residual stress evolution throughout the cyclic loading process. Two load levels, 300 MPa and 240 MPa, are selected as representative of high and low load levels, respectively.

The results of the relaxation measurement are presented in Figure 4-10. Figure 4-10(a) depicts the evolution of residual stresses on the surface of SMATed specimens during an interrupted fatigue test at an amplitude of 300 MPa. The line in red represents the initial residual stress, which is approximately -155 MPa. It can be observed that the relaxation of the residual stress starts at the beginning of the fatigue test. Within the first 500 loading cycles (approximately 1% of the total lifetime), the value of the compressive residual stress drops drastically from -155MPa to around -120MPa. From 500 to 5000 cycles, the relaxation rate gradually decreases. The compressive residual stress remains at about -90MPa at 5000 cycles. The compressive residual stress continues to decrease at a slow rate until 15000 cycles, which represents approximately one-third of the total lifetime of the specimens tested at 300 MPa. After 15000 cycles, the residual stress fluctuates around -80 MPa, which is assumed to be the stabilized value of the residual stress for the remainder of the fatigue test. The evolution of FWHM is also presented in the figure, and it has a similar trend to that of the residual stress. The difference is that FWHM value exhibits a longer stage of ‘slow decrease’ from 5000 to 25000 cycles before its stabilization. The proportion of residual stress relaxed is approximately 48%.

Figure 4-10(b) illustrates the evolution of residual stress and FWHM in a SMAT specimen subjected to a relatively lower stress amplitude of 240 MPa. The relaxation curve is comparable to that observed at 300 MPa, comprising three distinct phases: a rapid decrease, a steady decrease, and a stabilized phase. Given the difference in total lifetime, each phase for the 240 MPa test has a relatively longer duration. The tested specimen stabilizes its residual stress at approximately 30,000 to 40,000 cycles, which represents approximately 15% of the total lifetime at a load level of 240 MPa. The stabilized residual stress value is approximately -105 MPa, which accounts for 72% of the initial value of -145 MPa.

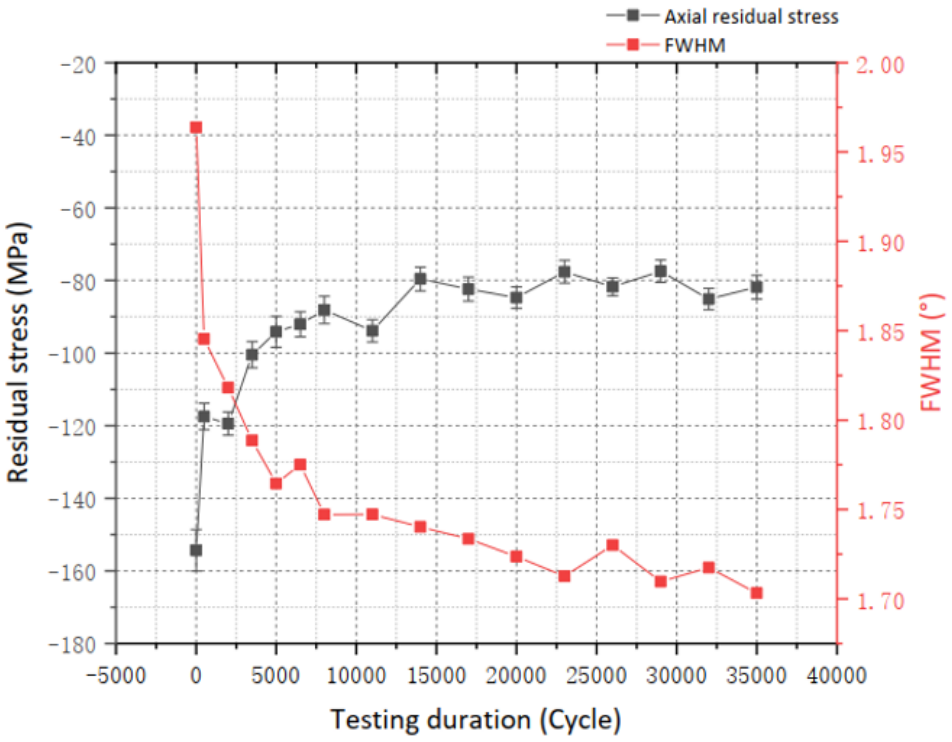

(a)

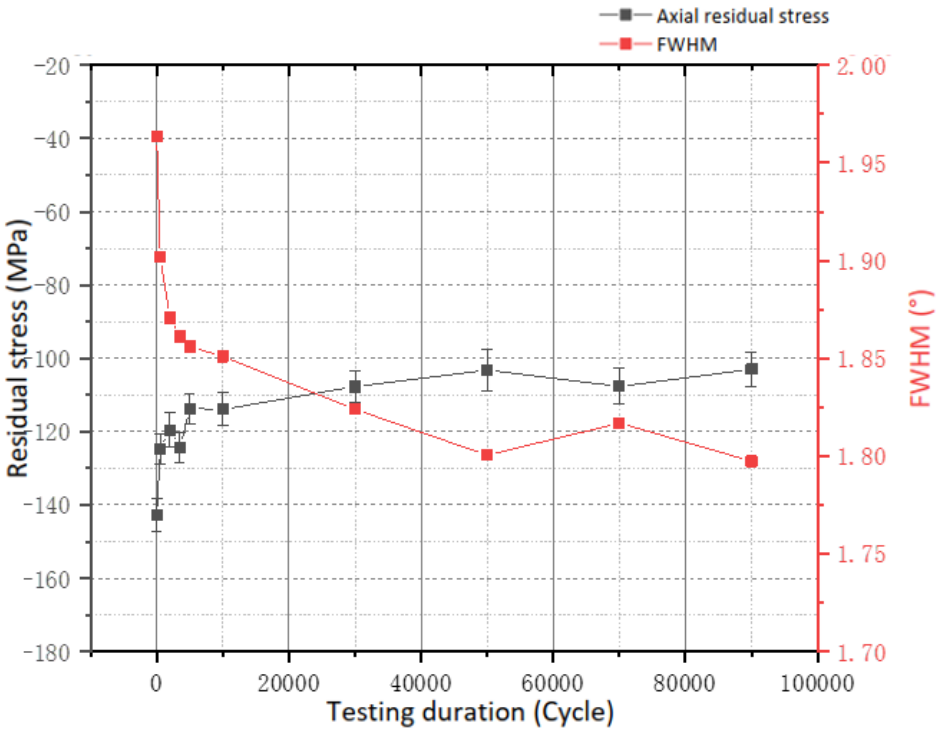

(b)

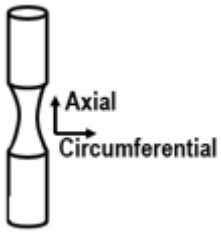

(c)

Figure 4-10. Evolution of residual stress and FWHM during cyclic loading: (a) 300MPa; (b) 240MPa. And (c): coordinate system of the cylindrical specimen

4.2.2 Post-SMAT heat treatment and its effect

A quantitative investigation is conducted to ascertain the extent to which residual stress affects fatigue strength. However, since residual stress is always generated in conjunction with work hardening, it is challenging to eliminate the effect of residual stress or work hardening in isolation. In this study, post-SMAT heat treatment is employed to neutralize the effect of both residual stress and work hardening.

As previously discussed in Chapter 1[77,151,152], the annealing treatment is a common method for reducing residual stress and work hardening. The most commonly selected temperature is 185°C, which allows for the efficient reduction of

residual stress while minimizing significant changes in microstructure. Figure 4-11 illustrates the evolution of both residual stress and FWHM as a function of annealing time. It can be observed that most of the compressive residual stress is removed within the first two hours of annealing, while the remainder can be disregarded, due to the inherent inaccuracy of the XRD measurements. The evolution of FWHM is analogous. Consequently, a post-SMAT annealing of nine hours is considered sufficient to remove the residual stress and work hardening induced by SMAT without recrystallisation.

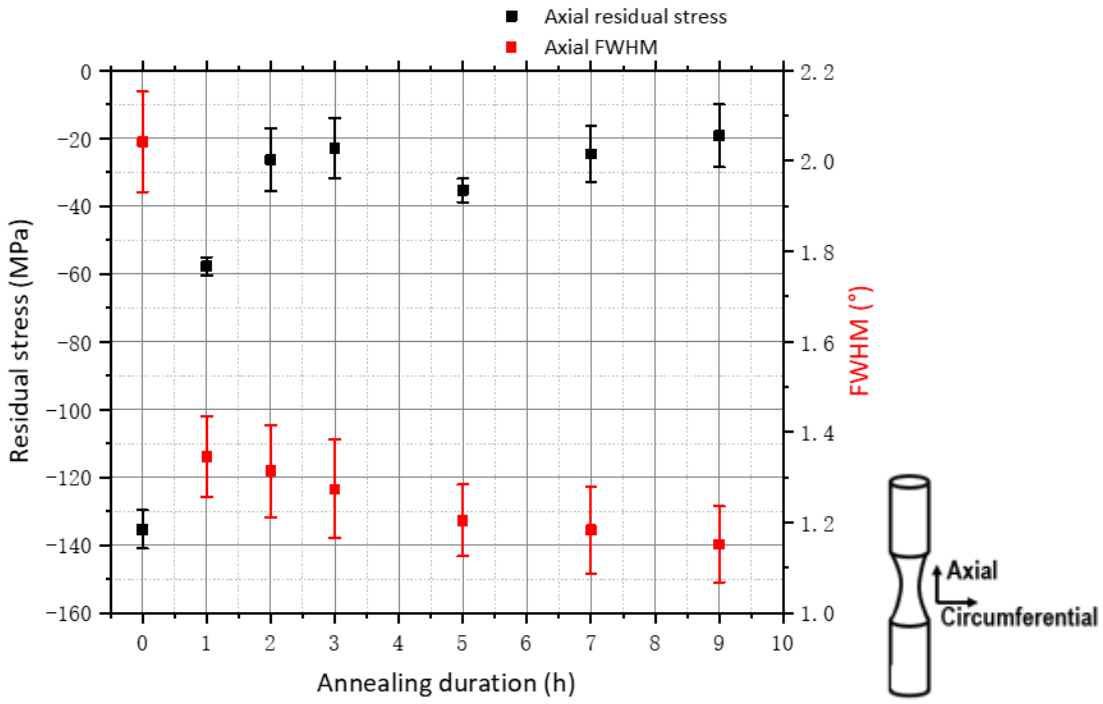

Figure 4-11. Evolution of residual stress and FWHM during post-SMAT heat treatment.

Four fatigue tests were conducted on specimens treated by SMAT and post-SMAT annealing (hereinafter referred to as 'SMAT-HT'). The results of these two tests are plotted in the S-N plots of SMAT specimens in order to facilitate a clear comparison. In Figure 4-12, the data points marked by red circles represent the results from SMAT-HT specimens. It is evident that the fatigue life of a SMAT-HT specimen is considerably shorter than that of a SMAT specimen when subjected to the same stress amplitude. The SMAT-HT specimen tested at a stress amplitude of 260 MPa exhibits a fatigue lifetime that is marginally longer than 104 cycles, which represents approximately 10% of the lifetime of SMAT specimens at the same stress amplitude. This pronounced disparity in fatigue strength serves to corroborate the advantageous influence of

residual stress and work hardening.

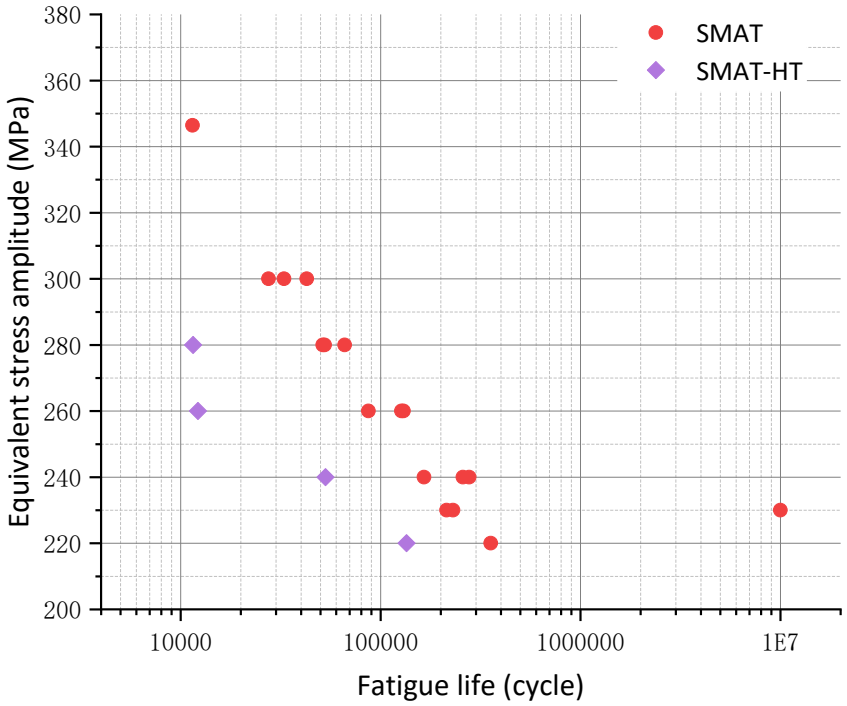

Figure 4-12. S-N plots of SMAT-HT specimens compared with SMAT state

The fractography of SMAT-HT specimens also reveals differences when compared with SMAT specimens. To illustrate, consider a SMAT-EP specimen tested at 240 MPa. As shown in Figure 4-13(a), the fracture surface of this SMAT-EP specimen is markedly rough. When examined in the direction indicated by the blue arrow, the lateral surface reveals the presence of a crack initiation site at the border of a SMAT-induced dimple. This observation is not evident in SMAT specimens, which suggests that the presence of SMAT-induced residual stresses plays a critical role in impeding crack propagation along the boundaries of SMAT-induced dimples.

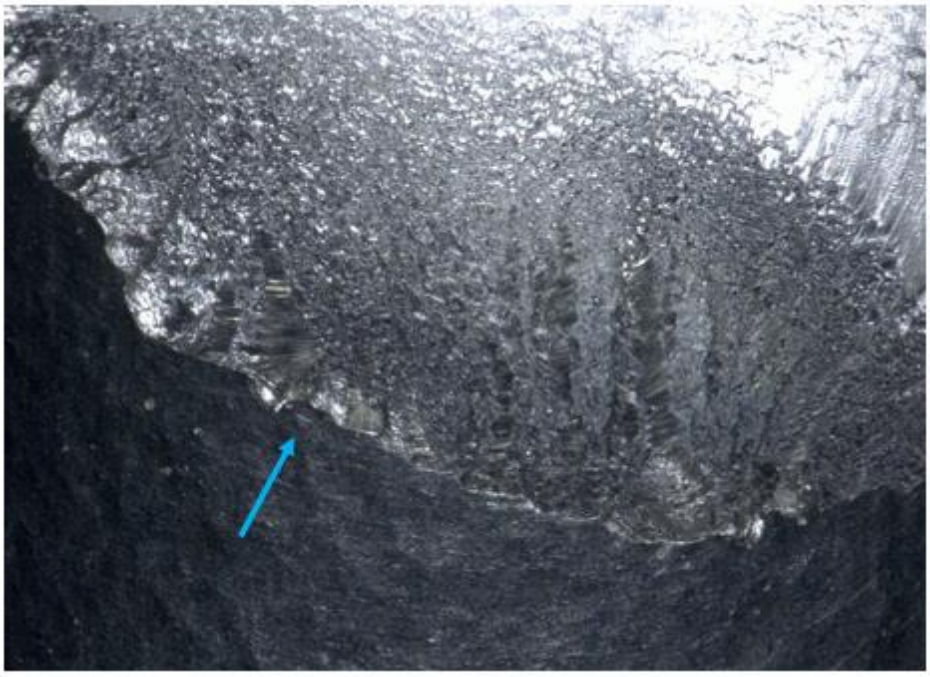

(a)

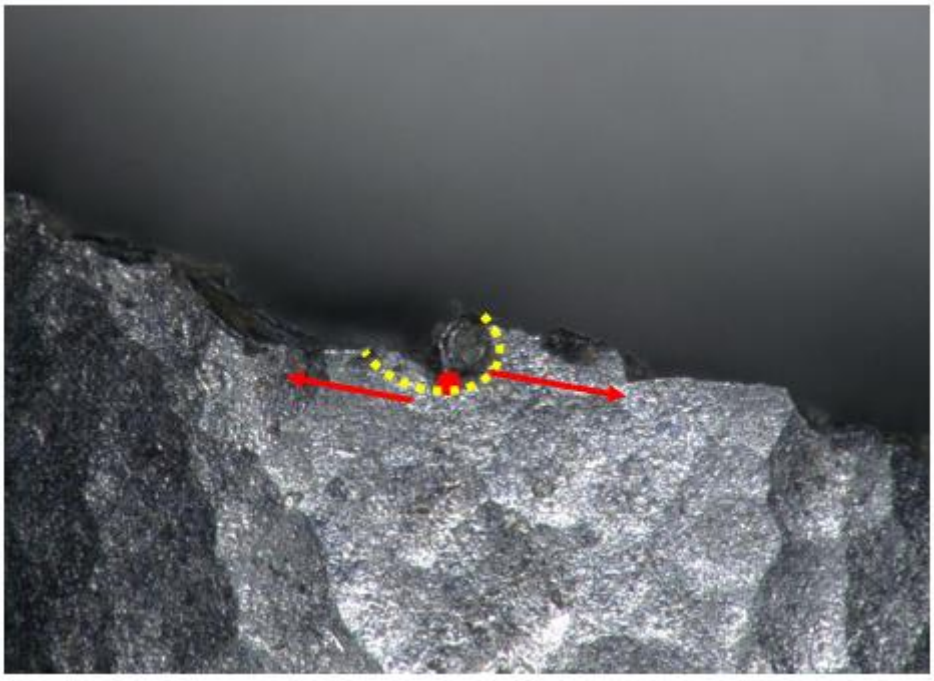

(b)

Figure 4-13. (a) Microscopic image of the fracture surface of a SMAT-HT specimen tested at 240MPa; (b) Observation in the direction marked in blue in (a).

4.3 Effect of grain refinement on fatigue properties

It is well established that grain size can influence the resistance to crack initiation and propagation when analyzing the fatigue strength of a material[101–103]. Previous research[153,154] has demonstrated that SMAT is capable of introducing a refined microstructure in the surface and subsurface areas of treated materials. Consequently, the present work also investigates the effect of grain refinement induced by SMAT.

As previously discussed, the effects of surface integrity and residual stresses are eliminated by post-SMAT electropolishing and post-SMAT annealing, respectively. A combination of these two post-SMAT treatments is believed to be capable of presenting a post-SMAT state which keeps only the grain refinement compared with the non-SMAT state. The process parameters for post-SMAT electropolishing and annealing are selected to be the same as those mentioned in sections 4.1 and 4.2. Several specimens are prepared with a combined EP and HT process (hereinafter referred to as 'SMAT-EP-HT'), and then tested at three stress amplitudes. The stress levels were set at 280 MPa, 240 MPa, and 220 MPa, which corresponds to high, intermediate, and low load levels, respectively. The results of these tests are recorded and plotted in Figure 4-14.

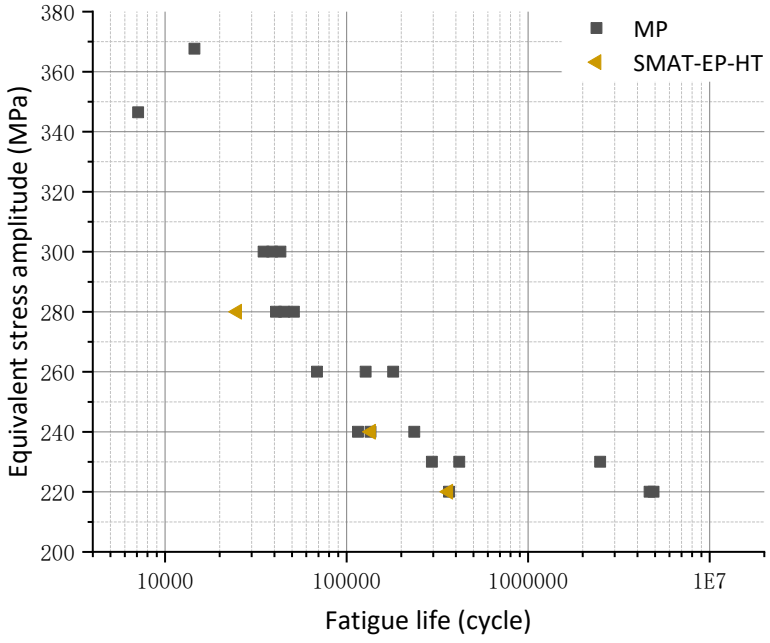

Figure 4-14. S-N plots of SMAT-EP-HT compared with MP state

As illustrated in Figure 4-14, the SMAT-EP-HT specimen tested at 280 MPa exhibits a shorter fatigue lifetime (approximately 1/3) compared with the MP state. This indicates that the grain refinement may accelerate the crack initiation and propagation compared with the MP state. For the intermediate load level of 240 MPa, the SMAT-EP-HT specimen shows no significant difference from the MP specimens. The SMAT-EP-HT specimen tested at a low load level exhibits an extremely shorter fatigue life compared with the MP state. However, due to the scattered nature of the fatigue test data in this regime, it can only be concluded that the potential grain refinement doesn't increase the fatigue strength, but decreases it.

4.4 Effect of MP-induced residual stresses and work hardening

As previously stated in Chapter 2, the fatigue test specimens are prepared in accordance with the following procedure: pre-SMAT heat treatment (a combination of solution annealing and annealing), pre-SMAT mechanical polishing, SMAT and post-SMAT treatment. The sequence of the pre-SMAT treatment may give rise to the concern that residual stresses may be introduced into the surface of materials following mechanical polishing. This may also contribute to the observed difference between the MP and SMAT states.

The results of the XRD measurements provide evidence for the existence of MP-induced residual stresses (hereinafter referred to as 'MP-RS'). As shown in Figure 4-15, the blue triangular dots demonstrate the axial distribution of MP-RS. The maximum value of MP-RS was found to be approximately -50 MPa, which is approximately one-third of the value of SMAT-RS. However, the depth of the distribution of MP-RS was found to be much less than that of SMAT-RS.

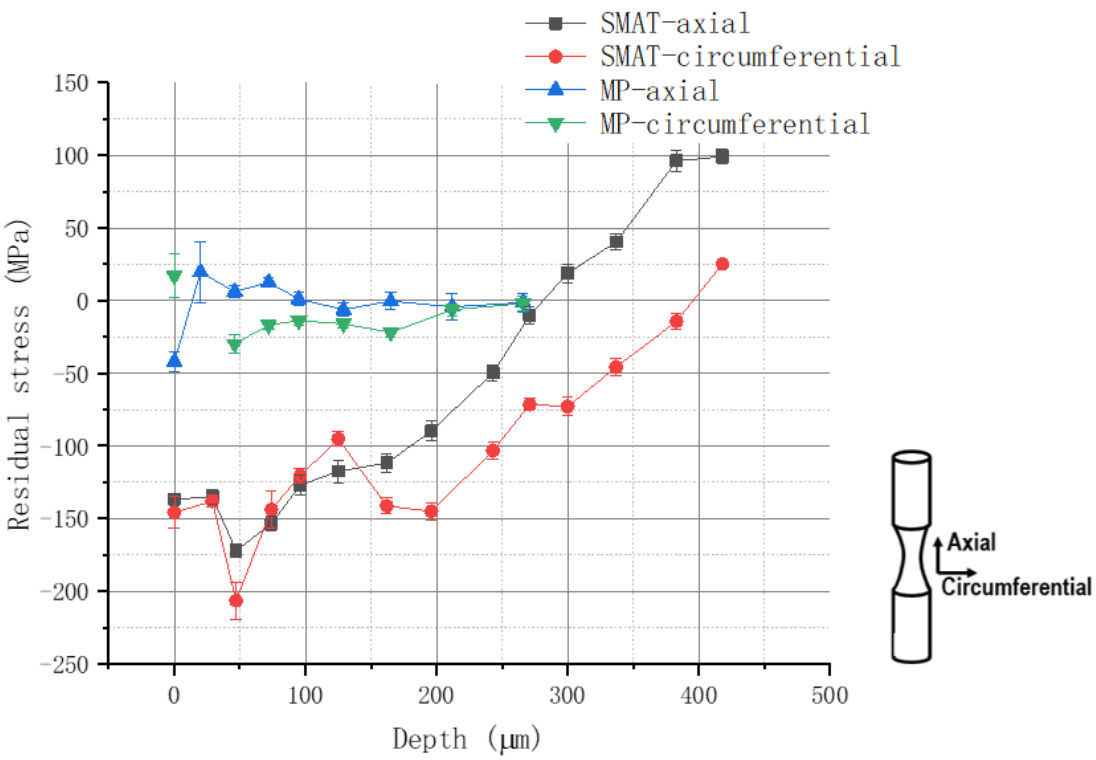

Figure 4-15. Profile distribution of SMAT-RS and MP-RS

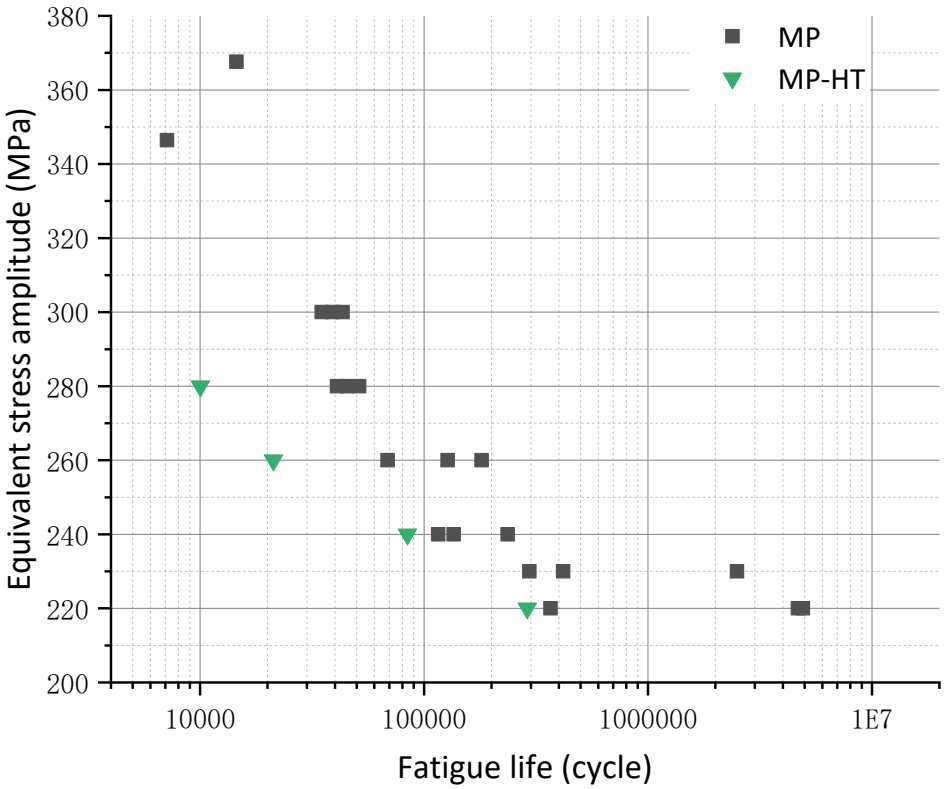

Figure 4-16. S-N plots of MP-HT tests compared with MP state

As previously demonstrated in section 4.1, annealing is an effective method for eliminating residual stresses induced by SMAT. Therefore, it can be concluded that the

MP-RS can also be removed in a similar manner. Consequently, a post-MP annealing process was applied to three specimens, which were subsequently subjected to biaxial fatigue tests. The results of these tests were recorded and are plotted in Figure 4-16, with the MP state results for comparison. MP-HT specimens are fatigue tested at 280 MPa, 260 MPa, 240 MPa and 220 MPa. The fatigue life of the MP-HT specimen is found to be significantly reduced compared with the MP specimens when tested at 260 MPa. Following the removal of the MP-RS, the fatigue life of the MP-HT specimens is observed to decrease by approximately 70% to 80%. In contrast, the reduction in fatigue life is found to be less pronounced when the MP-HT specimen is tested at 240 MPa. The reduction in fatigue lifetime is particularly pronounced at the lowest level of 220 MPa, with the MP-HT specimen exhibiting a fatigue life that is less than 10% of that of the MP specimens. In general, there is a considerable reduction in fatigue life when comparing the MP-HT state with the MP state. The reduction in fatigue life shown in Figure 4-16 helps to confirm the effect of MP-RS, which enhances the fatigue strength of MP specimens. Without such an enhancement, the MP specimens should not exhibit comparable or even higher fatigue strength compared with the SMAT state. As illustrated in Figure 4-17, the MP-HT tests are plotted with the data points of SMAT and SMAT-EP. At all the three load levels, the MP-HT specimens have the shortest fatigue life among the three states. For a stress of 260 MPa, the fatigue life of the MP-HT specimens is approximately 20% of that of the SMAT specimens and only 15% of that of the SMAT-EP specimens. For a stress of 240 MPa, the difference remains and becomes more pronounced between the MP-HT and SMAT-EP specimens. The observed phenomenon suggests that SMAT has the ability to increase the fatigue strength of raw materials, and that the duplex treatment of SMAT-EP has an additional beneficial effect.

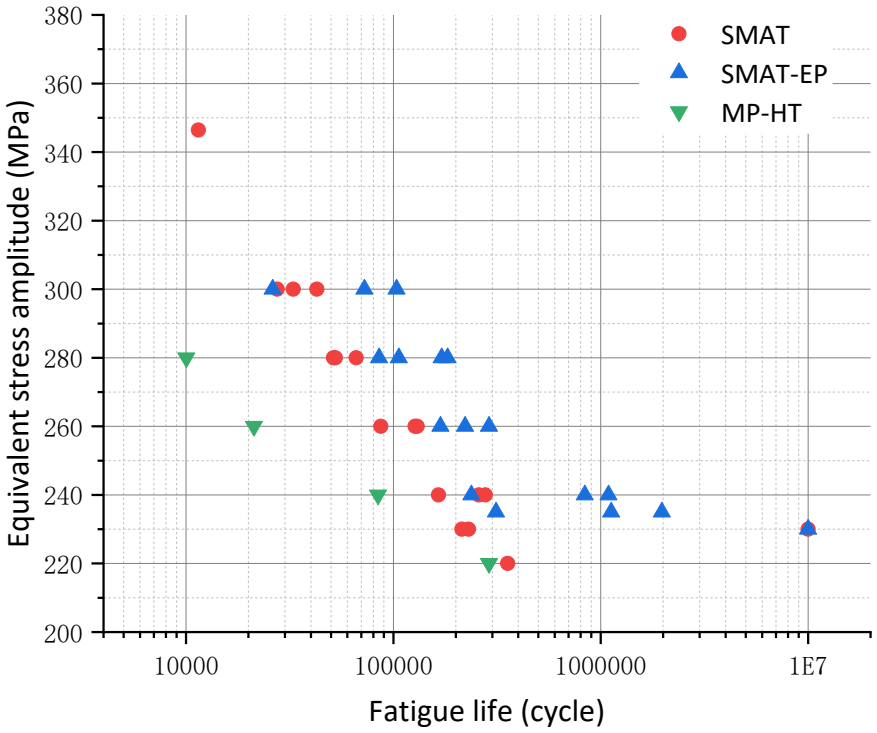

Figure 4-17. S-N plots of specimens in SMAT, SMAT-EP and MP-HT states

Furthermore, the effect of grain refinement can be re-examined using the MP-HT results. As illustrated in Figure 4-18, when compared with the MP-HT state, the SMAT-EP-HT state exhibits a slightly longer fatigue life from a relatively high load level to a low level. Since the MP-RS is completely absent in the MP-HT state, such a comparison focuses solely on the effect of grain refinement. The observed increase in fatigue lifetime indicates the potential enhancement brought about by grain refinement induced by SMAT, which has been reported in the literature [155].

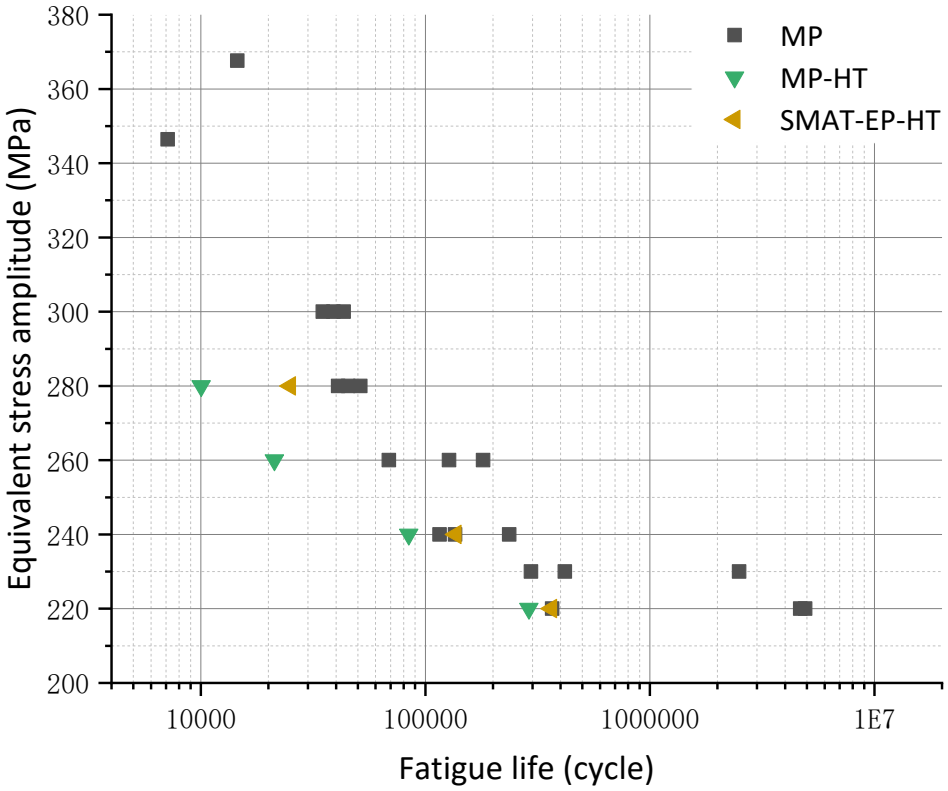

Figure 4-18. Comparison in S-N plots between MP, MP-HT and SMAT-EP-HT states

4.5 Conclusion

This chapter presents a qualitative and quantitative analysis of the factors contributing to the effect of SMAT on fatigue strength. These factors include surface integrity, SMAT-induced residual stresses, grain refinement and MP-induced residual stresses. Each factor is investigated individually through fatigue tests coupled with a specially designed post-SMAT treatment.

Electropolishing is used to remove a certain thickness of surface material so that the surface quality can be significantly improved. The fatigue strength of SMAT-EP specimens is found to be significantly higher than that of MP and SMAT states. This indicates that the increase in surface roughness and defects induced by SMAT is the main detrimental factor for fatigue strength compared with the MP state.

The relaxation of residual stress is investigated quantitatively. The residual stresses introduced by SMAT are found to be relaxed at the early stage of cyclic loadings and the relaxation lasts for no more than 35% of the total lifetime. The proportion of the

residual stress that is relaxed depends on the load level. For specimens tested at 300 MPa and 240 MPa, 52 % and 72 % of the initial residual stress can remain after the relaxation.

A 9-hour post-SMAT annealing at 185 °C is confirmed to be able of removing the residual stress and work hardening induced by SMAT. The results of fatigue tests with SMAT-HT specimens demonstrate that residual stress and work hardening significantly enhance the fatigue resistance of AA7075.

Similarly, annealing is applied to MP specimens to eliminate MP-induced residual stresses. The beneficial effect of the -50 MPa superficial MP-induced compressive residual stress is confirmed by comparing the fatigue test results of the MP state and MP-HT.

The combination of post-SMAT electropolishing and post-SMAT annealing was used to verify the effect of grain refinement. The increase in fatigue lifetime of SMAT-EP-HT specimens compared with MP-HT specimens indicates that grain refinement helps to improve the fatigue resistance.

In conclusion, the existence of both detrimental and beneficial factors and their competition determine the effect of SMAT on biaxial fatigue strength of AA7075, which is a rather complex phenomenon.

Chapter 5 Prediction on fatigue strength after SMAT with multiaxial fatigue criteria

In fatigue analysis, the prediction of fatigue strength is an integral part of the process. According to the literature, different fatigue criteria have been proposed and successfully extended to the multiaxial loading condition in the high-cycle fatigue (HCF) regime. These criteria can be categorized into two groups depending on their principle. Some criteria, such as Sines[156], are based on invariants of the stress tensor and they assume a fixed orientation of principal axes associated with a damage parameter. While some criteria, such as Fatemi-Socie[147], are based on the identification of a critical plane experiencing the maximum value of a certain damage parameter.

The objective of this section is to predict the fatigue strength of both mechanically-polished and SMATed AA7075 with different fatigue criteria, with the aim of identifying the most suitable criterion. To this end, four multiaxial fatigue criteria, which have been proven suitable for multiaxial fatigue from the literature survey, are considered: Crossland[157], Dang van[158], Findley[159] and Fatemi-Socie.

5.1 Multiaxial fatigue criteria

5.1.1 Crossland criterion

The Crossland criterion postulates that the risk of crack nucleation is proportional to a linear combination of the maximum amplitude of the second invariant of the stress deviator and the maximum value of the hydrostatic pressure during a complete cyclic loading cycle. This relationship is expressed as:

$$\xi_a + \alpha_c \cdot P_{max} = \beta_c \qquad (5-1)$$

Where the ξa is the maximum amplitude of the second invariant of the stress deviator $\sqrt{J2}$, $P_{max}$is the maximum hydrostatic pressure within a loading cycle. α_c and β_c are material constants to be determined using fatigue testing data.

5.1.2 Dang Van's criterion

The Dang Van criterion is based on a two-scale approach, in which the fatigue crack is considered to initiate at the grain level in the so-called persistent slip bands (PSB) due to alternating shear stresses. The tensile micro-scale hydrostatic stress helps open the crack and accelerate its growth along the PSB. The Dang Van criterion is postulated in the micro-scale as:

$$\tau(t) + a\sigma_h(t) = b \qquad (5-2)$$

5.1.3 Findley criterion

The Findley criterion is a criterion based on critical plane theory. It involves the maximum shear stress and normal stress acting on a material plane.

$$(\tau_a + \alpha_F \cdot \sigma_n)_{max,\theta} = \beta_F \qquad (5-3)$$

Where τ_a and σ_n are the shear and normal stress acting on the critical plane respectively. The critical plane is identified as the plane where the linear combination $(\tau_a + \alpha \cdot \sigma_n)$ experiences the maximum range during a loading cycle. α_F and β_F are material parameters.

5.1.4 Fatemi-Socie criterion

The Fatemi-Socie criterion has an expression as:

$$\left[\gamma_a \left(1 + \alpha_{FS} \cdot \frac{\sigma_n}{\sigma_Y}\right)\right]_{max,\theta} = \beta_{FS} \qquad (5-4)$$

Where γ_a is the shear strain amplitude on the critical plane, and σ_n is the normal stress acting on this plane. Similar to that of Findley criterion, the critical plane is identified as the plane experiencing the maximum value of the damage parameter $\gamma_a \left(1 + \alpha \cdot \frac{\sigma_n}{\sigma Y}\right)$. α_{FS} and β_{FS} are material parameters, and σ_Y is the yield stress of the base material.

5.2 Determination of material parameters

The application of a fatigue criterion typically comprises two steps: the

determination of material parameters and the calculation of predicted fatigue strength. This section presents the process of determining the material parameters.

Fatigue data obtained from tests with relatively simple load paths is often used for calculating the material parameters. Such tests include uniaxial tension-compression tests, pure torsional tests, bending tests, and so forth. In this work, such data is obtained from former research on AA7075[1,130]. As illustrated in Figure 5-1, the results of fully reversed tension-compression (a) and torsional tests (b) are employed to calculate the fatigue limit at fatigue lives spanning from 10^4 to 10^6 cycles.

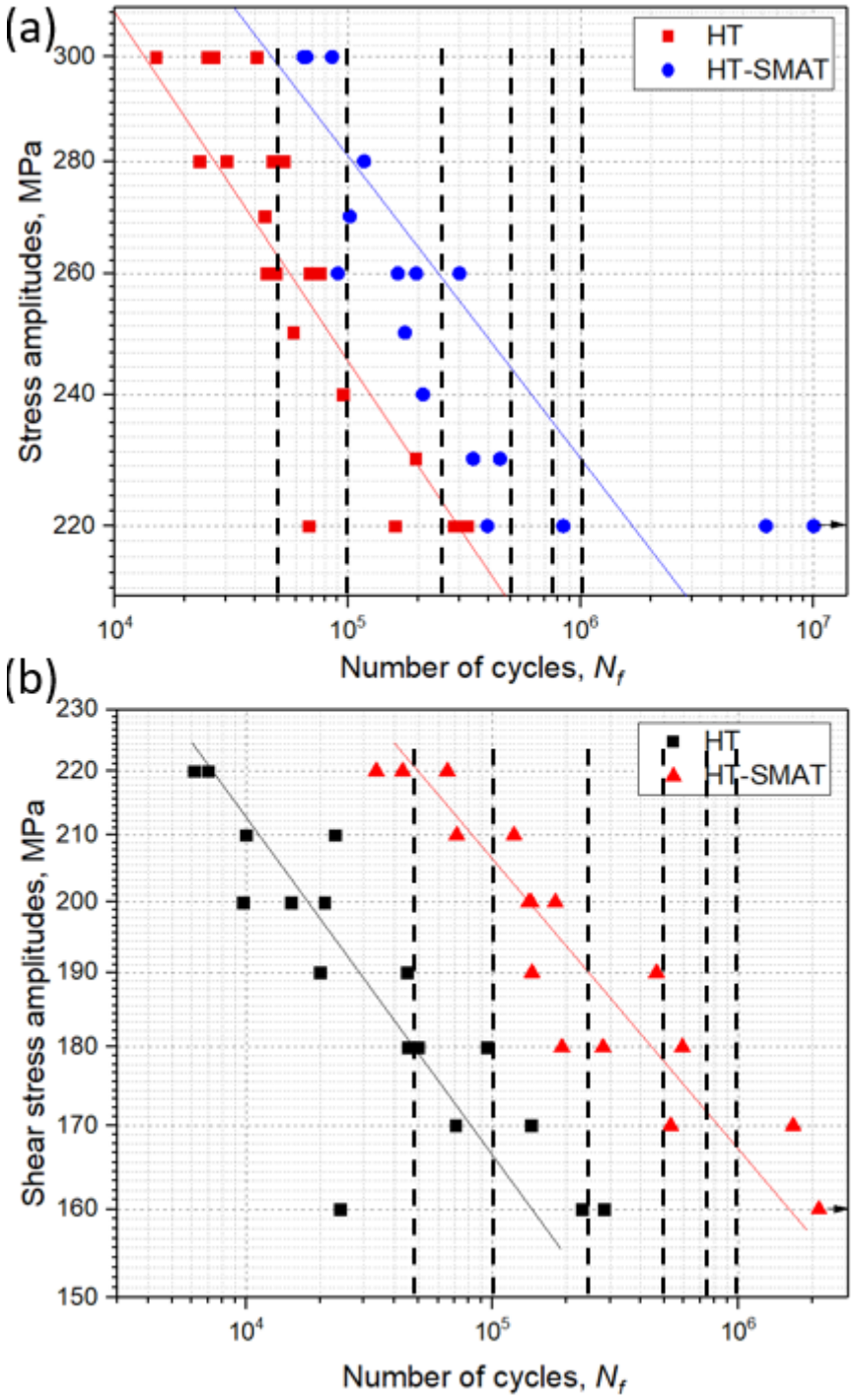

Figure 5-1. S-N curve of both base and SMATed AA7075 obtained from (a) tension-compression tests and (b) torsional tests[1]**.**

5.2.1 Crossland criterion

For the Crossland criterion, the parameter β_c equals to the torsional fatigue limit τ_t, since the hydrostatic pressure P_{max} equals to 0, in the case of pure torsion.

$$\xi_a = \tau_f = \beta_C \qquad (5-5)$$

While in the case of tension-compression, the equation (5-1) can be rewritten as:

$$\sigma_f/\sqrt{3} + \alpha_C \cdot \sigma_f/3 = \beta_C \qquad (5-6)$$

Where σ_f is the fatigue limit obtained from fully reversed tension-compression tests. Therefore, the solution of material parameters α_c and β_c can be easily obtained by combining equation (5-5) and (5-6) together.

$$\alpha_C = \frac{\tau_f - \sigma_f/\sqrt{3}}{\sigma_f/3} \qquad (5-7)$$

$$\beta_C = \tau_f \qquad (5-8)$$

5.2.2 Findley and Fatemi-Socie criteria

A criterion based on critical plane theory may present a more complex parameter-determining process. This section presents the Findley criterion as an example, detailing the process in detail, including confirming the solution of material parameters and identifying the critical plane.

For a material tested with fully reversed tension-compression loads, the stress state on a material plane θ can be expressed as:

$$\sigma = \sigma_a \cdot cos^2\,\theta\, sin\,\omega t$$

$$\tau = \sigma_a \cdot sin\theta cos\theta \sin \omega t$$

Where σ_a is the stress amplitude and θ is the angle between the material plane and the axial direction of the specimen, as illustrated in Figure 5-2.

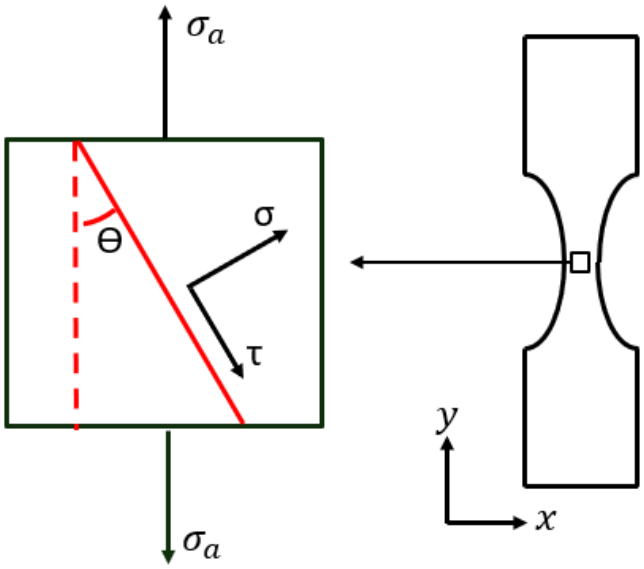

Figure 5-2. Schematic of stress state in tension-compression tests

Since the shear and normal stress acting on the material plane are at their maximum value simultaneously, the maximum value of the stress state can be expressed as follows:

$$\sigma = \sigma_a \cdot cos^2\,\theta \qquad (5-9)$$

$$\tau = \sigma_a \cdot sin\theta cos\theta \qquad (5-10)$$

Thus, the equation (5-2) can be rewritten with (5-9) and (5-10) as:

$$\tau_a + \alpha_F \cdot \sigma_n = \sigma_f(sin\,\theta\,cos\,\theta + \alpha_F \cdot cos^2\,\theta) = \beta_F \qquad (5-11)$$

Where σ_f is the fatigue limit at a certain fatigue life. To identify the critical plane, it is necessary to confirm the solution of the angle θ. Considering the left part of the equation (5-11) as a function of θ:

$$g(\theta) = \sigma_f(sin\,\theta\,cos\,\theta + \alpha_F \cdot cos^2\,\theta) \qquad (5-12)$$

Due to the existence of an extreme value of the function (5-12), the derivative has to equal to 0 at the extremum point:

$$\frac{dg}{d\theta} = cos^2\theta - sin^2\theta - 2\alpha_F \cdot sin\theta cos\theta = cos2\theta - \alpha_F \cdot sin2\theta = 0 \qquad (5-13)$$

Hence, the solution of the angle θ of the critical plane is given:

$$tan2\theta = \frac{1}{\alpha_F} \qquad (5-14)$$

The equation (5-11) can be rewritten with (5-14) as:

$$\sigma_f \cdot (sin\,\theta\,cos\,\theta + \alpha \cdot cos^2\,\theta) = \sigma_f \cdot cos^2\,\theta \cdot (tan\,\theta + \alpha) = \beta_F \qquad (5-15)$$

Some trigonometric identities can be useful here:

$$tan\,\theta = \frac{tan\,2\theta}{1+\sqrt{1+tan^2\,2\theta}} = \frac{1}{\alpha_F + \sqrt{1+{\alpha_F}^2}}$$

$$cos^2\,\theta = \frac{1}{1+tan^2\,\theta} = \frac{\left(\alpha_F + \sqrt{1+{\alpha_F}^2}\right)^2}{1+\left(\alpha_F + \sqrt{1+{\alpha_F}^2}\right)^2}$$

Using these two identities, the equation (5-14) can be rewritten as:

$$\beta_F = \frac{\sigma_f}{2} \cdot \left(\alpha_F + \sqrt{1+{\alpha_F}^2}\right) \qquad (5-16)$$

For material tested with reversed torsional loading, similar process should be done by repeating the calculation from equation (5-9) to equation (5-16). The solution of the angle of the critical plane can be obtained:

$$tan\,2\theta = -\alpha_F \qquad (5-17)$$

As well as the relation between β_F and α_F:

$$\beta_F = \tau_f \cdot \sqrt{1+{\alpha_F}^2} \qquad (5-18)$$

Where τ_f is the torsional fatigue limit at certain fatigue life. For both equation (5-16) and (5-18), the parameter β_F should be the same, thus an equality can be obtained:

$$\beta_F = \frac{\sigma_f}{2} \cdot \left(\alpha_F + \sqrt{1+\alpha_F^2}\right) = \tau_f \cdot \sqrt{1+\alpha_F^2} \qquad (5-19)$$

Since the fatigue limits of both tension-compression and torsion tests are known, the value of α_F can be confirmed by solving the equality (5-19). Once α_F is confirmed, β_F can be easily calculated through (5-16) or (5-18).

The Fatemi-Socie criterion is also based on the critical plane theory, thus the parameter-determining process is similar to that of Findley criterion.

Considering the range of fatigue lives in tension-compression and torsion tests, 6 fatigue lives are selected: 5×10^4, 10^5, 2.5×10^5, 5×10^5, 7.5×10^5 and 10^6 cycles, as illustrated with black dash lines in Figure 5-1. The material parameters of the three criteria mentioned above are calculated at these 6 fatigue lives. The parameters are listed in Table 5-1.

Table 5-1. Material parameter of 3 fatigue criteria at different fatigue lives

Fatigue life	5×10^4	10^5	2.5×10^5	5×10^5	7.5×10^5	10^6
Crosslan d-α_C	0.31	0.317	0.327	0.334	0.338	0.341
Crosslan d-β_C	179	167.6	153.7	143.9	138.4	134.7
Findley-α_F	0.387	0.393	0.402	0.408	0.411	0.414
Findley-β_F	191.96	180.09	165.65	155.41	149.61	145.77
Fatemi-Socie-α_{FS}	1.211	1.315	1.469	1.595	1.670	1.730
Fatemi-Socie-β_{FS}	0.0066 5	0.0062 3	0.0057 1	0.0053 5	0.0051 4	0.0050 1

5.3 Results and comparison

The results of section 5.2 allow for the prediction of the fatigue strength of MP, SMAT and SMAT-EP specimens. However, it should be noted that several assumptions have been made:

1) The material parameters for each fatigue criterion are related to the nature of the material. Therefore, it is assumed that the parameters are the same for SMATed material and base material;
2) The surficial material is of primary consideration in both the MP and SMATed states, as the majority of cracking sources are located on the surface rather than within the bulk material;
3) The residual stresses are imposed as static compressive stresses σ_R, thus the stress state for a SMATed material is assumed to be a plane stress state, as shown in Figure 5-3;
4) In the calculation, both the initial and the stabilized value of residual stresses are employed. The stabilized residual stress value is assumed to be a function of the

stress amplitude applied to the material, and thus it is obtained by linear fitting.

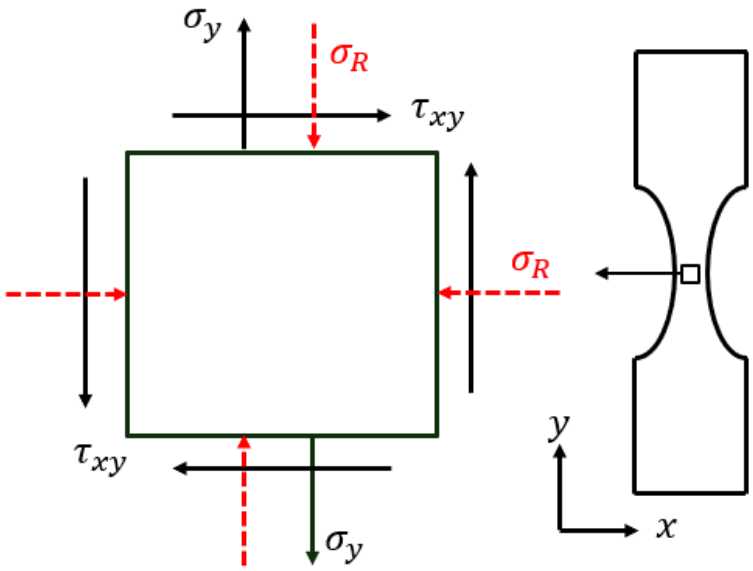

Figure 5-3. Schematic of the plane stress state of SMATed surficial material

In accordance with the aforementioned assumptions, the predicted fatigue strength can be calculated.

5.3.1 Prediction with Crossland criterion

Based on the stress state illustrated in Figure 5-3, the equation (5-1) can be written as:

$$\sqrt{\frac{1}{6}\left[\sigma_R^2 + \left(\sigma_R + \sigma_y\right)^2 + \sigma_y^2 + 6\tau_{xy}^2\right]} + \alpha_C \cdot \frac{1}{3}\left(\sigma_y + 2\sigma_R\right) = \rho_C \qquad (5-20)$$

It should be noticed that the ratio between axial and torsional loads is set as $\sqrt{3}$ for all the biaxial fatigue tests. Therefore, the left part of the equality (5-20) can be seen as a function of the applied load σ_y. The function can be used to calculate the value of σ_y, which is the predicted fatigue strength. When σ_R equals to 0, the non-SMAT surface condition can also be considered using the same method. The results calculated with Crossland criterion are shown below in Figure 5-4, 5-5 and 5-6.

In the case of the MP condition (Figure 5-4), the fatigue strength predicted by the Crossland criterion (red circles) demonstrates a high degree of predictive capability in comparison with the experimental data (black squares). However, a slight underestimation can be observed between the experimental and predicted fatigue

strength at relatively high loading levels, such as 5×10^4cycle. Conversely, at medium and relatively low loading levels, the difference between the experimental and predicted fatigue strength is minimal.

For SMAT specimens (Figure 5-5), the prediction of fatigue strength is made using two values of residual stresses induced by SMAT. As indicated by the red circles, the fatigue strength predicted using initial residual stresses showed significant errors in comparison with the experimental data. Overestimation was observed to be non-negligible for both high and low loading levels. When calculating with stabilized residual stresses, the accuracy of prediction (blue triangles) increased significantly. The discrepancy between the predicted and actual fatigue strength decreases from approximately 30% to 15% when initial residual stresses are replaced with stabilized residual stresses. While underestimation persists, this improvement demonstrates that the accuracy of prediction is contingent upon the calculation of stress states. For SMATed materials, fatigue crack behavior is primarily observed during long-term cyclic loadings, rather than the initial few loading cycles where the majority of residual stress relaxation occurs.

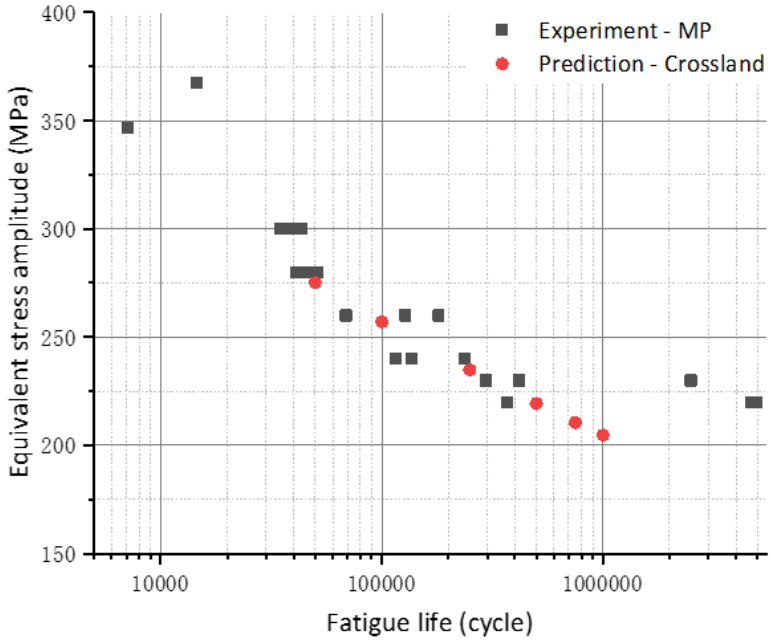

Figure 5-4. Comparison between predicted fatigue strength and experimental data of MP specimens

In the case of SMAT-EP specimens, the prediction is made using a stabilized value of

residual stresses. As illustrated in Figure 5-6, although overestimation persists, the discrepancy between the predicted fatigue strength and the experimental data is significantly reduced in comparison to that of the SMAT state. The error is approximately 10% to 15%.

In general, the Crossland criterion demonstrates satisfactory predictive capacity when applied to MP AA7075, while distinct overestimation of fatigue strength can be observed in the SMATed state. It can be postulated that the post-SMAT electropolishing process may serve to reduce the error of prediction, which may indicate that the effect of surface roughness is non-negligible in fatigue strength prediction.

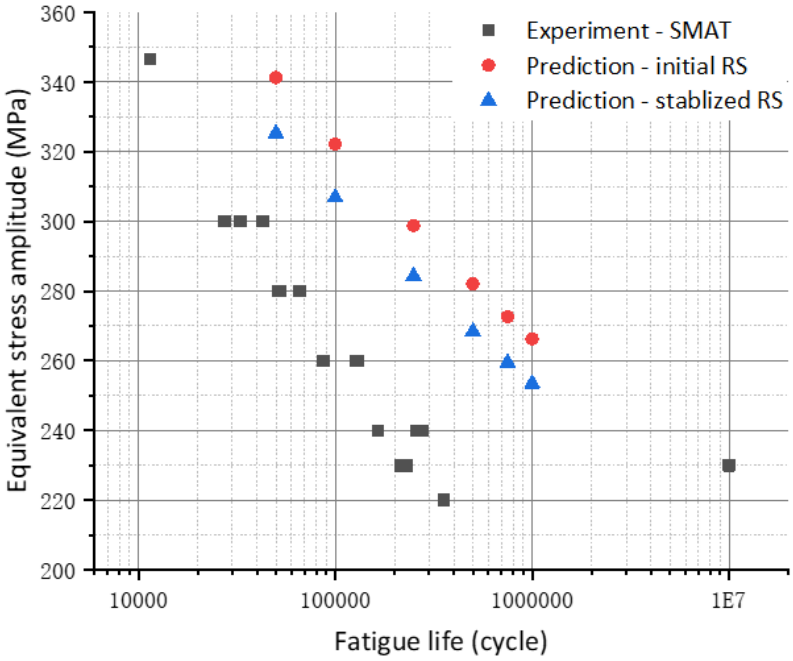

Figure 5-5. Prediction on fatigue strength of SMATed AA7075

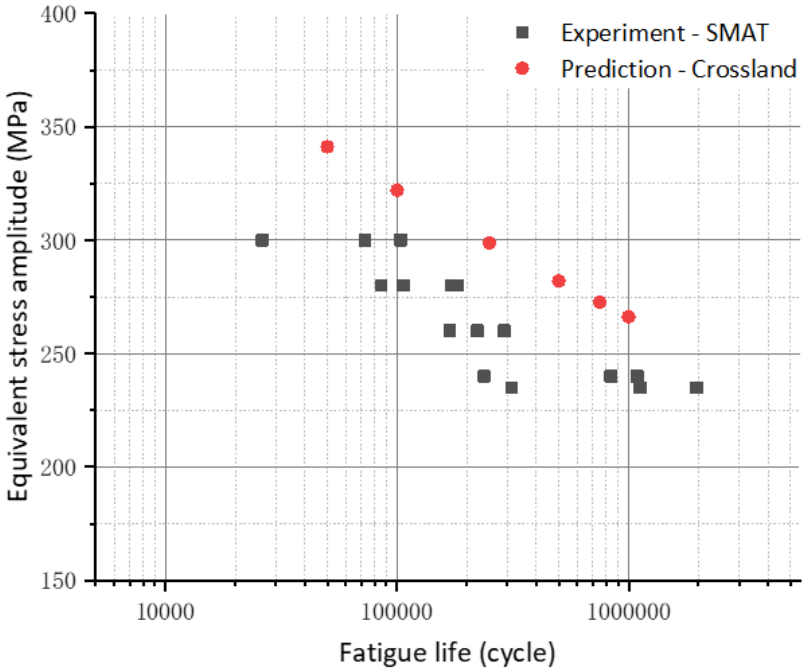

Figure 5-6. Prediction on fatigue strength of SMAT-EP AA7075 with stabilized value of residual stresses

5.3.2 Prediction with Findley and Fatemi-Socie criteria

The calculation of fatigue strength predicted with critical-plane criteria is a more complex process than that described in the previous section. This section presents the process using the Findley criterion as an example.

According to the stress state shown in Figure 5-3, the equation of Findley criterion can be rewritten as:

$$\left\{-\frac{\sigma_y}{2}sin2\theta+\tau_{xy}cos2\theta+\alpha_F\cdot(\sigma_R+\frac{\sigma_y}{2}-\frac{\sigma_y}{2}cos2\theta-\tau_{xy}sin2\theta)\right\}max,\theta=\beta_F(5-21)$$

To solve the equality, it is necessary to determine the critical plane firstly. The left part of the equation (5-21) can be seen as a function of the applied load σ_y and the material plane angle θ:

$$m(\sigma_y,\theta)=\left(-\frac{1}{2}sin2\theta+\frac{1}{\sqrt{3}}cos2\theta+\frac{\alpha_F}{2}-\frac{\alpha_F}{2}cos2\theta-\frac{\alpha_F}{\sqrt{3}}sin2\theta\right)\sigma_y+\alpha_F\sigma_R(5-22)$$

It is obvious that when the linear combination of $\left(-\frac{1}{2}sin2\theta+\frac{1}{\sqrt{3}}cos2\theta+\frac{\alpha_F}{2}-\frac{\alpha_F}{2}cos2\theta-\frac{\alpha_F}{\sqrt{3}}sin2\theta\right)$ reaches its maximum value, the predicted value of σ_y can be calculated. The value of θ varies within the range of the selected fatigue lives, though

the difference is not negligible in the present work.

The calculation process of the Fatemi-Socie criterion is analogous to that of the Findley criterion. The outcomes of all three aforementioned criteria are presented in Figures 5-7. With regard to the MP state, all three criteria demonstrate an acceptable degree of accuracy in their predictions. The Crossland criterion provides the most accurate prediction with the least amount of error. In contrast, for both SMAT and SMAT-EP states, the three criteria exhibit significant overestimation, and the errors of prediction on SMAT state are too large to be acceptable. Furthermore, for all fatigue lives within the range of 5×10^4-10^6 cycles, the difference between the various criteria is negligible.

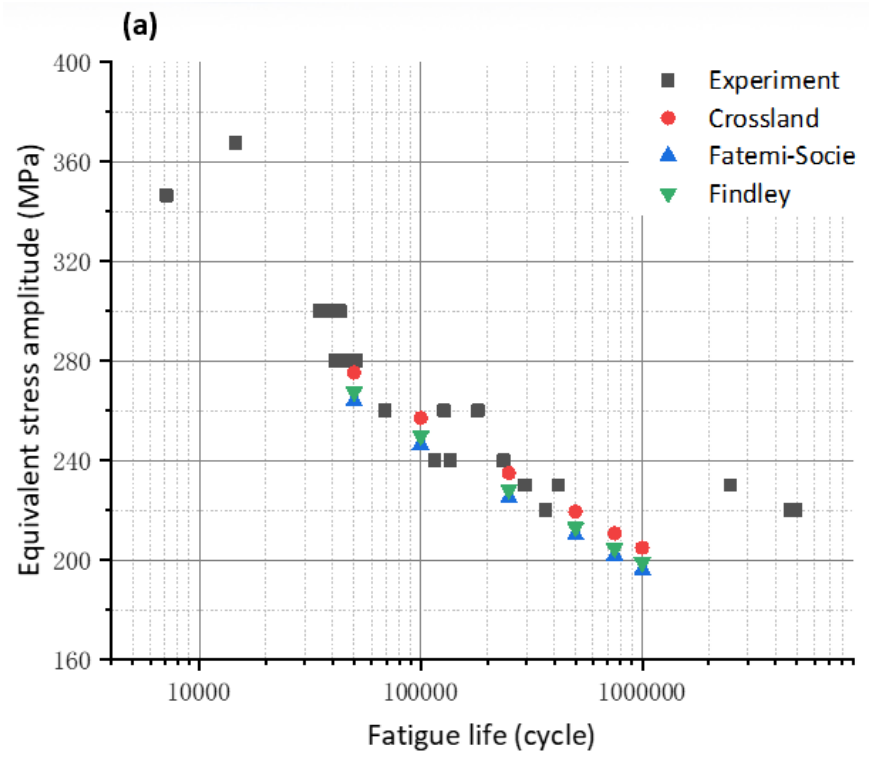

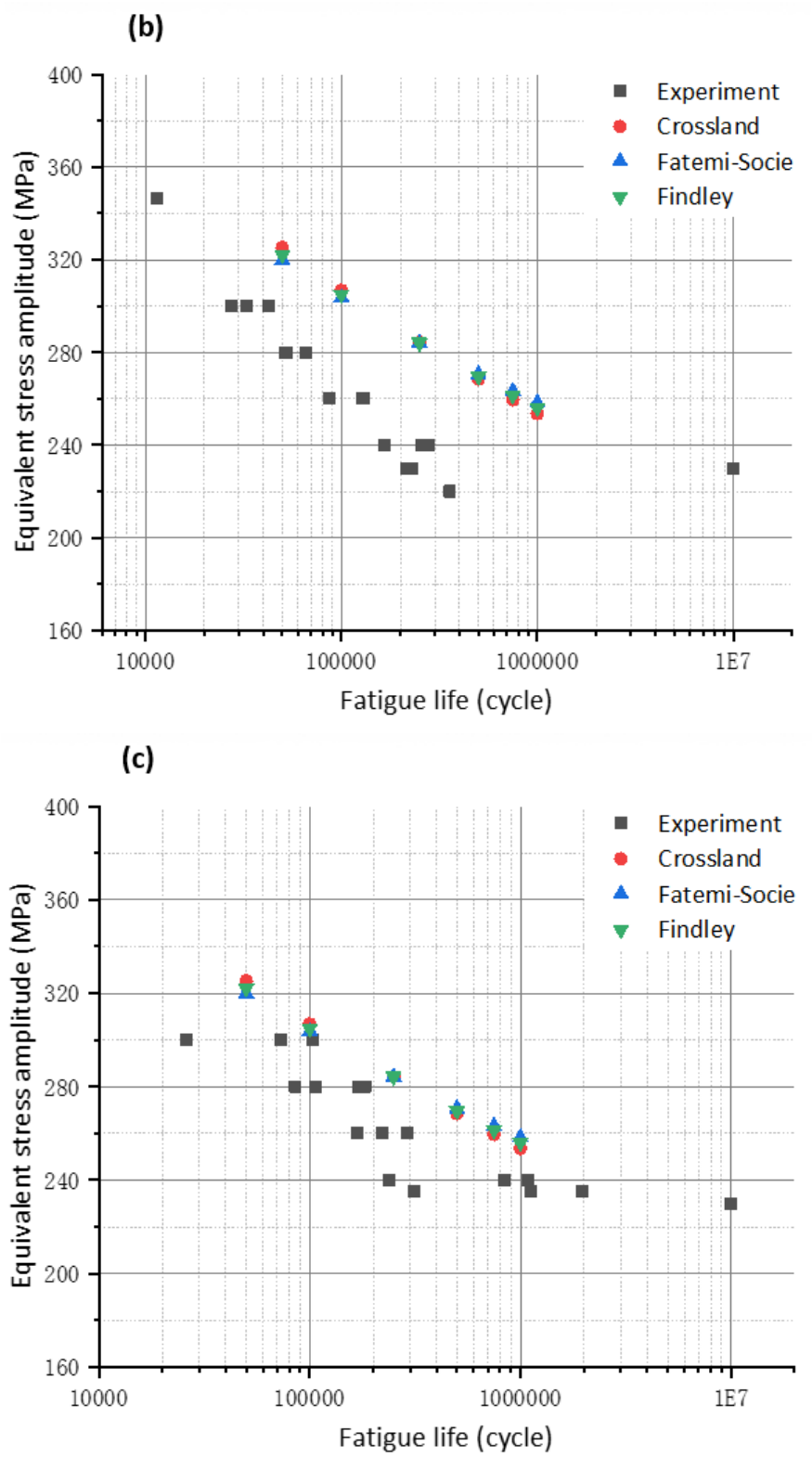

Figure 5-7. S-N slot of experimental and predicted data from (a) MP state tests, (b) SMAT state tests and (c) SMAT-EP state tests.

5.4 Discussion and improvement on predictions

As demonstrated in Section 5.3, the predictions generated using three fatigue criteria exhibit a notable overestimation for both SMAT and SMAT-EP specimens, rendering the prediction unreliable. In addition to the precision of fitting the results of tension-compression and torsional tests, other factors can be considered to reduce the error of prediction.

5.4.1 Effect of surface roughness

As previously discussed in section 2.3.1, the surface undergoes a significant transformation following SMAT, exhibiting pronounced plastically deformed characteristics. The value of the SMATed surface roughness is markedly elevated in comparison to that of the MP state. Consequently, the surface roughness may exert a non-negligible influence on the precision of prediction. Various methodologies have been implemented to account for the impact of surface roughness following surface treatment. According to the research on shot-peened material[160], a factor of stress concentration can be introduced:

$$K_t = 1 + 4\left(\frac{R_t}{D}\right)^{1.3} \qquad (5-23)$$

Where K_t is the stress concentration factor, R_t is the peak-valley value in surface roughness measurement, and D is the average space of dimples on the surface of SMATed material. Considering that the shape of the dimples induced by SMAT is basically round or elliptic, the diameter (or the mean value of major and minor axis $(a + b)/2$) is taken as the parameter D here, as illustrated in Figure 5-8.

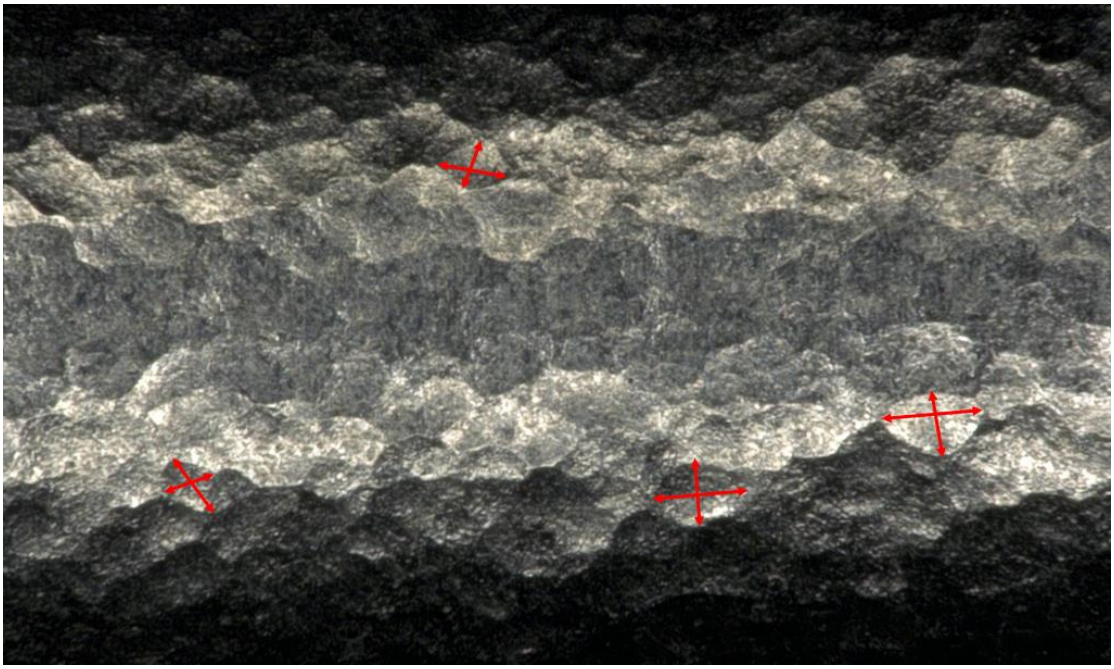

Figure 5-8. Measurement of average space of dimples on a SMATed surface

The prediction of fatigue strength with three criteria can be calibrated using the factor K_t. When this factor is taken into consideration, the prediction is presented in Figure 5-9. It can be observed that the error of prediction on fatigue strength for the SMAT state has decreased significantly. Overestimation is no longer observed for fatigue lives less than 10^5 cycles. Slight overestimation is present for fatigue lives greater than 5×10^5 cycles. The discrepancy between the predicted and experimental values has been reduced from over 20% to less than 10%. Consequently, the calibration with K_t can be regarded as an effective method for enhancing the precision of the prediction.

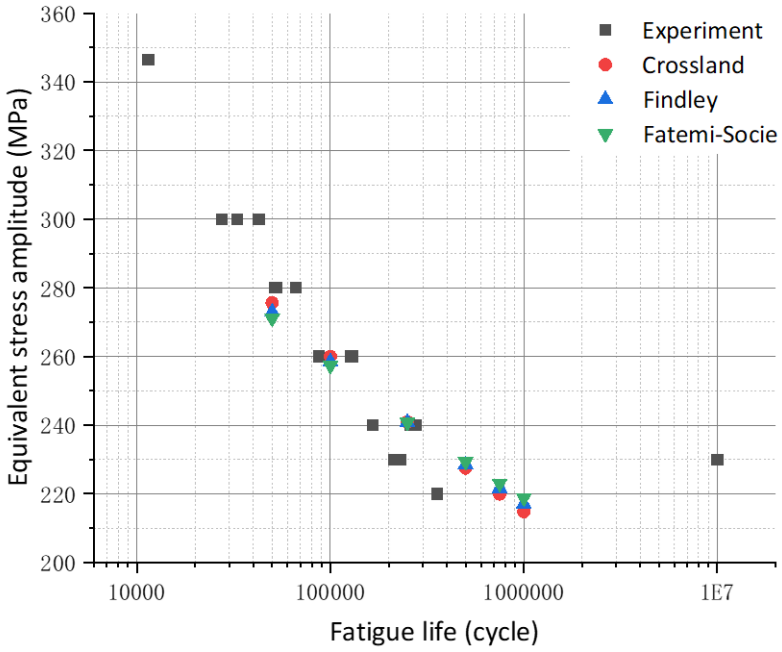

Figure 5-9. Prediction on fatigue strength calibrated using factor K_t

5.4.2 Effect of in-depth distribution of residual stresses

Another potential contributing factor to the inaccuracy of the prediction could be the nonuniformity of residual stresses. As previously discussed in Chapter 2, the residual stresses induced by SMAT exhibit a notable decrease along the radial direction. The compressive residual stresses are expected to disappear at a depth of approximately 300 µm, while the tensile residual stresses are believed to persist below this depth. It is therefore important to note that for the prediction of fatigue strength at relatively long fatigue lives, the possibility of interior crack initiation cannot be ignored.

5.4 Conclusion

In this chapter, the fatigue strength of AA7075 with different surface conditions is predicted using the Crossland, Findley and Fatemi-Socie criteria. The fatigue strength is predicted at 5×10^4, 10^5, 2.5×10^5, 5×10^5, 7.5×10^5 and 10^6 cycles. The results indicate that the Crossland criterion provides the most accurate prediction for the MP state, while all three criteria overestimate the fatigue strength for the SMAT and SMAT-EP

states. The prediction for the SMAT state exhibits the greatest discrepancy compared to the other two states. The error in the prediction for the SMAT state can be significantly reduced by incorporating a stress concentration factor K_t, which can account for the effect of surface roughness.

Chapter 6 Conclusions and prospects

6.1 Conclusions

Surface Mechanical Attrition Treatment is a promising technique capable of improving the mechanical properties of metallic materials, including the fatigue properties in both low cycle and high cycle regimes. However, the effect of SMAT on fatigue properties under complex loadings remains to be explored. The aim of the present work is to investigate the effect of SMAT on the fatigue properties of an aluminum alloy 7075 tested under combined tension-torsion loadings.

A brief literature review of the background of this work is presented in Chapter 1, including the basic elements of SMAT, the effect of SMAT on the fatigue properties of metallic materials, basic information of the studied material 7075 Aluminum Alloy and a brief review of multiaxial fatigue. SMAT is reported to be capable of introducing grain refinement, compressive residual stresses (CRS) and work hardening layer on the surface of variant treated materials, such as aluminum, titanium and stainless steels. Such modifications contribute to the enhancement of mechanical properties, including surface hardness, tensile strength, and corrosion resistance. The information of the material – AA7075 is also presented, along with the background of multiaxial fatigue.

In Chapter 2, pre-SMAT processes including mechanical polishing and heat treatment are first introduced. The SMAT process conducted on the AA7075 specimens is then illustrated, and the results of Post-SMAT characterizations such as hardness measurement and roughness measurement are presented. Compressive residual stresses and profiles are measured using X-ray diffraction and the electropolishing method. A compressive stress layer with a thickness of approximately 350μm and a peak value of -200 MPa is found on the SMATed AA7075 specimens.

The results of combined tension-torsion fatigue tests on AA7075 specimens in both mechanically-polished (MP) and SMAT surface states are presented and discussed in

Chapter 3. The S-N plots, Basquin equation and the fitted P-S-N curves all reveal a minimal difference in fatigue strength between MP and SMAT specimens. Fractographic observations show that MP specimens exhibit surface shear cracking and tensile cracking behaviors at high and low load levels respectively, while SMAT specimens primarily show shear cracking. The decrease in steady growth period (Stage II) area indicates that the crack growth could be accelerated due to the deteriorated surface integrity.

To explain the minimal difference in fatigue strength between MP and SMAT specimens, an investigation on the factors contributing to the effect of SMAT is presented in Chapter 4. The factors are examined individually, including surface integrity, the compressive residual stress layer, and grain refinement. Specially-designed experiments with different post-SMAT processes are conducted. Post SMAT electropolishing is applied to remove a 15 μm surface layer, which helps eliminate the influence of the deteriorated surface integrity. The SMAT-EP specimens exhibit significantly longer fatigue lives at all load levels, compared to specimens in MP and SMAT states, indicating that the deteriorated surface integrity is the main detrimental factor induced by SMAT. The relaxation of CRS is measured and analyzed through interrupted fatigue tests. The proportion of CRS relaxed is non-negligible and depends on the load levels. Post-SMAT annealing is chosen to eliminate the influence of the CRS layer. A 9-h annealing at 185℃ is confirmed to be capable of relaxing the SMAT-induced CRS. The significant decrease in fatigue lives of SMAT and annealed specimens demonstrates the beneficial effect of CRS. The combination of post-SMAT electropolishing and annealing is applied to reveal the effect of grain refinement, and the results confirm its beneficial effect. The existence of these detrimental and beneficial factors and their competition are considered the explanation for the complex effect of SMAT on fatigue properties.

The estimation of fatigue strength of AA7075 specimens in MP, SMAT and SMAT-EP states is shown in Chapter 5. Typical multiaxial fatigue criteria, including Crossland, Dang Van's, Findley and Fatemi-Socie, are compared. The results indicate that for MP

specimens, the Crossland criterion provides the most accurate prediction with the smallest error. For both SMAT and SMAT-EP specimens, over-estimation is found at all load levels with all criteria. The accuracy of prediction could be improved if the increased surface roughness is taken into consideration with a special stress concentration factor.

6.2 Prospects

This work focuses on the effect of SMAT on the biaxial fatigue properties of AA7075. The complex effect is investigated and explained with fatigue tests and fractographic observations. Although some conclusions have been drawn based on the present results, the research on the SMAT-affected fatigue properties still needs further exploration.

The multiaxial fatigue properties of metallic materials highly depend on the loading condition such as loading paths. In the present work, only the proportional combined tension-torsion loading path is applied in the fatigue tests. Results obtained from fatigue tests with other loading paths, like non-proportion loadings with different phase angles and pulse loadings, could be different from the present results.

Another factor influencing the multiaxial fatigue properties of metallic materials is the nature of the material. As reviewed in Chapter 1, materials with different values of stacking fault energy (SFE) may exhibit totally different multiaxial fatigue behaviors, especially in the LCF regime. SMAT may have totally different effects on multiaxial fatigue properties of metallic materials with low SFE, for example stainless steels, which is obviously worth exploring.

In terms of fatigue strength estimation, only several typical multiaxial fatigue criteria are used in the present work. Some newly-developed criteria, which focus more on work hardening and residual stresses, can be tested on the SMATed materials.

Résumé en français

1. Introduction

Le traitement par attrition mécanique de surface (SMAT) est une technique de traitement de surface prometteuse pour améliorer les propriétés mécaniques des matériaux métalliques. Cette technique implique des impacts multidirectionnels à haute fréquence, qui génèrent une couche nanostructurée à la surface d'une pièce, ainsi qu'un profil de contraintes résiduelles de compression élevé et un gradient d'écrouissage dans la zone de subsurface. Il a été démontré que le SMAT peut améliorer les propriétés mécaniques, en particulier la résistance à la fatigue, de divers matériaux dans différentes conditions de chargement.

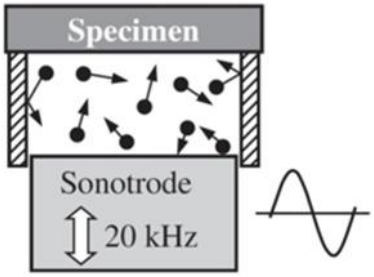

Figure 1. Schéma d'une installation SMAT

L'alliage d'aluminium 7075 (AA7075) est un matériau largement utilisé dans les industries aérospatiale et automobile. Les composants fabriqués à partir d'AA7075 sont souvent soumis à des conditions de travail complexes, telles que des charges multiaxiales. Par conséquent, les propriétés de fatigue de l'AA7075 ont fait l'objet d'une attention particulière.

L'objectif de cette étude est d'étudier les propriétés de fatigue de l'AA7075 traité par SMAT dans des conditions de chargement combinée de tension-compression/torsion.

2. Matériau et caractérisation

2.1 Processus pré-SMAT

Les matériaux AA7075 ont été usinés à partir de barres brutes en éprouvettes de fatigue en forme d'haltères dont les dimensions sont indiquées dans la figure 2. Un traitement thermique non standard a été effectué, consistant en une mise en solution de 4h 450℃ et un vieillissement de 12h 185℃, afin d'augmenter la ductilité du matériau.

Par la suite, les échantillons tels qu'usinés (AM) ont été soumis à un polissage mécanique afin d'éliminer les traces d'usinage et de réduire la rugosité.

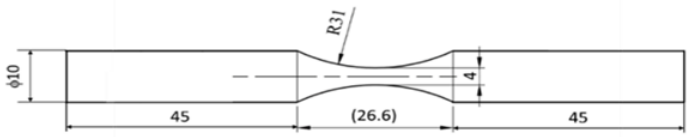

Figure 2. Dimensions de l'échantillon d'essai de fatigue AA7075.

2.2 Processus SMAT

La procédure SMAT a été réalisée à l'aide de la machine SMAT du laboratoire LASMIS UTT. Les paramètres du processus ont été déterminés en fonction des recherches antérieures menées dans le laboratoire, comme le montre le tableau 1.

Tableau 1. Paramètres du procédé SMAT

Taille du tir	Durée du SMAT	Couverture SMAT	Amplitude du signal
2mm	25min	1000%	27%

2.3 Caractérisation post-SMAT

Après le processus SMAT, le matériau AA7075 a été soumis à une caractérisation à l'aide d'une série de techniques de mesure au LASMIS UTT. Tout d'abord, la rugosité de la surface a été mesurée et est présentée dans le tableau 2.

Tableau 2. Rugosité des surfaces de différents états (μm)

État de	AM	MP	SMAT

surface			
Ra	0.5381	0.2812	0.4324
Rt	14.90	3.098	10.33

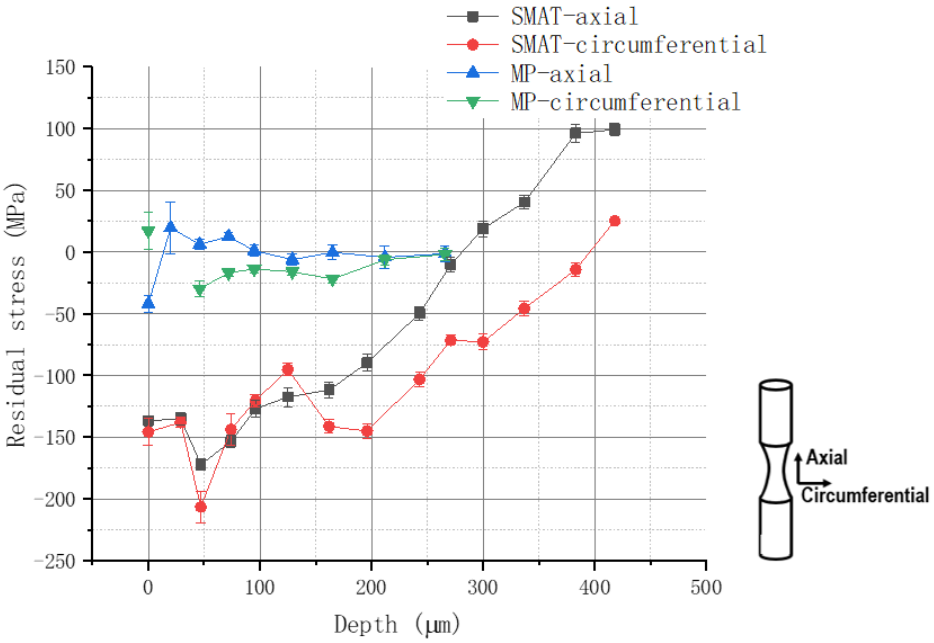

Figure 3. Profil de contrainte résiduelle des échantillons MP et SMAT.

Deuxièmement, les contraintes résiduelles induites par le SMAT ont été quantifiées à l'aide de l'appareil de diffraction des rayons X SEIFERT. Les profils de contraintes résiduelles ont été obtenus en éliminant les couches superficielles par électropolissage. Les données relatives aux contraintes résiduelles sont présentées dans la figure 4. Il a été constaté que des contraintes résiduelles de compression peuvent être générées à la surface des échantillons en AA7075 traités par SMAT sur une profondeur d'environ 350µm, et une valeur maximale de -200MPa

3. Propriétés de fatigue biaxiale après SMAT

3.1 Procédure expérimentale

Des essais de fatigue biaxiale ont été effectués sur des spécimens à l'état poli mécaniquement (MP) et à l'état SMAT. Les essais ont été réalisés à l'aide d'une machine d'essai de fatigue INSTRON au LASMIS de l'UTT. Une condition de chargement de tension-torsion proportionnelle (en phase) combinée a été sélectionnée, avec des

amplitudes de contraintes équivalentes comprises entre 220 MPa et 346 MPa. Tous les essais ont été effectués à une fréquence de 10 Hz à température ambiante.

3.2 Données S-N et ajustement P-S-N

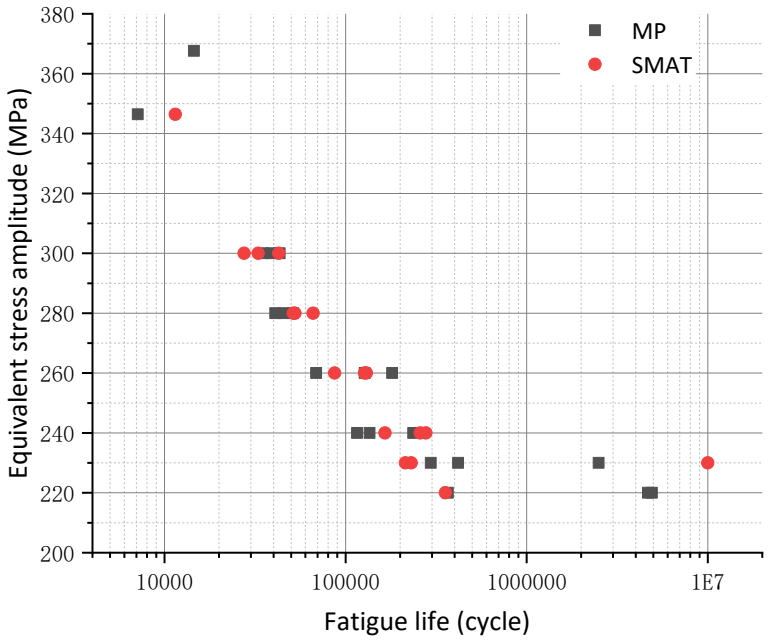

Figure 4. Diagrammes S-N des essais de fatigue pour les spécimens dans les états MP et SMAT

Les résultats des essais de fatigue biaxiale sont présentés sous forme S-N dans la figure 4. Afin de mieux comprendre la distinction entre les états MP et SMAT, l'équation de Basquin et les courbes P-S-N ont également été ajustées. Les paramètres des équations de Basquin ajustées pour les états MP et SMAT sont présentés dans le tableau 3.

Tableau 3. Paramètres de l'équation de Basquin pour les états MP et SMAT

	a	b
MP	762.717	-0.0850953
SMAT	756.004	-0.0853823

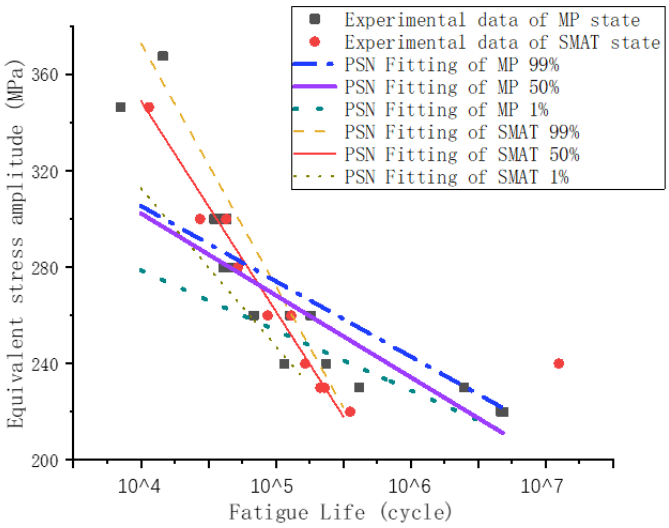

Figure 5. Ajustement P-S-N des états MP et SMAT.

Comme le montrent les courbes S-N, la durée de vie en fatigue de l'état SMAT ne présente pas de différence significative par rapport à l'état MP, pour toutes les amplitudes de contrainte appliquées. Ceci peut également être confirmé par la similitude de l'équation de Basquin et des courbes P-S-N.

3.3 Observation fractographique et mécanisme d'endommagement

L'observation fractographique des échantillons à l'état MP a révélé l'apparition de fissures de cisaillement et de traction à des niveaux de charge élevés et faibles, respectivement. En revanche, le comportement en traction des éprouvettes SMAT est presque indétectable. La zone plus petite du stade II, comme l'illustre la figure 6, indique que la croissance régulière des fissures est accélérée en raison de la qualité inférieure de la surface.

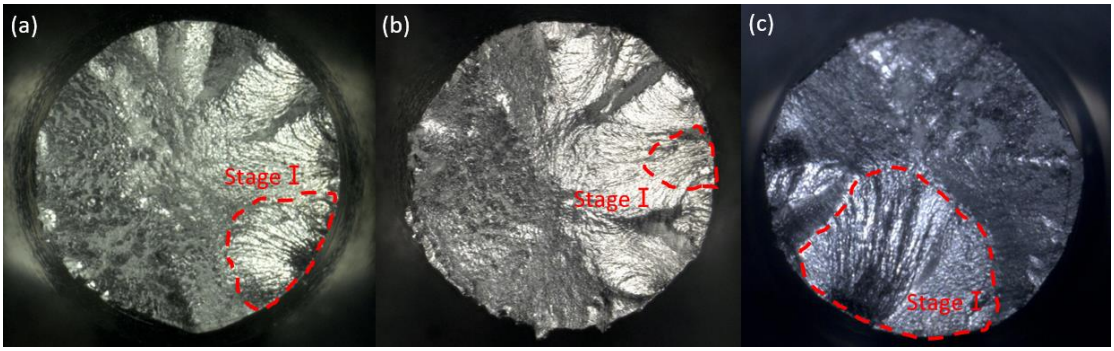

Figure 6. Figure 6. Observation des faciès de rupture: (a) état MP 368MPa ; (b) SMAT 280MPa; (c)MP 280MPa.

4. Rôle des facteurs induits par le SMAT dans l'influence de la résistance à la fatigue

Une analyse qualitative et quantitative a été menée pour déterminer les facteurs qui influencent l'impact du SMAT sur la résistance à la fatigue. Ces facteurs comprennent l'intégrité de la surface, les contraintes résiduelles induites par le SMAT et l'affinement du grain. Chaque facteur est étudié individuellement par le biais d'essais de fatigue, qui sont menés conjointement avec un traitement post-SMAT spécialement conçu à cet effet.

4.1 Intégrité de la surface

L'électropolissage est utilisé pour enlever une épaisseur spécifique de matériau de surface, améliorant ainsi de manière significative la qualité de la surface. La résistance à la fatigue des échantillons SMAT-EP s'est avérée nettement plus élevée que celle des échantillons MP et SMAT (figure 7). Cela indique que l'impact négatif du SMAT sur la résistance à la fatigue est principalement dû à l'augmentation de la rugosité et des défauts de la surface.

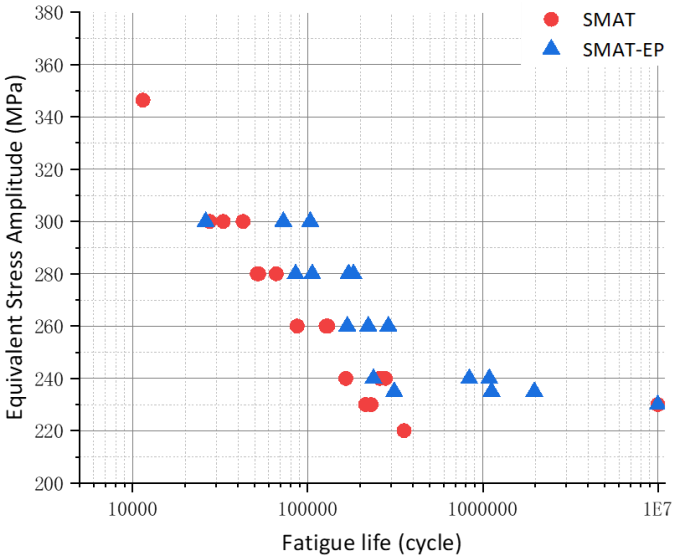

Figure 7. Comparaison des diagrammes S-N des échantillons SMAT et SMAT-EP.

4.2 Contrainte résiduelle

L'étude quantitative de la relaxation des contraintes résiduelles fait l'objet de la présente étude. Il est démontré que les contraintes résiduelles introduites par le SMAT sont relaxées au début des chargements cycliques, la relaxation ne durant pas plus de 35 % de la durée de vie totale (figure 8). Pour les échantillons testés à 300 MPa et 240 MPa, respectivement, 52 % et 72 % de la contrainte résiduelle initiale peuvent subsister après la relaxation.

Il a été démontré qu'un recuit post-SMAT de 9 heures à 185 °C est capable d'éliminer les contraintes résiduelles et l'écrouissage induits par le SMAT. La diminution de la résistance à la fatigue des échantillons SMAT-HT indique que les contraintes résiduelles et l'écrouissage augmentent considérablement la résistance à la fatigue de l'AA7075.

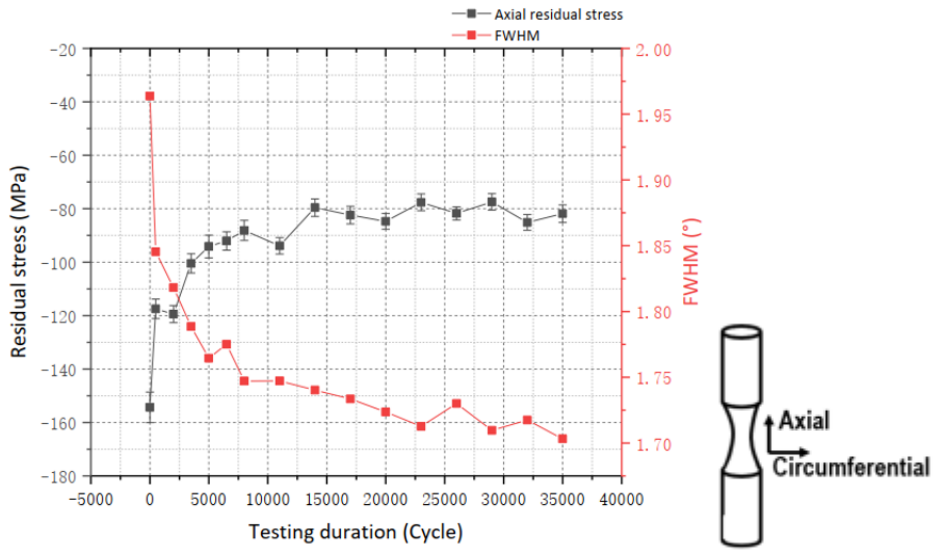

Figure 8. Évolution de la contrainte résiduelle et du FWHM lors d'un chargement cyclique (300MPa)

4.3 Raffinement des grains

La combinaison de l'électropolissage et du recuit post-SMAT a été utilisée pour vérifier l'impact de l'affinage des grains. L'amélioration de la durée de vie en fatigue des échantillons SMAT-EP-HT par rapport aux échantillons MP-HT suggère que l'affinage des grains contribue à l'amélioration de la résistance à la fatigue.

5. Estimation de la durée de vie en fatigue

5.1 Critères de fatigue

Le présent travail utilise les critères de Crossland, Findley et Fatemi-Socie pour prédire la résistance à la fatigue de l'AA7075 avec différents états de surface. Les paramètres matériels des critères de fatigue ont été déterminés par des essais de fatigue uniaxiale et de torsion menés au LASMIS, UTT.

5.2 5.2 Résultats de l'estimation de la durée de vie en fatigue et comparaison des critères

L'estimation est faite à 5×10^4, 10^5, $2{,}5\times10^5$, 5×10^5, $7{,}5\times10^5$ et 10^6 cycles. Les résultats indiquent que le critère de Crossland fournit la prédiction la plus précise pour l'état MP, tandis que les trois critères surestiment la résistance à la fatigue pour les états SMAT et SMAT-EP. La prédiction pour l'état SMAT présente l'écart le plus important par rapport aux deux autres états. L'écart dans la prédiction pour l'état SMAT peut être réduit de manière significative en incorporant un facteur de concentration de contrainte (K_t), qui peut prendre en compte l'effet de la rugosité de la surface.

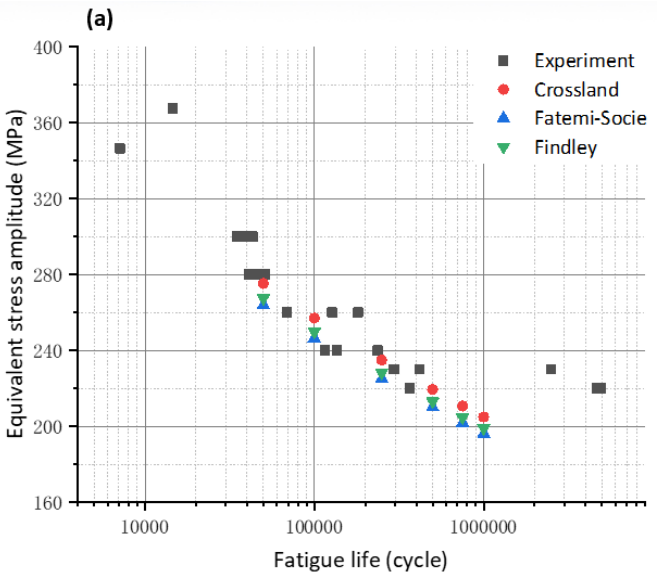

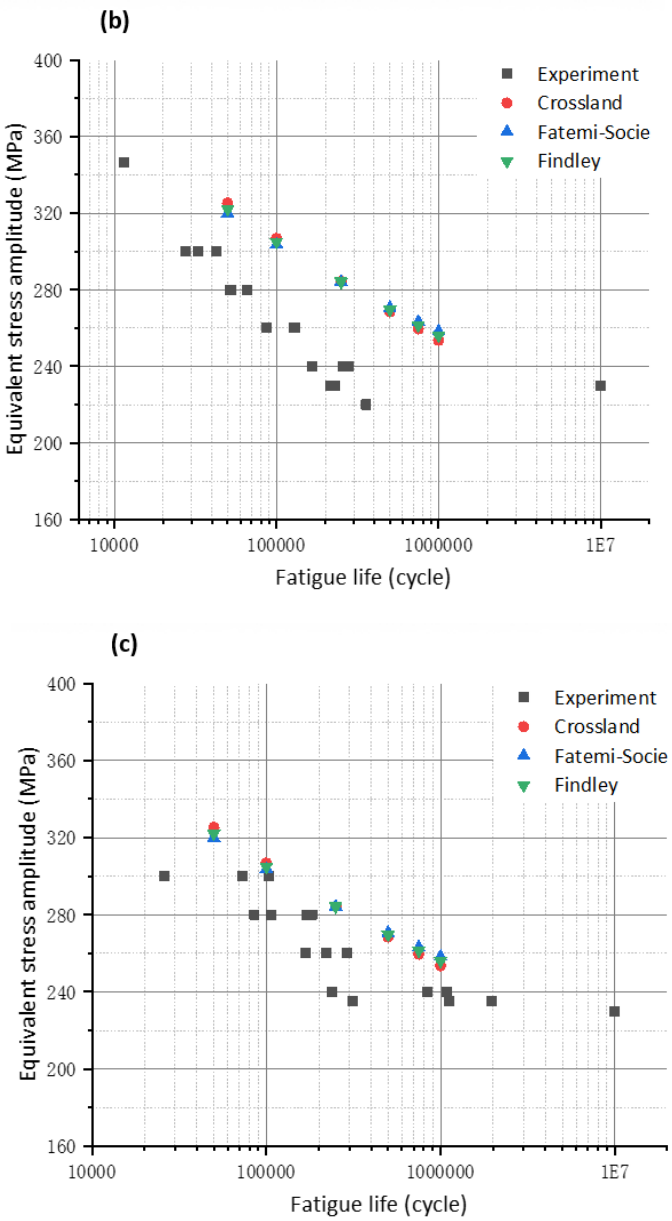

Figure 9. Courbes S-N des données expérimentales et prédites à partir (a) des essais MP, (b) des essais SMAT et (c) des essais SMAT-EP.

6. Conclusion et perspectives

Dans la présente étude, le matériau AA7075 est soumis à un traitement d'attrition mécanique de surface (SMAT), puis testé avec des charges biaxiales de tension-torsion proportionnelles. Une différence minime est observée entre les durées de vie en fatigue des spécimens polis mécaniquement (non-SMAT) et des spécimens soumis au SMAT. Les échantillons d'AA7075 polis mécaniquement présentaient des

comportements de fissuration par cisaillement et par traction à des niveaux élevés et faibles, respectivement, tandis que les échantillons SMAT présentaient principalement une fissuration par cisaillement. Un processus post-SMAT, comprenant l'électropolissage et le recuit, est utilisé pour étudier séparément les facteurs influençant la résistance à la fatigue. On peut conclure que la présence d'une couche de contrainte résiduelle compressive et l'affinement des grains ont un effet positif significatif sur la résistance à la fatigue du matériau, tandis que l'augmentation de la rugosité de la surface et les défauts ont un impact négatif. L'effet complexe du SMAT sur la résistance à la fatigue biaxiale de l'AA7075 est déterminé par l'existence de facteurs à la fois préjudiciables et bénéfiques, qui sont en concurrence les uns avec les autres.

Cette étude examine principalement l'effet du SMAT sur la résistance à la fatigue biaxiale en traction-torsion de l'AA7075. Étant donné le degré élevé de variabilité de la résistance à la fatigue multiaxiale en fonction des conditions de chargement, telles que l'angle de phase et les trajectoires de charge, les études futures devraient se concentrer sur la résistance à la fatigue multiaxiale des matériaux dotés de SMAT dans différentes conditions de chargement. En outre, il est important de noter que des matériaux de nature différente, tels que l'énergie de défaut d'empilement (SFE) et la sensibilité à l'entaille, peuvent présenter des comportements totalement différents après le SMAT. Il s'agit d'un domaine qui mérite d'être exploré plus en avant.

References

1. Li, Y. Experimental Study of Fatigue Properties under Different Loadings of an AA7075 Alloy Treated by SMAT. *http://www.theses.fr* **2021**.
2. Zhang, H.W.; Wang, L.; Hei, Z.K.; Liu, G.; Lu, J.; Lu, K. Low-Temperature Plasma Nitriding of AISI 304 Stainless Steel with Nano-Structured Surface Layer. *Zeitschrift fuer Met. Res. Adv. Tech.* **2003**, *94*, 1143–1147, doi:10.3139/146.031143.
3. Novelli, M.; Fundenberger, J.J.; Bocher, P.; Grosdidier, T. On the Effectiveness of Surface Severe Plastic Deformation by Shot Peening at Cryogenic Temperature. *Appl. Surf. Sci.* **2016**, *389*, 1169–1174, doi:10.1016/j.apsusc.2016.08.009.
4. Unal, O.; Varol, R. Surface Severe Plastic Deformation of AISI 304 via Conventional Shot Peening, Severe Shot Peening and Repeening. *Appl. Surf. Sci.* **2015**, *351*, 289–295, doi:10.1016/j.apsusc.2015.05.093.
5. Merwin, J.E.; Johnson, K.L. An Analysis of Plastic Deformation in Rolling Contact. *Proc. Inst. Mech. Eng.* **1963**, *177*, 676–690, doi:10.1243/pime_proc_1963_177_052_02.
6. Wong, C.C.; Hartawan, A.; Teo, W.K. Deep Cold Rolling of Features on Aero-Engine Components. *Procedia CIRP* **2014**, *13*, 350–354, doi:10.1016/j.procir.2014.04.059.
7. Roland, T.; Retraint, D.; Lu, K.; Lu, J. Fatigue Life Improvement through Surface Nanostructuring of Stainless Steel by Means of Surface Mechanical Attrition Treatment. *Scr. Mater.* **2006**, *54*, 1949–1954, doi:10.1016/j.scriptamat.2006.01.049.
8. Shaw, L.L.; Tian, J.W.; Ortiz, A.L.; Dai, K.; Villegas, J.C.; Liaw, P.K.; Ren, R.; Klarstrom, D.L. A Direct Comparison in the Fatigue Resistance Enhanced by Surface Severe Plastic Deformation and Shot Peening in a C-2000 Superalloy. *Mater. Sci. Eng. A* **2010**, *527*, 986–994, doi:10.1016/j.msea.2009.10.028.

9. Tian, J.W.; Villegas, J.C.; Yuan, W.; Fielden, D.; Shaw, L.; Liaw, P.K.; Klarstrom, D.L. A Study of the Effect of Nanostructured Surface Layers on the Fatigue Behaviors of a C-2000 Superalloy. *Mater. Sci. Eng. A* **2007**, *468–470*, 164–170, doi:10.1016/j.msea.2006.10.150.
10. Dai, K.; Shaw, L. Analysis of Fatigue Resistance Improvements via Surface Severe Plastic Deformation. *Int. J. Fatigue* **2008**, *30*, 1398–1408, doi:10.1016/j.ijfatigue.2007.10.010.
11. Umemoto, M.; Todaka, Y.; Tsuchiya, K. Formation of Nanocrystalline Structure in Steels by Air Blast Shot Peening. *Mater. Trans.* **2003**, *44*, 1488–1493, doi:10.2320/matertrans.44.1488.
12. Wang, T.; Yu, J.; Dong, B. Surface Nanocrystallization Induced by Shot Peening and Its Effect on Corrosion Resistance of 1Cr18Ni9Ti Stainless Steel. *Surf. Coatings Technol.* **2006**, *200*, 4777–4781, doi:10.1016/j.surfcoat.2005.04.046.
13. Tao, N.R.; Wang, Z.B.; Tong, W.P.; Sui, M.L.; Lu, J.; Lu, K. An Investigation of Surface Nanocrystallization Mechanism in Fe Induced by Surface Mechanical Attrition Treatment. *Acta Mater.* **2002**, *50*, 4603–4616, doi:10.1016/S1359-6454(02)00310-5.
14. Lu, K.; Lu, J. Nanostructured Surface Layer on Metallic Materials Induced by Surface Mechanical Attrition Treatment. *Mater. Sci. Eng. A* **2004**, *375–377*, 38–45, doi:10.1016/j.msea.2003.10.261.
15. Samih, Y.; Beausir, B.; Bolle, B.; Grosdidier, T. In-Depth Quantitative Analysis of the Microstructures Produced by Surface Mechanical Attrition Treatment (SMAT). *Mater. Charact.* **2013**, *83*, 129–138, doi:10.1016/j.matchar.2013.06.006.
16. Sun, Z.; Retraint, D.; Baudin, T.; Helbert, A.L.; Brisset, F.; Chemkhi, M.; Zhou, J.; Kanouté, P. Experimental Study of Microstructure Changes Due to Low Cycle Fatigue of a Steel Nanocrystallised by Surface Mechanical Attrition Treatment (SMAT). *Mater. Charact.* **2017**, *124*, 117–121, doi:10.1016/j.matchar.2016.12.017.
17. Zhou, J.; Sun, Z.; Kanouté, P.; Retraint, D. Effect of Surface Mechanical

Attrition Treatment on Low Cycle Fatigue Properties of an Austenitic Stainless Steel. *Int. J. Fatigue* **2017**, *103*, 309–317, doi:10.1016/j.ijfatigue.2017.06.011.

18. Lu, J.; Lu, K. 8.14 - Surface Nanocrystallization (SNC) of Materials and Its Effect on Mechanical Behavior. *Compr. Struct. Integr.* **2007**, *8*, 495–528, doi:10.1016/B0-08-043749-4/08037-X.
19. Wen, M.; Wen, C.; Peter, H.; Li, Y. Wear Behaviour of Pure Ti with a Nanocrystalline Surface Layer. *Appl. Mech. Mater.* **2011**, *66–68*, 1500–1504, doi:10.4028/www.scientific.net/AMM.66-68.1500.
20. Yang, X.F.; Lu, J. A New Way to Synthesize Carbon Nanofiber Film on Bulk Titanium via Hybrid Surface Mechanical Attrition Treatment. *Appl. Surf. Sci.* **2013**, *264*, 191–196, doi:10.1016/j.apsusc.2012.09.169.
21. Zhang, S.; Chen, H.; Lin, Q. Surface Nanocrystallization of Commercial Pure Titanium Induced by SMAT and Its Properties. *J. Mater. Sci. Technol.* **2004**, *20*, 716–718.
22. Sun, J.; Yao, Q.T.; Zhang, Y.H.; Du, X.D.; Wu, Y.C.; Tong, W.P. Simultaneously Improving Surface Mechanical Properties and in Vitro Biocompatibility of Pure Titanium via Surface Mechanical Attrition Treatment Combined with Low-Temperature Plasma Nitriding. *Surf. Coatings Technol.* **2017**, *309*, 382–389, doi:10.1016/j.surfcoat.2016.11.095.
23. Liu, Y.; Jin, B.; Lu, J. Mechanical Properties and Thermal Stability of Nanocrystallized Pure Aluminum Produced by Surface Mechanical Attrition Treatment. *Mater. Sci. Eng. A* **2015**, *636*, 446–451, doi:10.1016/j.msea.2015.03.068.
24. Darling, K.A.; Tschopp, M.A.; Roberts, A.J.; Ligda, J.P.; Kecskes, L.J. Enhancing Grain Refinement in Polycrystalline Materials Using Surface Mechanical Attrition Treatment at Cryogenic Temperatures. *Scr. Mater.* **2013**, *69*, 461–464, doi:10.1016/j.scriptamat.2013.05.036.
25. Han, Y.; Zhang, L.; Lu, J.; Zhang, W. Thermal Stability and Corrosion Resistance of Nanocrystallized Zirconium Formed by Surface Mechanical Attrition Treatment. *J. Mater. Res.* **2009**, *24*, 3136–3145, doi:10.1557/jmr.2009.0368.

26. Liu, X.; Nakatani, M.; Gao, H.; Sharma, B.; Pan, H.; Fu, Z.; Li, X.; Ameyama, K.; Zhu, X. Effect of Stacking Fault Energy on Deformation Mechanisms in Cu and Cu-30% Zn Alloy with Gradient Structure Obtained by SMAT. *J. Alloys Compd.* **2021**, *865*, 158863, doi:10.1016/j.jallcom.2021.158863.
27. Gallitelli, D.; Retraint, D.; Rouhaud, E. Comparison between Conventional Shot Peening (SP) and Surface Mechanical Attrition Treatment (SMAT) on a Titanium Alloy. *Adv. Mater. Res.* **2014**, *996*, 964–968, doi:10.4028/www.scientific.net/AMR.996.964.
28. Wu, X.; Tao, N.; Hong, Y.; Xu, B.; Lu, J.; Lu, K. Microstructure and Evolution of Mechanically-Induced Ultrafine Grain in Surface Layer of AL-Alloy Subjected to USSP. *Acta Mater.* **2002**, *50*, 2075–2084, doi:10.1016/S1359-6454(02)00051-4.
29. Pandey, V.; Chattopadhyay, K.; Santhi Srinivas, N.C.; Singh, V. Role of Ultrasonic Shot Peening on Low Cycle Fatigue Behavior of 7075 Aluminium Alloy. *Int. J. Fatigue* **2017**, *103*, 426–435, doi:10.1016/j.ijfatigue.2017.06.033.
30. An, X.; Rodopoulos, C.A.; Statnikov, E.S.; Vitazev, V.N.; Komlkov, O. V. Study of the Surface Nanocrystallization Induced by the Esonix Ultrasonic Impact Treatment on the Near-Surface of 2024-T351 Aluminum Alloy. *J. Mater. Eng. Perform.* **2006**, *15*, 355–364, doi:10.1361/105994906X108693.
31. Liao, M.; Chen, W.R.; Bellinger, N.C. Effects of Ultrasonic Impact Treatment on Fatigue Behavior of Naturally Exfoliated Aluminum Alloys. *Int. J. Fatigue* **2008**, *30*, 717–726, doi:10.1016/j.ijfatigue.2007.05.002.
32. Todaka, Y.; Umemoto, M.; Tsuchiya, K. Comparison of Nanocrystalline Surface Layer in Steels Formed by Air Blast and Ultrasonic Shot Peening. *Mater. Trans.* **2004**, *45*, 376–379, doi:10.2320/matertrans.45.376.
33. Pour-Ali, S.; Kiani-Rashid, A.R.; Babakhani, A. Surface Nanocrystallization and Gradient Microstructural Evolutions in the Surface Layers of 321 Stainless Steel Alloy Treated via Severe Shot Peening. *Vacuum* **2017**, *144*, 152–159, doi:10.1016/j.vacuum.2017.07.016.
34. Li, Y.R.; Lin, W.M.; Wei, Y.H.; Hou, L.F.; Du, H.Y. Characteristic and Properties of Nanocrystalline Surface Layer in Cu-10wt%Ni Alloy Induced by Surface

Mechanical Attrition Treatment. *Gongneng Cailiao/Journal Funct. Mater.* **2011**, *42*, 766–769.

35. Liu, Y.; Jin, B.; Li, D.J.; Zeng, X.Q.; Lu, J. Wear Behavior of Nanocrystalline Structured Magnesium Alloy Induced by Surface Mechanical Attrition Treatment. *Surf. Coatings Technol.* **2015**, *261*, 219–226, doi:10.1016/j.surfcoat.2014.11.026.
36. Shi, X.Y.; Liu, Y.; Li, D.J.; Chen, B.; Zeng, X.Q.; Lu, J.; Ding, W.J. Microstructure Evolution and Mechanical Properties of an Mg-Gd Alloy Subjected to Surface Mechanical Attrition Treatment. *Mater. Sci. Eng. A* **2015**, *630*, 146–154, doi:10.1016/j.msea.2015.02.009.
37. Joshi, M.D.; Kumar, V.; Litoria, A.K.; Singh, D.; Hosmani, S.S. Effect of Surface Mechanical Attrition Treatment on Tribological Behavior of AISI 2205 Steel. *Mater. Today Proc.* **2020**, *33*, 4919–4926, doi:10.1016/j.matpr.2020.02.487.
38. Huang, J.Y.; Zhu, Y.T.; Jiang, H.; Lowe, T.C. Microstructures and Dislocation Configurations in Nanostructured Cu Processed by Repetitive Corrugation and Straightening. *Acta Mater.* **2001**, *49*, 1497–1505, doi:10.1016/S1359-6454(01)00069-6.
39. Sun, H.Q.; Shi, Y.N.; Zhang, M.X.; Lu, K. Plastic Strain-Induced Grain Refinement in the Nanometer Scale in a Mg Alloy. *Acta Mater.* **2007**, *55*, 975–982, doi:10.1016/j.actamat.2006.09.018.
40. Bay, B.; Hansen, N.; Hughes, D.A.; Kuhlmann-Wilsdorf, D. Overview No. 96 Evolution of f.c.c. Deformation Structures in Polyslip. *Acta Metall. Mater.* **1992**, *40*, 205–219, doi:10.1016/0956-7151(92)90296-Q.
41. Christian, J.W.; Mahajan, S. Deformation Twinning. *Prog. Mater. Sci.* **1995**, *39*, 1–157, doi:10.1016/0079-6425(94)00007-7.
42. Zhu, Y.T.; Liao, X.Z.; Wu, X.L. Deformation Twinning in Nanocrystalline Materials. *Prog. Mater. Sci.* **2012**, *57*, 1–62, doi:10.1016/j.pmatsci.2011.05.001.
43. Li, Y.S.; Tao, N.R.; Lu, K. Microstructural Evolution and Nanostructure Formation in Copper during Dynamic Plastic Deformation at Cryogenic

Temperatures. *Acta Mater.* **2008**, *56*, 230–241, doi:10.1016/j.actamat.2007.09.020.

44. Meyers, M.A.; Vöhringer, O.; Lubarda, V.A. The Onset of Twinning in Metals: A Constitutive Description. *Acta Mater.* **2001**, *49*, 4025–4039, doi:10.1016/S1359-6454(01)00300-7.
45. Gatey, A.M.; Hosmani, S.S.; Figueroa, C.A.; Arya, S.B.; Singh, R.P. Role of Surface Mechanical Attrition Treatment and Chemical Etching on Plasma Nitriding Behavior of AISI 304L Steel. *Surf. Coatings Technol.* **2016**, *304*, 413–424, doi:10.1016/j.surfcoat.2016.07.020.
46. Yasuoka, M.; Wang, P.; Zhang, K.; Qiu, Z.; Kusaka, K.; Pyoun, Y.S.; Murakami, R. ichi Improvement of the Fatigue Strength of SUS304 Austenite Stainless Steel Using Ultrasonic Nanocrystal Surface Modification. *Surf. Coatings Technol.* **2013**, *218*, 93–98, doi:10.1016/j.surfcoat.2012.12.033.
47. Pandey, V.; Rao, G.S.; Chattopadhyay, K.; Santhi Srinivas, N.C.; Singh, V. Effect of Surface Nanostructuring on LCF Behavior of Aluminum Alloy 2014. *Mater. Sci. Eng. A* **2015**, *647*, 201–211, doi:10.1016/j.msea.2015.09.021.
48. Anand Kumar, S.; Ganesh Sundara Raman, S.; Sankara Narayanan, T.S.N.; Gnanamoorthy, R. Influence of Surface Mechanical Attrition Treatment on Fretting Wear Behaviour of Ti-6Al-4V. *Adv. Mater. Res.* **2012**, *463–464*, 316–320, doi:10.4028/www.scientific.net/AMR.463-464.316.
49. Ortiz, A.L.; Tian, J.W.; Shaw, L.L.; Liaw, P.K. Experimental Study of the Microstructure and Stress State of Shot Peened and Surface Mechanical Attrition Treated Nickel Alloys. *Scr. Mater.* **2010**, *62*, 129–132, doi:10.1016/j.scriptamat.2009.10.015.
50. Geng, D.; Sun, Q.; Xin, C.; Xiao, L. Contribution to Improvement of Fatigue Properties of Zr-4 Alloy: Gradient Nanostructured Surface Layer versus Compressive Residual Stress. *Nanomaterials* **2021**, *11*, 3125, doi:10.3390/nano11113125.
51. Ren, J.; Shan, A.; Zhang, J.; Song, H.; Liu, J. Surface Nanocrystallization of Ni3Al by Surface Mechanical Attrition Treatment. *Mater. Lett.* **2006**, *60*, 2076–2079,

doi:10.1016/J.MATLET.2005.12.076.

52. Maawad, E.; Brokmeier, H.G.; Wagner, L.; Sano, Y.; Genzel, C. Investigation on the Surface and Near-Surface Characteristics of Ti-2.5Cu after Various Mechanical Surface Treatments. *Surf. Coatings Technol.* **2011**, *205*, 3644–3650, doi:10.1016/j.surfcoat.2011.01.001.

53. Zhou, J.; Retraint, D.; Sun, Z.; Kanouté, P. Comparative Study of the Effects of Surface Mechanical Attrition Treatment and Conventional Shot Peening on Low Cycle Fatigue of a 316L Stainless Steel. *Surf. Coatings Technol.* **2018**, *349*, 556–566, doi:10.1016/j.surfcoat.2018.06.041.

54. Gao, T.; Sun, Z.; Xue, H.; Retraint, D. Effect of Surface Mechanical Attrition Treatment on High Cycle and Very High Cycle Fatigue of a 7075-T6 Aluminium Alloy. *Int. J. Fatigue* **2020**, *139*, doi:10.1016/j.ijfatigue.2020.105798.

55. Miková, K.; Bagherifard, S.; Bokuvka, O.; Guagliano, M.; Trško, L. Fatigue Behavior of X70 Microalloyed Steel after Severe Shot Peening. *Int. J. Fatigue* **2013**, *55*, 33–42, doi:10.1016/j.ijfatigue.2013.04.021.

56. Zhang, C.; Duan, X.; Zhou, L.; Lan, X. Surface Nanocrystallization of Zircaloy-4 by Surface Mechanical Attrition Treatment. *Mater. Sci. Forum* **2010**, *658*, 452–455, doi:10.4028/www.scientific.net/MSF.658.452.

57. Chen, X.H.; Lu, J.; Lu, L.; Lu, K. Tensile Properties of a Nanocrystalline 316L Austenitic Stainless Steel. *Scr. Mater.* **2005**, *52*, 1039–1044, doi:10.1016/j.scriptamat.2005.01.023.

58. Roland, T.; Retraint, D.; Lu, K.; Lu, J. Enhanced Mechanical Behavior of a Nanocrystallised Stainless Steel and Its Thermal Stability. *Mater. Sci. Eng. A* **2007**, *445–446*, 281–288, doi:10.1016/j.msea.2006.09.041.

59. Shi, X.Y.; Liu, Y.; Li, D.J.; Chen, B.; Zeng, X.Q.; Lu, J.; Ding, W.J. Microstructure Evolution and Mechanical Properties of an Mg-Gd Alloy Subjected to Surface Mechanical Attrition Treatment. *Mater. Sci. Eng. A* **2015**, *630*, 146–154, doi:10.1016/j.msea.2015.02.009.

60. Wu, Y.; Sun, Z.; Guelorget, B.; … R.S.-E. 2018 S.; 2018, undefined Characterization of the Gradient Properties of a 316L Steel Generated by

SMAT Using Micro-Pillar Compression Tests. *utt.hal.science*.

61. Yu, X.; Fu, T.; Zhan, Z.; Zhang, L.; Yang, Y.; Liu, Z.; Liu, J.; Li, L. Effect of Surface Mechanical Attrition Treatment on Corrosion Resistance of Commercial Pure Titanium. *ElsevierT Fu, Z Zhan, L Zhang, Y Yang, Z Liu, J Liu, L Li, X YuSurface Coatings Technol. 2015•Elsevier* **2015**, doi:10.1016/j.surfcoat.2015.08.041.
62. Jelliti, S.; Richard, C.; Retraint, D.; Roland, T.; Chemkhi, M.; Demangel, C. Effect of Surface Nanocrystallization on the Corrosion Behavior of Ti–6Al–4V Titanium Alloy. *Surf. Coatings Technol.* **2013**, *224*, 82–87, doi:10.1016/J.SURFCOAT.2013.02.052.
63. Li, N.; Shi, S.; Luo, J.; Lu, J.; Wang, N. Effects of Surface Nanocrystallization on the Corrosion Behaviors of 316L and Alloy 690. *Surf. Coatings Technol.* **2017**, *309*, 227–231, doi:10.1016/j.surfcoat.2016.11.052.
64. Benafia, S.; Retraint, D.; Yapi Brou, S.; Panicaud, B.; Grosseau Poussard, J.L. Influence of Surface Mechanical Attrition Treatment on the Oxidation Behaviour of 316L Stainless Steel. *Corros. Sci.* **2018**, *136*, 188–200, doi:10.1016/j.corsci.2018.03.007.
65. Gatey, A.M.; Hosmani, S.S.; Figueroa, C.A.; Arya, S.B.; Singh, R.P. Role of Surface Mechanical Attrition Treatment and Chemical Etching on Plasma Nitriding Behavior of AISI 304L Steel. *Surf. Coatings Technol.* **2016**, *304*, 413–424, doi:10.1016/j.surfcoat.2016.07.020.
66. Han, Y.; Zhang, L.; Lu, J.; Research, W.Z.-J. of M.; 2009, undefined Thermal Stability and Corrosion Resistance of Nanocrystallized Zirconium Formed by Surface Mechanical Attrition Treatment. *cambridge.orgY Han, L Zhang, J Lu, W ZhangJournal Mater. Res. 2009•cambridge.org* **2009**, doi:10.1557/JMR.2009.0368.
67. Pandey, V.; Singh, J.K.; Chattopadhyay, K.; Srinivas, N.C.S.; Singh, V. Influence of Ultrasonic Shot Peening on Corrosion Behavior of 7075 Aluminum Alloy. *J. Alloys Compd.* **2017**, *723*, 826–840, doi:10.1016/j.jallcom.2017.06.310.
68. Huang, H.W.; Wang, Z.B.; Yong, X.P.; Lu, K. Enhancing Torsion Fatigue Behaviour of a Martensitic Stainless Steel by Generating Gradient

Nanograined Layer via Surface Mechanical Grinding Treatment. *Mater. Sci. Technol. (United Kingdom)* **2013**, *29*, 1200–1205, doi:10.1179/1743284712Y.0000000192.

69. Wang, Z.B.; Tao, N.R.; Li, S.; Wang, W.; Liu, G.; Lu, J.; Lu, K. Effect of Surface Nanocrystallization on Friction and Wear Properties in Low Carbon Steel. *Mater. Sci. Eng. A* **2003**, *352*, 144–149, doi:10.1016/S0921-5093(02)00870-5.
70. Liu, Y.; Jin, B.; Li, D.J.; Zeng, X.Q.; Lu, J. Wear Behavior of Nanocrystalline Structured Magnesium Alloy Induced by Surface Mechanical Attrition Treatment. *Surf. Coatings Technol.* **2015**, *261*, 219–226, doi:10.1016/j.surfcoat.2014.11.026.
71. Zhang, Y.; Han, Z.; Wang, K.; Wear, K.L.-; 2006, undefined Friction and Wear Behaviors of Nanocrystalline Surface Layer of Pure Copper. *ElsevierYS Zhang, Z Han, K Wang, K LuWear, 2006•Elsevier* **2006**, *260*, 942–948, doi:10.1016/j.wear.2005.06.010.
72. Roland, T.; Retraint, D.; Lu, K.; Lu, J. Effect of Surface Nano Crystallization on Tribological Properties of Stainless Steel. *Mater. Sci. Forum* **2006**, *524–525*, 717–722, doi:10.4028/www.scientific.net/msf.524-525.717.
73. Rigney, D.A. Transfer, Mixing and Associated Chemical and Mechanical Processes during the Sliding of Ductile Materials. *Wear* **2000**, *245*, 1–9, doi:10.1016/S0043-1648(00)00460-9.
74. Joshi, M.D.; Kumar, V.; Litoria, A.K.; Singh, D.; Hosmani, S.S. Effect of Surface Mechanical Attrition Treatment on Tribological Behavior of AISI 2205 Steel. *Mater. Today Proc.* **2020**, *33*, 4919–4926, doi:10.1016/j.matpr.2020.02.487.
75. Liu, Z.; Zhang, H.; Yan, Z.; Liaw, P.K.; Dong, P. Cyclic Deformation and Fatigue Behavior of 7075-T651 Al Alloy with a Gradient Structure. *Mater. Sci. Eng. A* **2021**, *822*, doi:10.1016/j.msea.2021.141669.
76. Chen, Y.; Liu, F.; He, C.; Li, L.; Wang, C.; Liu, Y.; Wang, Q. Effect of Ultrasonic Peening Treatment on the Fatigue Behaviors of a Magnesium Alloy up to Very High Cycle Regime. *J. Magnes. Alloy.* **2022**, *10*, 614–626, doi:10.1016/j.jma.2021.07.028.

77. Kumar, S.; Chattopadhyay, K.; Singh, V. Effect of Ultrasonic Shot Peening on LCF Behavior of the Ti–6Al–4V Alloy. *J. Alloys Compd.* **2017**, *724*, 187–197, doi:10.1016/j.jallcom.2017.07.014.

78. Kumar, S.; Chattopadhyay, K.; Singh, V.; Satyanarayana, D.V.V.; Kumar, V. Low Cycle Fatigue Life of the Alloy IN718 Enhanced through Surface Nanostructuring. *Mater. Charact.* **2020**, *159*, doi:10.1016/j.matchar.2019.110066.

79. Chen, G.; Gao, J.; Cui, Y.; Gao, H.; Guo, X.; Wu, S. Effects of Strain Rate on the Low Cycle Fatigue Behavior of AZ31B Magnesium Alloy Processed by SMAT. *J. Alloys Compd.* **2018**, *735*, 536–546, doi:10.1016/j.jallcom.2017.11.141.

80. Yan, X.; Yin, S.; Chen, C.; Jenkins, R.; Lupoi, R.; Bolot, R.; Ma, W.; Kuang, M.; Liao, H.; Lu, J.; et al. Fatigue Strength Improvement of Selective Laser Melted Ti6al4v Using Ultrasonic Surface Mechanical Attrition. *Mater. Res. Lett.* **2019**, *7*, 327–333, doi:10.1080/21663831.2019.1609110.

81. Carneiro, L.; Wang, X.; Jiang, Y. Cyclic Deformation and Fatigue Behavior of 316L Stainless Steel Processed by Surface Mechanical Rolling Treatment. *Int. J. Fatigue* **2020**, *134*, doi:10.1016/j.ijfatigue.2019.105469.

82. Ramos, R.; Ferreira, N.; Ferreira, J.A.M.; Capela, C.; Batista, A.C. Improvement in Fatigue Life of Al 7475-T7351 Alloy Specimens by Applying Ultrasonic and Microshot Peening. *Int. J. Fatigue* **2016**, *92*, 87–95, doi:10.1016/j.ijfatigue.2016.06.022.

83. Uusitalo, J.; Karjalainen, L.P.; Retraint, D.; Palosaari, M. Fatigue Properties of Steels with Ultrasonic Attrition Treated Surface Layers. *Mater. Sci. Forum* **2009**, *604–605*, 239–248, doi:10.4028/3-908453-09-7.239.

84. Dureau, C.; Novelli, M.; Arzaghi, M.; Massion, R.; Bocher, P.; Nadot, Y.; Grosdidier, T. On the Influence of Ultrasonic Surface Mechanical Attrition Treatment (SMAT) on the Fatigue Behavior of the 304L Austenitic Stainless Steel. *Metals (Basel).* **2020**, *10*, doi:10.3390/met10010100.

85. Li, D.; Chen, H.N.; Xu, H. The Effect of Nanostructured Surface Layer on the Fatigue Behaviors of a Carbon Steel. *Appl. Surf. Sci.* **2009**, *255*, 3811–3816,

doi:10.1016/j.apsusc.2008.10.037.

86. Zhang, C.; Song, G.; Wang, Y.; Zheng, M.; Xiao, G.; Yang, J. Effect of Surface Nanocrystallization on Fatigue Crack Initiation and Propagation Behavior in Pure Zr. *Mater. Sci. Eng. A* **2020**, *794*, doi:10.1016/j.msea.2020.139831.
87. Li, D.; Chen, H.N.; Xu, H. Comparative Responses of Welded Joints to Surface Mechanical Attrition Treatment and Shot Peening. *Surf. Eng.* **2009**, *25*, 15–20, doi:10.1179/174329409X389335.
88. Yin, D.; Wang, D.; Jing, H.; Huo, L. The Effects of Ultrasonic Peening Treatment on the Ultra-Long Life Fatigue Behavior of Welded Joints. *Mater. Des.* **2010**, *31*, 3299–3307, doi:10.1016/j.matdes.2010.02.006.
89. Wang, Y.; Huang, M.; Zhou, L.; Cong, Z.; Gao, H. Improved Fatigue Behavior of Pipeline Steel Welded Joint by Surface Mechanical Attrition Treatment (SMAT). *J. Mater. Sci. Technol.* **2009**, *25*, 513–515.
90. Zhao, X.; Wang, D.; Huo, L. Analysis of the S-N Curves of Welded Joints Enhanced by Ultrasonic Peening Treatment. *Mater. Des.* **2011**, *32*, 88–96, doi:10.1016/j.matdes.2010.06.030.
91. Lago, J.; Trško, L.; Jambor, M.; Nový, F.; Bokůvka, O.; Mičian, M.; Pastorek, F. Fatigue Life Improvement of the High Strength Steel Welded Joints by Ultrasonic Impact Peening. *Metals (Basel).* **2019**, *9*, doi:10.3390/met9060619.
92. An, L.; Sun, Y.T.; Lu, S.P.; Wang, Z.B. Enhanced Fatigue Property of Welded S355J2W Steel by Forming a Gradient Nanostructured Surface Layer. *Acta Metall. Sin. (English Lett.* **2020**, *33*, 1252–1258, doi:10.1007/s40195-020-01046-8.
93. Wu, B.; Zhang, J.; Zhang, L.; Pyoun, Y.S.; Murakami, R.I. Effect of Ultrasonic Nanocrystal Surface Modification on Surface and Fatigue Properties of Quenching and Tempering S45C Steel. *Appl. Surf. Sci.* **2014**, *321*, 318–330, doi:10.1016/j.apsusc.2014.09.068.
94. Kakiuchi, T.; Uematsu, Y.; Hasegawa, N.; Kondoh, E. Effect of Ultrasonic Shot Peening on High Cycle Fatigue Behavior in Type 304 Stainless Steel at Elevated Temperature. *Zair. Soc. Mater. Sci. Japan* **2016**, *65*, 325–330,

doi:10.2472/jsms.65.325.

95. Amanov, A.; Pyun, Y.S.; Kim, J.H.; Suh, C.M.; Cho, I.S.; Kim, H.D.; Wang, Q.; Khan, M.K. Ultrasonic Fatigue Performance of High Temperature Structural Material Inconel 718 Alloys at High Temperature after UNSM Treatment. *Fatigue Fract. Eng. Mater. Struct.* **2015**, *38*, 1266–1273, doi:10.1111/ffe.12330.
96. Benedetti, M.; Fontanari, V.; Bandini, M.; Taylor, D. Multiaxial Fatigue Resistance of Shot Peened High-Strength Aluminum Alloys. *Int. J. Fatigue* **2014**, *61*, 271–282, doi:10.1016/j.ijfatigue.2013.10.020.
97. Benedetti, M.; Fontanari, V.; Allahkarami, M.; Hanan, J.C.; Bandini, M. On the Combination of the Critical Distance Theory with a Multiaxial Fatigue Criterion for Predicting the Fatigue Strength of Notched and Plain Shot-Peened Parts. *Int. J. Fatigue* **2016**, *93*, 133–147, doi:10.1016/j.ijfatigue.2016.08.015.
98. Wang, Q.; Xin, C.; Sun, Q.; Xiao, L.; Sun, J. Biaxial Tension-Torsion Fatigue Behavior of Gradient Nano-Grained Pure Titanium Fabricated by Surface Nanocrystallization. *Mater. Sci. Eng. A* **2017**, *702*, 125–132, doi:10.1016/j.msea.2017.05.031.
99. Suh, M.S.; Suh, C.M.; Pyun, Y.S. Very High Cycle Fatigue Characteristics of a Chrome-Molybdenum Steel Treated by Ultrasonic Nanocrystal Surface Modification Technique. *Fatigue Fract. Eng. Mater. Struct.* **2013**, *36*, 769–778, doi:10.1111/ffe.12045.
100. Khan, M.K.; Liu, Y.J.; Wang, Q.Y.; Pyun, Y.S.; Kayumov, R. Effect of Ultrasonic Nanocrystal Surface Modification on the Characteristics of AISI 310 Stainless Steel up to Very High Cycle Fatigue. *Fatigue Fract. Eng. Mater. Struct.* **2016**, *39*, 427–438, doi:10.1111/ffe.12367.
101. Shamsaei, N.; Fatemi, A. Effect of Microstructure and Hardness on Non-Proportional Cyclic Hardening Coefficient and Predictions. *Mater. Sci. Eng. A* **2010**, *527*, 3015–3024, doi:10.1016/j.msea.2010.01.056.
102. Hanlon, T.; Tabachnikova, E.D.; Suresh, S. Fatigue Behavior of Nanocrystalline Metals and Alloys. *Int. J. Fatigue* **2005**, *27*, 1147–1158,

doi:10.1016/j.ijfatigue.2005.06.035.

103. Hanlon, T.; Kwon, Y.N.; Suresh, S. Grain Size Effects on the Fatigue Response of Nanocrystalline Metals. *Scr. Mater.* **2003**, *49*, 675–680, doi:10.1016/S1359-6462(03)00393-2.

104. Wu, B.; Wang, P.; Pyoun, Y.S.; Zhang, J.; Murakami, R. ichi Effect of Ultrasonic Nanocrystal Surface Modification on the Fatigue Behaviors of Plasma-Nitrided S45C Steel. *Surf. Coatings Technol.* **2012**, *213*, 271–277, doi:10.1016/j.surfcoat.2012.10.063.

105. Ochi, Y.; Masaki, K.; Matsumura, T.; Sekino, T. Effect of Shot-Peening Treatment on High Cycle Fatigue Property of Ductile Cast Iron. *Int. J. Fatigue* **2001**, *23*, 441–448, doi:10.1016/S0142-1123(00)00110-9.

106. Arakawa, J.; Kakuta, M.; Hayashi, Y.; Tanegashima, R.; Akebono, H.; Kato, M.; Sugeta, A. Fatigue Strength of USP Treated ASTM CA6NM for Hydraulic Turbine Runner. *Surf. Eng.* **2014**, *30*, 662–669, doi:10.1179/1743294414Y.0000000308.

107. Shimatani, Y.; Shiozawa, K.; Nakada, T.; Yoshimoto, T.; Lu, L. The Effect of the Residual Stresses Generated by Surface Finishing Methods on the Very High Cycle Fatigue Behavior of Matrix HSS. *Int. J. Fatigue* **2011**, *33*, 122–131, doi:10.1016/j.ijfatigue.2010.07.009.

108. Dalaei, K.; Karlsson, B.; Svensson, L.E. Stability of Shot Peening Induced Residual Stresses and Their Influence on Fatigue Lifetime. *Mater. Sci. Eng. A* **2011**, *528*, 1008–1015, doi:10.1016/j.msea.2010.09.050.

109. Zhou, J.; Sun, Z.; Kanouté, P.; Retraint, D. Reconstruction of Residual Stress and Work Hardening and Their Effects on the Mechanical Behaviour of a Shot Peened Structure. *Mech. Mater.* **2018**, *127*, 100–111, doi:10.1016/j.mechmat.2018.09.005.

110. Kumar, S.A.; Raman, S.G.S.; Narayanan, T.S.N.S. Influence of Surface Mechanical Attrition Treatment Duration on Fatigue Lives of Ti-6Al-4V. *Trans. Indian Inst. Met.* **2014**, *67*, 137–141, doi:10.1007/s12666-013-0322-2.

111. Huang, G.R.; Tsai, W.Y.; Huang, J.C.; Hu, C.K. Analytical Modelling for

Ultrasonic Surface Mechanical Attrition Treatment. *AIP Adv.* **2015**, *5*, doi:10.1063/1.4926811.

112. Maurel, P.; Weiss, L.; Grosdidier, T.; Bocher, P. How Does Surface Integrity of Nanostructured Surfaces Induced by Severe Plastic Deformation Influence Fatigue Behaviors of Al Alloys with Enhanced Precipitation? *Int. J. Fatigue* **2020**, *140*, doi:10.1016/j.ijfatigue.2020.105792.
113. Amanov, A.; Karimbaev, R.; Maleki, E.; Unal, O.; Pyun, Y.S.; Amanov, T. Effect of Combined Shot Peening and Ultrasonic Nanocrystal Surface Modification Processes on the Fatigue Performance of AISI 304. *Surf. Coatings Technol.* **2019**, *358*, 695–705, doi:10.1016/j.surfcoat.2018.11.100.
114. Novelli, M.; Bocher, P.; Grosdidier, T. Effect of Cryogenic Temperatures and Processing Parameters on Gradient-Structure of a Stainless Steel Treated by Ultrasonic Surface Mechanical Attrition Treatment. *Mater. Charact.* **2018**, *139*, 197–207, doi:10.1016/j.matchar.2018.02.028.
115. Maurel, P.; Weiss, L.; Bocher, P.; Grosdidier, T. Effects of SMAT at Cryogenic and Room Temperatures on the Kink Band and Martensite Formations with Associated Fatigue Resistance in a β-Metastable Titanium Alloy. *Mater. Sci. Eng. A* **2021**, *803*, doi:10.1016/j.msea.2020.140618.
116. Bagherifard, S.; Guagliano, M. Fatigue Behavior of a Low-Alloy Steel with Nanostructured Surface Obtained by Severe Shot Peening. *Eng. Fract. Mech.* **2012**, *81*, 56–68, doi:10.1016/j.engfracmech.2011.06.011.
117. Stinville, J.C.; Cormier, J.; Templier, C.; Villechaise, P. Monotonic Mechanical Properties of Plasma Nitrided 316L Polycrystalline Austenitic Stainless Steel: Mechanical Behaviour of the Nitrided Layer and Impact of Nitriding Residual Stresses. *Mater. Sci. Eng. A* **2014**, *605*, 51–58, doi:10.1016/j.msea.2014.03.039.
118. Lequeu, P.; Smith, K.P.; Daniélou, A. Aluminum-Copper-Lithium Alloy 2050 Developed for Medium to Thick Plate. *J. Mater. Eng. Perform.* **2010**, *19*, 841–847, doi:10.1007/S11665-009-9554-Z.
119. Andreatta, F. Local Electrochemical Behaviour of 7xxx Aluminium Alloys. **2004**.

120. Dixit, M.; Mishra, R.S.; Sankaran, K.K. Structure-Property Correlations in Al 7050 and Al 7055 High-Strength Aluminum Alloys. *Mater. Sci. Eng. A* **2008**, *478*, 163–172, doi:10.1016/j.msea.2007.05.116.

121. Panigrahi, S.; A, R.J.-M. and M.T.; 2011, undefined Effect of Annealing on Thermal Stability, Precipitate Evolution, and Mechanical Properties of Cryorolled Al 7075 Alloy. *SpringerSK Panigrahi, R JayaganthanMetallurgical Mater. Trans. A, 2011•Springer* **2011**, *42*, 3208–3217, doi:10.1007/s11661-011-0723-y.

122. LI, J. feng; PENG, Z. wei; LI, C. xing; JIA, Z. qiang; CHEN, W. jing; ZHENG, Z. qiao Mechanical Properties, Corrosion Behaviors and Microstructures of 7075 Aluminium Alloy with Various Aging Treatments. *Trans. Nonferrous Met. Soc. China (English Ed.* **2008**, *18*, 755–762, doi:10.1016/S1003-6326(08)60130-2.

123. Birbilis, N.; Cavanaugh, M.K.; Buchheit, R.G. Electrochemical Behavior and Localized Corrosion Associated with Al7Cu2Fe Particles in Aluminum Alloy 7075-T651. *Corros. Sci.* **2006**, *48*, 4202–4215, doi:10.1016/j.corsci.2006.02.007.

124. Mahathaninwong, N.; Plookphol, T.; Wannasin, J.; Wisutmethangoon, S. T6 Heat Treatment of Rheocasting 7075 Al Alloy. *Mater. Sci. Eng. A* **2012**, *532*, 91–99, doi:10.1016/j.msea.2011.10.068.

125. Tehinse, O.B. Response of 7075 and 7050 Aluminium Alloys to High Temperature Pre-Precipitation Heat Treatment. **2014**, 12–21.

126. Fu, L.; Duan, H.; Li, H.; Lin, L.; Wang, Q.; Yao, J.; Luo, Y. Low-Cycle Fatigue Behavior of 7075-T6 Aluminum Alloy at Different Strain Amplitudes. *Mater. Express* **2020**, *10*, 942–947, doi:10.1166/MEX.2020.1696.

127. Zhao, T.; Jiang, Y. Fatigue of 7075-T651 Aluminum Alloy. *Int. J. Fatigue* **2008**, *30*, 834–849, doi:10.1016/j.ijfatigue.2007.07.005.

128. Tanaka, K.; Matsuoka, S.; Kimura, M. FATIGUE STRENGTH OF 7075-T6 ALUMINIUM ALLOY UNDER COMBINED AXIAL LOADING AND TORSION. *Fatigue Fract. Eng. Mater. Struct.* **1984**, *7*, 195–211, doi:10.1111/J.1460-2695.1984.TB00189.X.

129. Singh, A.K.; Datta, S.; Chattopadhyay, A.; Riddick, J.C.; Hall, A.J. Fatigue Crack Initiation and Propagation Behavior in Al – 7075 Alloy under in-Phase Bending-Torsion Loading. *Int. J. Fatigue* **2019**, *126*, 346–356, doi:10.1016/j.ijfatigue.2019.05.024.

130. Li, Y.; Retraint, D.; Gao, P.; Xue, H.; Gao, T.; Sun, Z. Effect of Surface Mechanical Attrition Treatment on Torsional Fatigue Properties of a 7075 Aluminum Alloy. *Metals (Basel).* **2022**, doi:10.3390/met12050785.

131. Fatemi, A.; Shamsaei, N. Multiaxial Fatigue: An Overview and Some Approximation Models for Life Estimation. *Int. J. Fatigue* **2011**, *33*, 948–958, doi:10.1016/j.ijfatigue.2011.01.003.

132. TAIRA, S.; INOUE, T.; YOSHIDA, T. Low Cycle Fatigue under Multiaxial Stresses : In the Case of Combined Cyclic Tension-Compression and Cyclic Torsion at Room Temperature. *Trans. Japan Soc. Mech. Eng.* **1969**, *35*, 526–532, doi:10.1299/kikai1938.35.526.

133. Lamba, H.S.; Sidebottom, O.M. Cyclic Plasticity for Nonproportional Paths: Part 1 - Cyclic Hardening, Erasure of Memory, and Subsequent Strain Hardening Experiments. *Am. Soc. Mech. Eng.* **1977**.

134. Kanazawa, K.; … K.M.-F.& F. of; 1979, undefined Cyclic Deformation of 1% Cr-Mo-V Steel under Out-of-phase Loads. *Wiley Online Libr. Kanazawa, KJ Miller, MW BrownFatigue Fract. Eng. Mater. Struct. 1979•Wiley Online Libr.* **1979**, *2*, 211–228, doi:10.1111/j.1460-2695.1979.tb01357.x.

135. Sonsino, C.M.; Grubisic, V. Fatigue Behavior of Cyclically Softening and Hardening Steels Under Multiaxial Elastic-Plastic Deformation. *ASTM Spec. Tech. Publ.* **1985**, 586–605, doi:10.1520/stp36244s.

136. Shamsaei, N.; Gladskyi, M.; Panasovskyi, K.; Shukaev, S.; Fatemi, A. Multiaxial Fatigue of Titanium Including Step Loading and Load Path Alteration and Sequence Effects. *Int. J. Fatigue* **2010**, *32*, 1862–1874, doi:10.1016/j.ijfatigue.2010.05.006.

137. Bannantine, J.A.; Socie, D.F. Observations of Cracking Behavior in Tension and Torsion Low Cycle Fatigue. *ASTM Spec. Tech. Publ.* **1987**, 899–921,

doi:10.1520/stp24530s.

138. Hua, C.T.; Socie, D.F. FATIGUE DAMAGE IN 1045 STEEL UNDER VARIABLE AMPLITUDE BIAXIAL LOADING. *Fatigue Fract. Eng. Mater. Struct.* **1985**, *8*, 101–114, doi:10.1111/J.1460-2695.1985.TB01197.X.

139. Brown, M.; … K.M.-& F. of E.M.&; 1979, undefined High Temperature Low Cycle Biaxial Fatigue of Two Steels. *Wiley Online Libr. Brown, KJ MillerFatigue Fract. Eng. Mater. Struct. 1979•Wiley Online Libr.* **1979**, *1*, 217–229, doi:10.1111/j.1460-2695.1979.tb00379.x.

140. Brown, M.; … K.M.-& F. of E.M.&; 1979, undefined Initiation and Growth of Cracks in Biaxial Fatigue. *Wiley Online Libr. Brown, KJ MillerFatigue Fract. Eng. Mater. Struct. 1979•Wiley Online Libr.* **1979**, *1*, 231–246, doi:10.1111/j.1460-2695.1979.tb00380.x.

141. Shamsaei, N.; Fatemi, A. Effect of Hardness on Multiaxial Fatigue Behaviour and Some Simple Approximations for Steels. *Fatigue Fract. Eng. Mater. Struct.* **2009**, *32*, 631–646, doi:10.1111/J.1460-2695.2009.01369.X.

142. Qu, W.L.; Zhao, E.N.; Zhou, Q.; Pi, Y.L. Multiaxial Low-Cycle Fatigue Life Evaluation under Different Non-Proportional Loading Paths. *Fatigue Fract. Eng. Mater. Struct.* **2018**, *41*, 1064–1076, doi:10.1111/FFE.12752.

143. Zhao, B.F.; Xie, L.Y.; Bai, X.; Ren, J.G.; Li, H.Y.; Zhang, S.J. A Multi-Axial Low-Cycle Fatigue Life Prediction Model Considering Effects of Additional Hardening. *Fatigue Fract. Eng. Mater. Struct.* **2018**, *41*, 1488–1503, doi:10.1111/FFE.12791.

144. Shamsaei, N.; Fatemi, A.; Socie, D.F. Multiaxial Fatigue Evaluation Using Discriminating Strain Paths. *Int. J. Fatigue* **2011**, *33*, 597–609, doi:10.1016/j.ijfatigue.2010.11.002.

145. Mei, J.; Dong, P. Modeling of Path-Dependent Multi-Axial Fatigue Damage in Aluminum Alloys. *Int. J. Fatigue* **2017**, *95*, 252–263, doi:10.1016/j.ijfatigue.2016.10.031.

146. Findley, W.N.; Mathur, P.N. Modified Theories of Fatigue Failure under Combined Stress. *Proc. Soc. Exp. Stress Anal.* **1955**, *14*, 35–46.

147. Fatemi, A.; Socie, D.F. A Critical Plane Approach To Multiaxial Fatigue Damage Including Out-of-Phase Loading. *Fatigue Fract. Eng. Mater. Struct.* **1988**, *11*, 149–165, doi:10.1111/j.1460-2695.1988.tb01169.x.

148. Smith, R.; Watson, P.; Topper, T. A Stress–Strain Function for the Fatigue of Metal. *J Mater* **1970**, *5*, 767–778.

149. Jiang, Y. Fatigue Criterion for General Multiaxial Loading. *Fatigue Fract. Eng. Mater. Struct.* **2000**, *23*, 19–32, doi:10.1046/j.1460-2695.2000.00247.x.

150. Tschegg, E.K. Mode III and Mode I Fatigue Crack Propagation Behaviour under Torsional Loading. *J. Mater. Sci.* **1983**, *18*, 1604–1614, doi:10.1007/BF00542053.

151. Kongiang, S.; Plookphol, T.; Wannasin, J.; Wisutmethangoon, S. Effect of the Two-Step Solution Heat Treatment on the Microstructure of Semisolid Cast 7075 Aluminum Alloy. *Trans Tech PublS Kongiang, T Plookphol, J Wannasin, S WisutmethangoonAdvanced Mater. Res. 2012•Trans Tech Publ* **2012**, doi:10.4028/www.scientific.net/AMR.488-489.243.

152. Leng, L.; Zhang, Z.J.; Duan, Q.Q.; Zhang, P.; Zhang, Z.F. Improving the Fatigue Strength of 7075 Alloy through Aging. *Mater. Sci. Eng. A* **2018**, *738*, 24–30, doi:10.1016/j.msea.2018.09.047.

153. Tao, N.R.; Sui, M.L.; Lu, J.; Lua, K. Surface Nanocrystallization of Iron Induced by Ultrasonic Shot Peening. *Nanostructured Mater.* **1999**, *11*, 433–440, doi:10.1016/S0965-9773(99)00324-4.

154. Lu, J.; Lu, K. Surface Nanocrystallization (SNC) of Materials and Its Effect on Mechanical Behavior. *Compr. Struct. Integr.* **2003**, *8*, 495–528, doi:10.1016/B0-08-043749-4/08037-X.

155. Padilla, H.A.; Boyce, B.L. A Review of Fatigue Behavior in Nanocrystalline Metals. *Exp. Mech.* **2010**, *50*, 5–23, doi:10.1007/s11340-009-9301-2.

156. Sines, G.; Ohgi, G. Fatigue Criteria Under Combined Stresses or Strains. *J. Eng. Mater. Technol.* **1981**, *103*, 82–90, doi:10.1115/1.3224995.

157. Effect of Large Hydrostatic Pressures on the Torsional... - Available online: https://scholar.google.com/scholar?hl=zh-

CN&as_sdt=0%2C5&q=Effect+of+large+hydrostatic+pressures+on+the+torsional+fatigue+strength+of+an+alloy+steel&btnG= (accessed on 9 February 2024).

158. Briffod, F.; Shiraiwa, T.; Enoki, M. Sur La Résistance à La Fatigue Des Métaux. *Sci. Tech. l'armement* **1973**, *47*, 641-, doi:10.1016/J.IJFATIGUE.2017.10.019.

159. Findley, W.N. A Theory for the Effect of Mean Stress on Fatigue of Metals Under Combined Torsion and Axial Load or Bending. *J. Eng. Ind.* **1959**, *81*, 301–305, doi:10.1115/1.4008327.

160. Li, J.K.; Mei, Y.; Duo, W.; Renzhi, W. AN ANALYSIS OF STRESS CONCENTRATIONS CAUSED BY SHOT PEENING AND ITS APPLICATION IN PREDICTING FATIGUE STRENGTH. *Fatigue Fract. Eng. Mater. Struct.* **1992**, *15*, 1271–1279, doi:10.1111/J.1460-2695.1992.TB01262.X.

Pengfei GAO

Doctorat : Matériaux, Mécanique, Optique et Nanotechnologie

Année 2024

Propriétés de fatigue sous chargements complexes d'un alliage AA7075 traité par SMAT

Le traitement par attrition mécanique de surface (SMAT) est capable d'améliorer les propriétés mécaniques des matériaux métalliques. L'effet du SMAT sur les propriétés de fatigue biaxiale d'un alliage d'aluminium 7075 a été étudié dans ce travail. Des éprouvettes sous forme d'haltères en alliage AA7075 ont été traitées par SMAT, après usinage, traitement thermique non standard et polissage mécanique. Les profils de contrainte résiduelle induits par SMAT ont été déterminés par diffraction des rayons X. Des essais de fatigue biaxiale ont été menés sous des chargements de traction-torsion proportionnels combinés. Une différence minimale de résistance à la fatigue a été constatée entre les échantillons polis mécaniquement et les échantillons traités par SMAT à des niveaux de chargement élevés et intermédiaires, tandis qu'une réduction a été constatée après SMAT pour de faibles niveaux de chargement. Les effets des facteurs induits par le SMAT ont été étudiés individuellement par un processus post-SMAT spécialement conçu, tel qu'un recuit et un électropolissage. La couche de contraintes résiduelles de compression et la détérioration de l'intégrité de la surface ont été considérées comme les principaux facteurs bénéfiques et néfastes respectivement. Les échantillons traités par SMAT puis électropolis ont présenté une résistance à la fatigue significativement plus élevée pour tous les niveaux de chargement. Des critères de fatigue multiaxiale ont été appliqués pour estimer la résistance à la fatigue des échantillons polis mécaniquement et traités par SMAT.

Mots clés : aluminium, alliages – grenaillage de précontrainte – contraintes résiduelles – matériaux, fatigue – matériaux, fissuration.

Fatigue Properties Under Complex Loadings of an AA7075 Alloy Processed by SMAT

Surface Mechanical Attrition Treatment (SMAT) is able of improving mechanical properties of metallic materials. The effect of SMAT on the biaxial fatigue properties of a 7075 aluminum alloy was investigated in the present work. The AA7075 dumbbell specimens were treated by SMAT, after a non-standard heat treatment and mechanical polishing. The SMAT-induced residual stress and its profile were evaluated by X-ray diffraction. Biaxial fatigue tests were performed under proportional combined tension-torsion loadings. A minimal difference in fatigue strength was found between mechanically-polished specimens and SMATed specimens at high and medium load levels, while a reduction was found after SMAT at low load levels. The effects of factors induced by SMAT were individually investigated by specially-designed post-SMAT processes, such as annealing and electropolishing. The compressive residual stress layer and the deterioration of surface integrity were considered as the main beneficial and detrimental factors respectively. Specimens treated by SMAT and electropolishing exhibited significantly higher fatigue strength at all load levels. Multiaxial fatigue criteria were applied to estimate the fatigue strength of both mechanically-polished and SMATed specimens.

Keywords: aluminum alloys – shot peening – residual stresses – materials, fatigue – materials, cracking.

Thèse réalisée en partenariat entre :

Ecole Doctorale "Sciences pour l'Ingénieur"